Design and Analysis of a Superconducting Magnet Cryostat for Traveling Heater Method Growth of CdZnTe

by

Robbi Lynn McDonald
B.Sc., University of Victoria, 2000

A Thesis Submitted in Partial Fulfillment of the
Requirements for the Degree of

Master of Applied Science

in the Department of Mechanical Engineering

We accept this thesis as conforming
to the required standard

[redacted]

Dr. Sadik Dost, Supervisor (Department of Mechanical Engineering)

[redacted]

Dr. Andrew Rowe, Co-Supervisor (Department of Mechanical Engineering)

[redacted]

Dr. George Beer, Outside Member (Department of Physics)

[redacted]

Dr. Pan Agathoklis, External Examiner (Department of Electrical and Computer Engineering)

Supervisor: Dr. Sadik Dost

Abstract

Cadmium Zinc Telluride (CdZnTe) has been identified as an excellent gamma ray detector material. However, finding an economical way to grow large high quality crystals has been difficult. Using traveling heater method (THM) with a rotating and static magnetic field may be the solution. The rotating magnetic field could increase the growth rate and a static magnetic field less than 1.25 Tesla may reduce growth defects. The design and analysis of a 1.25 Tesla superconducting magnet cryostat system that surrounds the THM furnace with a rotating magnetic field is the focus of this thesis. Individual system components examined include the vacuum vessel, structural supports, current leads, and insulation. Total heat transfer from all of these components is determined and the operating temperature of the superconducting magnet is estimated. Finally, the instrumentation required to monitor the superconducting magnet state is discussed and the uncertainties in the measurement are approximated.

Examiners:

[redacted]

Dr. Sadik Dost, Supervisor (Department of Mechanical Engineering)

[redacted]

Dr. Andrew Rowe, Co-Supervisor (Department of Mechanical Engineering)

[redacted]

Dr. George Beer, Outside Member (Department of Physics)

[redacted]

Dr. Pan Agathoklis, External Examiner (Department of Electrical and Computer Engineering)

Table of Contents

List of Tables

List of Figures

Nomenclature

a	lid unsupported outer radius (cm)
A	cross sectional area (m^2)
A_w	weld length (cm)
b	lid inner hole radius (cm)
d_b	bracket width (cm)
D	plate constant
D_0	magnet outer diameter (cm)
e	emissivity
E	Modulus of Elasticity (Pa)
E_w	weld efficiency
f	allowable weld load (Pa)
F	applied load to an interface (N)
G	Fabry factor
H	hardness of a material
H_0	magnetic field (T)
I	current (A)
j(r,z)	Kelvin distribution
k	thermal conductivity (W/m-K)
k_{ave}	average thermal conductivity (W/m-K)
k_e	electronic thermal conductivity (W/m-K)
k_{eff}	effective thermal conductivity (W/m-K)
k_g	lattice thermal conductivity (W/m-K)
k_t	thermal contact conductance (W/K)
L	magnet length (m)
L_{ave}	average length over temperature range (cm)
Lc	critical length of magnet (cm)
L_{cond}	conduction path length (cm)
Lsc	HTS length (cm)
$\dot{Q}_{Res}$	Electrical contact resistance heat (W)
L_0	Lorenz number ($A^2\Omega^2/K^2$)
L_{293}	length at 294 K (cm)
M_w	weld bending moment (N-m^2)
Mr	plate radial bending moment
P	internal pressure (Pa)
Pc	vacuum vessel collapsing pressure (Pa)
P_w	weld allowable concentrated axial load (N)
$\dot{Q}$	rate of heat flow (W)
$\dot{Q}_{cond}$	cylinder conductive heat transfer (W)
$\dot{Q}_{rad}$	radiant heat transfer (W)

r	radius (m)
R	vacuum vessel radius (cm)
R1	magnet inner bore radius (m)
R2	magnet outer radius (m)
R_c	electrical contact resistance (ohm)
Ri	vacuum vessel shell inner radius (cm)
S	stress (Pa)
S1	end capped vessel meridional stress (Pa)
S2	axial load stress (Pa)
S_a	allowable stress (Pa)
Sc	tangential hoop stress at collapsing pressure (Pa)
S_h	hoop stress (Pa)
S_t	weld tensile strength (Pa)
S_T	dimensionless temperature uncertainty
S_w	section modulus of weld lines (cm^3)
t	vessel wall thickness (cm)
T	temperature (K)
u_T	temperature uncertainty
u_R	resistive uncertainty
V	weld vertical shear (N)
w	fillet weld size (cm)
W	resultant weld force (N/m)
W_0	residual thermal resistivity (m-K/W)
W_1	Weld tension/compression force (N/m)
W_b	weld bending force (N/m)
W_i	intrinsic thermal resistivity (m-K/W)
W_s	weld vertical shear force (N/m)
y	plate deflection (cm)

Greek

α	=R2/R1
α_l	coefficient of thermal expansion (m/m-K)
β	=L/2xR1
ε	strain
λ	space factor
ν	Poisson's ratio
ω	weld leg size (cm)
ρ	electrical resistivity (ohm-m)
ρ_R	residual electrical resistivity (ohm-m)
ρ_I	ideal lattice electrical resistivity (ohm-m)
σ	electrical conductivity (1/ohm-m)
σ_P	plate bending stress

Acknowledgments

Moving from the field of physics to mechanical engineering has been very rewarding and challenging. I feel very honored to have been given this project and grateful for the experience. There are several people who I would like to thank for making the completion of this project possible:

- Dr. Sadik Dost for giving me this opportunity and allowing me the time to learn as much as I desired along the way.
- Dr. Andrew Rowe for providing me with excellent technical advice and guidance.
- Mr. Brian Lent for his help in understanding crystal growth methods and his support along the way.

A number of other students and staff contributed their time and effort including: Mr. Ray Brougham, Mr. Rodney Katz, Mr. Michael Crowle, Mr. George Csanyi-Fritz, Mr. Hamdi Sheibani, and Mr. Armando Tura.

I would also like to acknowledge the Canadian Space Agency (CSA), Redlen Crystals Ltd, Amistar Research Inc, B.C. Advanced Systems Institute, and the National Science and Engineering Research Council (NSERC) for their funding of this work and the projects associated with it.

1 Introduction

This thesis examines the design and analysis of a cryogen-free superconducting magnet system for the growth of Cadmium Zinc Telluride using the traveling heater method. In the introduction, the crystal growth method and the purpose of the magnetic field will be described. The decision to use a superconducting magnet was made by analyzing the power requirements of a conventional solenoid magnet. Also, a description of how cryogen-free superconducting magnets were made possible and the components required for a cryogen-free magnet system is included in a literature review. The superconducting magnet is then discussed along with the auxiliary systems required to operate the magnet. Finally, the design and analysis of the superconducting magnet cryostat is described.

1.1 Project Description

One of the focuses of the Crystal Growth group in the department of Mechanical Engineering and the University of Victoria is the growth of Cadmium Zinc Telluride (CdZnTe). If a practical method of growing large, homogeneous single crystals is found, this material will have several possible applications including [1]:

1. Substrate for Mercury Cadmium Telluride (HgCdTe) infrared detectors.
2. Detector in high-resolution x-ray tomography.
3. Gamma ray detector for use in nuclear medical imaging and other radiation detection devices.

HgCdTe infrared detectors are used in missile guidance systems and military target acquisition, identification and tracking. In the field of high-resolution x-ray tomography, CdZnTe is one of several candidate detector materials. Its use remains in the research and development stage. Possibly one of the most promising uses for CdZnTe is in gamma ray detectors. Gamma detectors for nuclear medical imaging are important tools in medical diagnosis because they have the ability to produce three-dimensional images and measure the internal functions of the body [1].

Presently, Silicon, Gallium Arsenide, and Germanium are the most widely used crystals in gamma ray detectors. However, due to their low absorption and high thermal noise, these crystals limit the quality of the images obtained [1]. A new, high quality, detector material is needed to advance this field of research. CdZnTe is an ideal gamma ray detector material because of its large energy band gap, low thermal conductivity, and high electrical resistivity at room temperature. Unfortunately, CdZnTe is difficult to grow into large homogeneous single crystals. A promising technique for the growth of Cadmium Zinc Telluride is the Traveling Heater Method (THM).

In THM, crystal growth is induced by supersaturating a solution of the growth material. Supersaturation is created by lowering the temperature of the solution at its interface with the seed crystal. The solute concentration is maintained by dissolving source material at the solution-source interface using increased temperature. As the growth interface progresses forward from the seed, the low temperature region at the growth interface and the high temperature region at the source interface must move at the same rate. These interfaces are shown in Figure 1. Since this growth method uses lower temperatures than other growth methods, it can produce crystals with less thermal stress and therefore fewer defects.

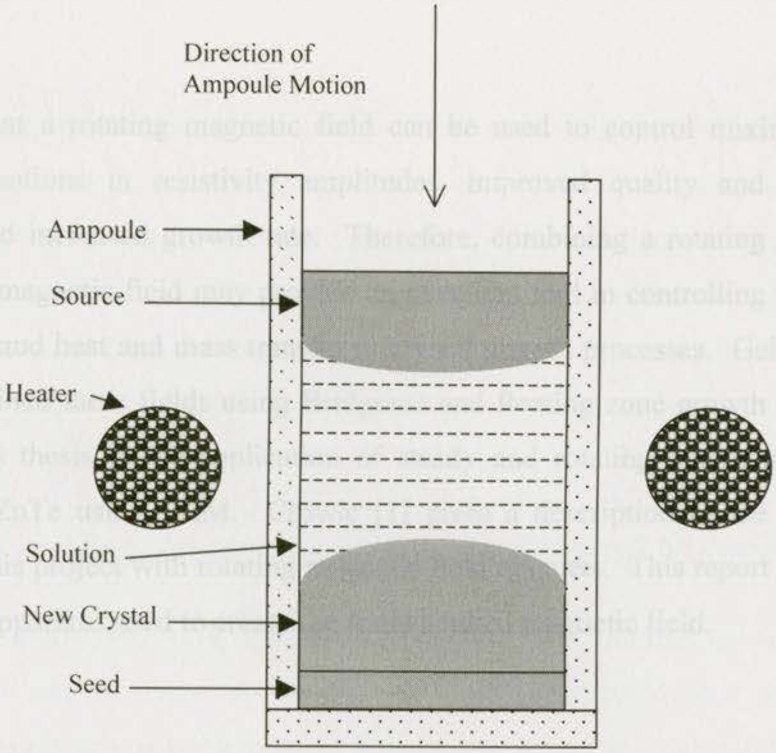

Figure 1: THM growth apparatus. The heaters remain stationary and the ampoule moves.

There are, however, several problems with the THM method. One problem is that the growth rate is slow. Another problem (in most crystal growth methods) is the existence of density driven convection currents. These currents may result in a concave shape of the growth interface [2], which can lead to flaws or polycrystalline materials due to trapped impurities and dopents. One way of reducing these currents is by creating an optimal thermal temperature gradient in the crystal solution [1]. Also, growth by several methods in microgravity conditions has been proven [3-5] to significantly reduce the density driven currents, leading to a closer approximation to the desired diffusion-controlled growth and improved crystal uniformity. On Earth, an externally applied steady vertical magnetic field has been demonstrated, both experimentally [5,6] and numerically [7,8], to simulate microgravity growth conditions. Thus, experimenting with this magnetic field will assist in defining the optimum THM growth conditions for future space-processing opportunities.

One negative effect of an applied magnetic field is that the growth rate is reduced [9]. This can be attributed to a decrease in mixing due to a reduction in convection. A rotating magnetic field may be the solution to this problem. Several researchers [2,5,10] have found that a rotating magnetic field can be used to control mixing resulting in reduced fluctuations in resistivity amplitudes, improved quality and compositional uniformity, and increased growth rate. Therefore, combining a rotating magnetic field with a steady magnetic field may provide an excellent tool in controlling the parameters of convection and heat and mass transfer in crystal growth processes. Gelfgat *et al.* [11] recently combined these fields using Bridgman and floating zone growth methods. The subject of this thesis is the application of steady and rotating magnetic fields to the growth of CdZnTe using THM. Crowle [1] gives a description of the THM furnace designed for this project with rotating magnetic field magnets. This report focuses on the design of the apparatus used to create the static applied magnetic field.

1.2 Required Magnetic Field Strength and Uniformity

As mentioned previously, a static magnetic field can beneficially reduce gravitational convection currents; however, if the magnetic field strength is too high, adverse effects can arise. A three-dimensional model of the effect of an applied magnetic field on the flow structures of GaAs in liquid phase electroepitaxy (LPEE) (another solution growth method) has shown that for field strengths greater than 0.3 Tesla the crystal growth becomes unstable [12]. Experimental results of LPEE growth of GaAs show that this maximum field strength is actually 0.45 Tesla [13]. The difference between the experimental and theoretical maximum field values is due to various assumptions and simplifications made in the model.

A numerical study of the growth using THM under a fixed magnetic field has also been performed [9]. The results show that for fields greater than 1 Tesla, compositional non-uniformity increases significantly and the growth rate is reduced. From these results it was decided that the magnet should be designed to produce a maximum field of 1.25 Tesla.

The effects of deviation from axisymmetry and of a non-uniform field distribution have also been numerically investigated [12]. Results show that for a non-uniformity level of 6%, the changes in the crystal flow field are small. Thus, for magnetic fields less than 1 Tesla, small deviations in uniformity are not expected to significantly influence crystal growth quality. However, for larger deviations or larger magnetic fields, these effects become more significant [9,12].

1.3 Resistive Magnet versus Superconducting Magnet

To create a magnetic field with sufficient strength over the volumes needed to contain a THM unit, one can use either a conventional resistive solenoid or a superconducting magnet. To determine if using a resistive magnet is practical, the size and power required by the magnet must be calculated.

For resistive magnets, the power, W, required to create a 1.25 Tesla field is given by

$$W = \frac{\rho R1}{\lambda}\left(\frac{1\times10^{6} H_0}{G}\right)^2, \tag{1}$$

where ρ is the electrical resistivity of the material in ohm-m, $R1$ is the inner bore radius in meters, H_0 is the field in Tesla, 1×10^6 is a unit conversion factor in A^2/N, λ is the space factor or the ratio of the active section of winding to the total section of the winding and G is the Fabry factor which is a combination of all the geometry terms. G is given by

$$G = \frac{1}{5}\left(\frac{2\pi\beta}{\alpha^2 - 1}\right)^{1/2} \ln\frac{\alpha + (\alpha^2 + \beta^2)^{1/2}}{1 + (1 + \beta^2)^{1/2}}, \tag{2}$$

where

$$\beta = L/2R1, \qquad \alpha = R2/R1, \tag{3}$$

where L is the length of the magnet in meters and $R2$ is the outer radius in meters [14]. For a uniform current density solenoid, G has a maximum of 0.179 at α=3 and β=2 making the field maximum for the least amount of power. Using non-uniform current density coils can improve the efficiency of the magnet. If two coils are used, for example, the optimum G factor becomes 0.207 resulting in a 33% decrease in power.

The maximum theoretical improvement in efficiency for an electromagnet is created if the current is distributed in the Kelvin distribution given by

$$j(r,z)=\left(\frac{1}{R1^2}\right)\frac{\sin^3\theta}{(r/R1)^2}. \tag{4}$$

This distribution results in a maximum G of 0.257, however it can only be reached with a magnet that has infinite dimensions. A practical sized magnet could be achieved with a Kelvin distribution G factor of 0.23 at α=4.5 and β=3. One method of designing a magnet that comes close to achieving the Kelvin distribution is using variable thickness disks (Bitter disks). It must be remembered, however, that even though the theoretical efficiency is increased the actual efficiency will decrease with higher current densities once the magnet heats up due to joule heating. If cooling holes are required within the magnet to keep the temperature down this will also decrease the efficiency.

Table 1 shows the results of using Equation 1 with a magnetic field of 1.25 Tesla and electrical resistivity of copper of 1.67×10^{-8} ohm-m for different values of G. The inner radius, $R1$, is chosen to be 0.64 cm (0.25 in) larger than the outside furnace radius of 16.1 cm (6.35 in). A λ of 0.7 is chosen as a realistic space factor.

Case	G	alpha	beta	R1 (cm)	R2 (cm)	L (cm)	Power (kW)
Uniform Coil	0.178	4.5	3	16.8	50.3	67.1	195
Kelvin	0.23	3	2	16.8	75.4	100.6	118

Table 1: Calculated power required to produce a field of 1.25 T for different solenoid magnets.

This amount of power is extreme. The set-up cost of a system that produces over 100 kW of power might be similar to the superconducting magnet system, however, the long term operating costs would be much higher. Also the cooling requirements of the solenoid magnet would be tremendous. The crystals must grow continuously for several days making the power and cooling requirements of the solenoid system unreasonable. In view of these difficulties, a superconducting magnet is considered to be the best choice for this project.

1.4 Superconducting Magnet Design Literature Review

Superconducting magnet systems generally operate at liquid helium temperatures (4.2 K). However, it is difficult and expensive to continuously operate conventional liquid helium cooled superconducting magnets over many hours because of a limited supply and high price of helium. Systems that do not rely on cryogens are much more practical for the demands of crystal growth. Cryogen-free systems were made realistically possible by the development of reliable two-stage Gifford-McMahon (GM) cryocoolers able to reach 40 K on the first stage and 4 K on the second stage. Another development that made conduction cooling possible was the development of high temperature superconductor (HTS) leads, significantly reducing heat transfer to the magnet.

Several companies sell cryogen-free superconducting magnets including Oxford Instruments, American Magnetics, Janis Research, and CRYO Industries of America, Inc. [15-18]. Descriptions of the design of cryogen-free superconducting magnets have been published by many scientists [19-30]. For the THM furnace, a large bore (38.1 cm) is required in the superconducting magnet. Large bore cryogen free magnets have been previously designed mainly for magnetic resonance imaging (MRI) applications [24,30].

In each design, the cryocooled magnet is surrounded by some form of radiation shield attached to the first stage of a cryocooler and contained in a vacuum vessel with a room temperature bore. The magnet and cryocooler are thermally connected with flexible copper connectors and the thermal contacts are augmented with indium foil. Current leads are a combination of a copper section and a high temperature superconducting (HTS) lead section. Aluminum nitride is used as an electrically insulating thermal conductor between the cryocooler and the magnet leads [22,28]. Supports for many of the smaller magnets are vertical cylinders made from glass fibre reinforced epoxy (GFRP) however some also use radial supports [20,24,25,31].

Since the cool-down time of cryocooled superconducting magnets can be very slow, thermal switches have been developed to decrease this time [32]. The switch connects the first and the second stages of the two-stage cryocooler to take advantage of the high power of the first stage to cool the second stage faster. Once the entire apparatus reaches the first stage temperatures, the switch is turned off, or disconnected, so that the second stage can cool the magnet to the appropriate cryogenic temperature. However, for this experiment, cool-down time is not important and therefore thermal switches are not employed.

1.5 Superconducting Magnet Description

A field strength of 1.25 Tesla is approximated as the maximum flux density required to simulate microgravity in the THM crystal growth. A superconducting solenoid rated for this field strength and with a clear bore diameter of 38.1 cm (15 in) was designed and built by American Magnetics, Inc. [15] for this project. The coil is wound using conductors comprised of many filaments of NbTi superconducting material embedded in a copper matrix. The field uniformity of this magnet in the 5.08 cm (2 in) cubed area of crystal growth is below the predicted acceptable value of 6% as shown by the percent field deviation plot in Figure 2.

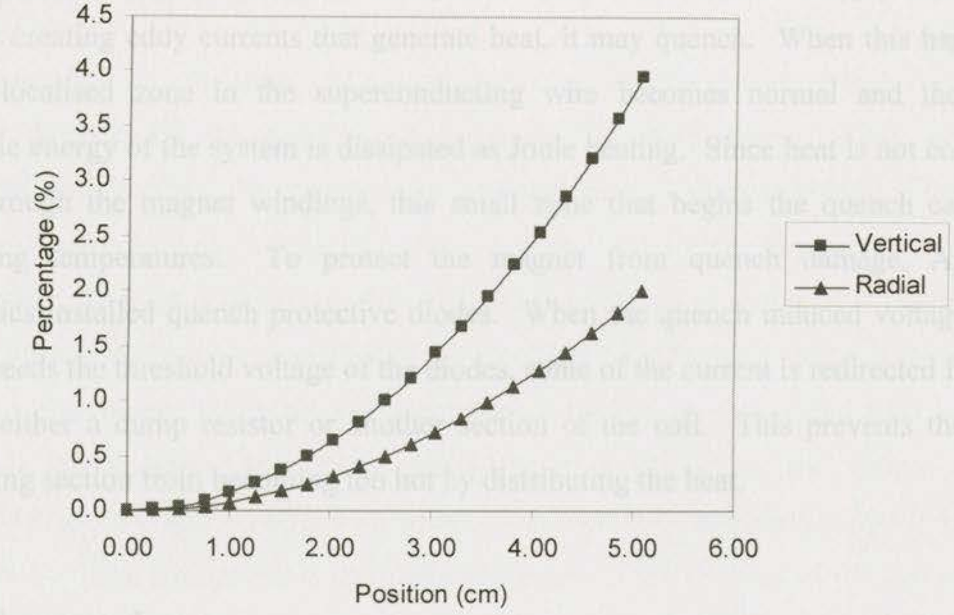

Figure 2: Vertical and radial magnetic field deviation from 1.25 T center position (r=0,z=0).

To operate the magnet at 1.25 Tesla, the magnet must first be cooled to 4.2 K then charged with a current of 158.3 Amps. The work described here encompasses the design and construction of an apparatus to create this 4.2 K environment using a cryocooler. The magnet is charged and discharged with a specialised magnet power supply. This supply has quench detection and protection, a programmable ramping rate and adjustable current and voltage limits.

After the magnet has been energised, the power supply may be turned off with the magnet switched to persistent mode. The persistent mode is created by short circuiting the magnet with a section of superconducting wire contained in a persistent switch. When the magnet is charging, this superconducting wire is heated to its normal resistive state so that voltage can be established across the terminals. Once the desired field is reached, the heater is turned off and the persistent switch shorts the magnet creating a complete superconducting loop.

If the magnet is not cold enough, is charged too quickly or the power supply is not stable thereby creating eddy currents that generate heat, it may quench. When this happens, a small, localised zone in the superconducting wire becomes normal and the stored magnetic energy of the system is dissipated as Joule heating. Since heat is not conducted well through the magnet windings, this small zone that begins the quench can reach damaging temperatures. To protect the magnet from quench damage, American Magnetics installed quench protective diodes. When the quench induced voltage of the coil exceeds the threshold voltage of the diodes, some of the current is redirected from the coil to either a dump resistor or another section of the coil. This prevents the initial quenching section from becoming too hot by distributing the heat.

1.6 Cryocooler

The cryocooler used is a RDK-415D Sumitomo (SHI) 4 K refrigerator from Janis Research Company [33]. It operates using a modified Gifford-McMahon refrigeration cycle with two stages. The first stage can extract 45 Watts of heat at 40 K and the second stage can extract 1.5 Watts of heat at 4.2 K. A photo of the cryocooler is shown in Figure 3.

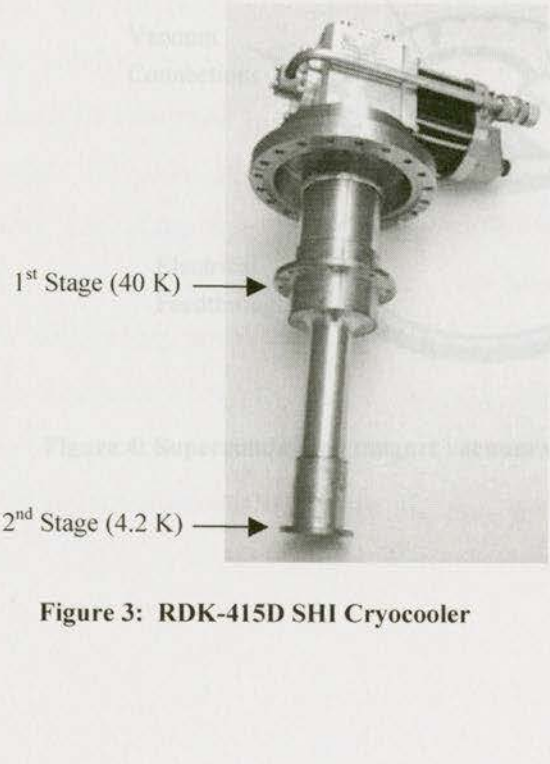

Figure 3: RDK-415D SHI Cryocooler

1.7 Design Outline

This report describes the design of a superconducting magnet system. Many components must be designed for the operation of the superconducting magnet. First, to achieve cryogenic temperatures, the magnet must be enclosed in a vacuum vessel. This vessel, shown in Figure 4, must have an inner bore that allows the THM furnace to be placed in the centre of the magnet and it can have an outer diameter no greater than 81.3 cm (32 in). The lid of this vessel must have flanges for electrical feedthroughs, vacuum connections, and for a cryocooler. Inside the vacuum vessel, a thermal shield layered with insulation surrounds the magnet. This shield, consisting of a strongback and copper shell, is suspended from the lid of the vacuum vessel using thermally insulating supports as shown in Figure 5. The strongback is thermally connected to the 1st stage of the cryocooler so that the heat shield remains at approximately 40 K. Finally, the superconducting magnet is also covered in insulation and is hung from the strongback and thermally connected to the 2nd stage of the cryocooler as sketched in Figure 5. Current leads for the magnet pass through the lid and the strongback and are also thermally connected to the 2nd stage of the cryocooler.

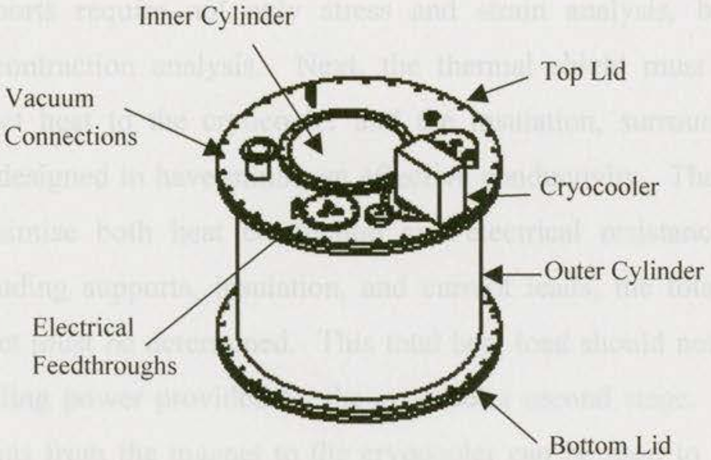

Figure 4: Superconducting magnet vacuum vessel.

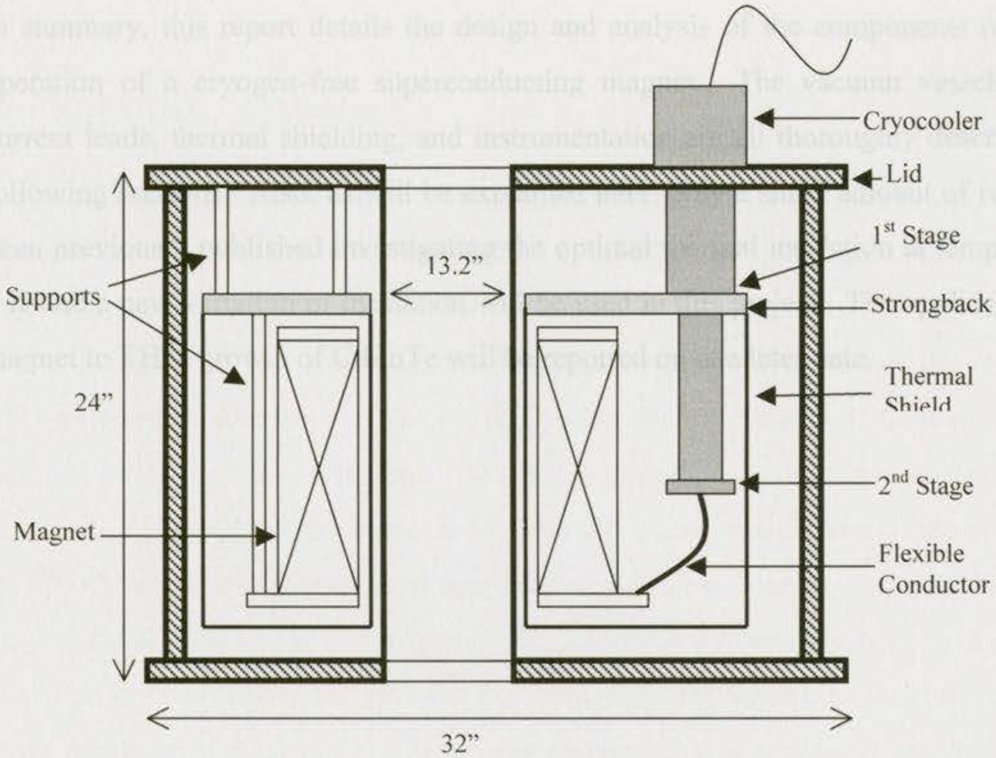

Figure 5: Cross-section sketch of superconducting magnet system.

In designing the complete system, many factors must be considered. For the vacuum vessel, the stress and strain on the vessel must be used to determine the thickness of the parts. The supports require not only stress and strain analysis, but also thermal conduction and contraction analysis. Next, the thermal shield must be designed to effectively conduct heat to the cryocooler and the insulation, surrounding it and the magnet, must be designed to have minimum effective conductivity. The magnet current leads should minimise both heat conduction and electrical resistance. From these components, including supports, insulation, and current leads, the total heat load that reaches the magnet must be determined. This total heat load should not be greater than the 1.5 W of cooling power provided by the cryocooler second stage. Analysis of the thermal connections from the magnet to the cryocooler can be used to approximate the steady-state superconducting magnet temperature. To verify the actual state of the magnet, temperature sensors are placed at various locations on the magnet and shield.

In summary, this report details the design and analysis of the components required for operation of a cryogen-free superconducting magnet. The vacuum vessel, supports, current leads, thermal shielding, and instrumentation are all thoroughly described in the following sections. Also, as will be explained later, only a small amount of reports have been previously published investigating the optimal thermal insulation at temperatures of 4 K and a new variation of insulation will be used in this project. The application of this magnet to THM growth of CdZnTe will be reported on at a later date.

2 Vacuum Vessel

The outer shell of the superconducting magnet apparatus is called the vacuum vessel. It is composed of two flat heads or lids, an outer cylindrical shell, an inner cylindrical shell, or bore, and welded flanges to hold the pieces together. A schematic of the vacuum vessel is shown in Figure 6. The outer radius is limited to 81.3 cm (32 in) so that the vessel will fit through standard doorways. Once the flanges are designed with sufficient space for an o-ring and bolts, the outer cylinder of the shell is limited to an outside diameter of 69.9 cm (27.5 in). The height of the vessel is 61.0 cm (24 inches) and is determined mostly by the cryocooler and the requirement of approximately 5-8 cm of space between the bottom of the magnet and the inside of the bottom lid. The inner cylinder needs to have a minimum diameter that will allow the 32.3 cm (12.7 in) diameter furnace to fit in the center. An inner diameter of 33.5 cm (13.2 in) was chosen to give room for convective cooling between the furnace and the vessel shell. All of the components must be made of a suitably strong material with low magnetic permeability. A safety factor of at least four determines the specific dimensions of each component. This analysis will be described in the following sections.

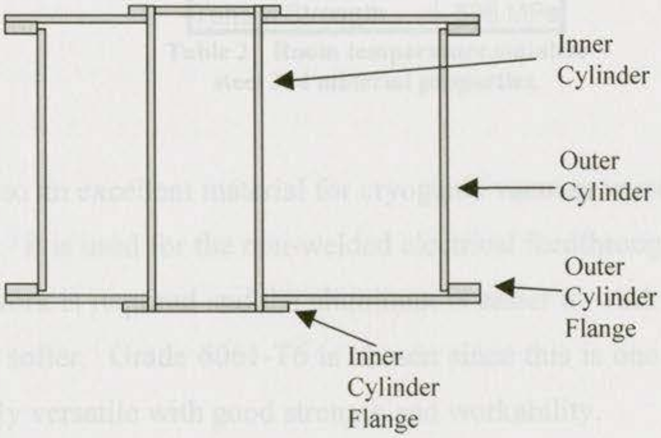

Figure 6: Cross section of outer shell components of the superconducting magnet.

2.1 Materials

The magnet vessel must be made of a material that has high strength, is nonmagnetic, and is relatively easy to work with. The outer vessel will generally remain at room temperature however it is also a good idea for the material to have cryogenic compatibility. Some common materials that have these properties are generally face-centered cubic (fcc) metals and alloys and include nickel steel (> 29 % nickel), austenitic stainless steel, copper, nickel, and aluminum. Of these materials the austenitic stainless steel has all the desirable vessel properties including it remains ductile and strong over the entire cryogenic range of temperatures. Furthermore, unlike many of the ferritic steels, it is nonmagnetic. The most commonly used austenitic stainless steels are 18-8, including 304, and 316 stainless steel. The 316 stainless steel contains an addition of molybdenum for improved corrosion resistance but this can make welding more difficult, the material is more expensive, and more difficult to machine. For this reason, stainless steel 304 was chosen. Material properties of stainless steel 304 are shown in Table 2.

Material	304 SS
Modulus of Elasticity	193 GPa
Modulus of Rigidity	86 GPa
Poisson Ratio	0.3
Yield Strength	228 MPa
Tensile Strength	586 MPa

Table 2: Room temperature stainless steel 304 material properties.

Aluminum is also an excellent material for cryogenic vacuum vessels however it is not as easily weldable. It is used for the non-welded electrical feedthrough flanges on the vessel since detailed work is required and the aluminum is easier to work with than the stainless steel since it is softer. Grade 6061-T6 is chosen since this is one of the least expensive grades yet highly versatile with good strength and workability.

2.2 Shell Design

Although subject to lower stresses than positive pressure chambers, vacuum vessel design is also governed by various standard codes. When designing a pressure vessel according to the ASME Boiler and Pressure Vessel Code, Section VIII, Division 1 [34], all major loads on the vessel must be considered. In this work, the vacuum vessel will be operating under atmospheric pressure, approximately 103 KPa (15 psi). The walls of the vessel will remain at room temperature since they are well insulated from the cryogenic environment. Therefore there should not be any concerns with thermal contraction. The lid ends of the vessel are flat and these create an axial load on the cylinder due to atmospheric pressure on the lids along with the weight supported by the vessel. The main goal for the shell design is to ensure that the combined load due to pressure and weight does not exceed the maximum allowable stress. The lids and cylindrical walls of the vessel will each be analyzed separately.

2.3 Outer Cylinder

The outer cylinder can be analyzed as a cylindrical vessel under external pressure. To reduce cost, the structure is designed as a thin-walled vessel. By convention, this means that the ratio of the outside diameter, D_O, to the wall thickness, t, is greater than 10. Because thin-walled vessels under external pressure fail at stresses much lower than the yield strength due to instability of the shell, extra care is required in choosing an appropriate wall thickness. In the ASME Code there are specific equations for thin walled vessels that must be adhered to. The equations that are used to determine the collapsing pressure and working pressure of a vessel for a particular wall thickness depend on the length of the cylinder. Short cylinders have their own set of equations.

A short cylinder is one in which the unsupported length is much less than the critical length, Lc, given by

$$Lc = 1.14\left(1-\nu^2\right)^{1/4} D_O (D_O / t)^{1/2}, \tag{5}$$

where ν is the Poisson ratio. The length of the magnet vessel is given in Table 3 and the calculated critical length is given in Table 4 for wall thickness of 0.32 cm (0.125 in) and 0.48 cm (0.1875 in). The critical lengths are a great deal larger than the design length and therefore the vessel is considered short. This means that the cylinder will fail by plastic yielding alone at high stresses close to the yield strength of the material whereas if the cylinder were long, failure by buckling would also be a concern.

For short cylinders, Bednar [35] gives the following formula for the critical pressure Pc (collapsing pressure):

$$Pc = \frac{2.42E}{(1-\nu^2)^{3/2}}\left[\frac{(t/D_O)^{2.5}}{(L/D_O) - 0.45(t/D_O)^{0.5}}\right]. \tag{6}$$

where E is the modulus of elasticity or Young's modulus. Critical pressure is calculated for thicknesses of 0.32 cm (0.125 in) and 0.48 cm (0.1875 in) and the results are in Table 4. Values obtained for these thicknesses are 10 and 27 times respectively larger than the operating pressure of 103 KPa. These are considerable safety factors.

A more accurate method for determining the collapsing pressure is given by the ASME Code. In this method the collapsing pressure is written in terms of the tangential stress using the hoop formula

$$Pc = 2Sc(t / D_O), \tag{7}$$

where Sc is the tangential hoop stress at collapse. Assuming the term $0.45(t/D_O)^{0.5}$ can be neglected from Equation 6 and using a Poisson's ratio of 0.3, substituting Equation 6 into Equation 7 gives

$$Sc / E = 1.40(t / D_O)^{1.5} / (L / D_O). \tag{8}$$

This is defined as factor A and is plotted in Fig. UGO-28.0 of the ASME Boiler and Pressure Vessel Code [34]. This equation can be used for all materials. To find the collapsing pressure at a certain factor A for a specific material, a material chart must be referred to. This material chart is actually a strain-stress curve for the material. In the ASME Code material charts, factor A is plotted against a factor B, where factor B is equivalent to $Sc/2=PaD_O/t$, and Pa is the allowable working pressure and is four times less than the collapsing pressure. For stainless steel 304, the material chart in Figure UHA-28.1 of the Code [34],[35], must be used. This method is more accurate than using Equation 6 since it takes into account the nonlinear relationship between strain and stress. The resulting allowable pressure and collapsing pressure determined from factors A and B are also shown in Table 4. The Code gives B values in psi so both the psi value and the converted MPa value are given in the table. This method finds a much lower collapsing pressure than calculated for a vessel thickness of 0.48 cm (0.1875 in) but agrees more closely with the 0.32 cm (0.125 in) calculated value. Although the allowable working pressure of the 0.32 cm thickness is twice as large as required for the vacuum vessel, a thinner wall would be difficult to machine and weld so the 0.32 cm thickness was chosen.

Unsupported Length	54.1cm
Outside Diameter	69.9cm

Table 3: Outer cylinder dimensions of the superconducting magnet vessel.

Thickness (cm)	L/D0	D0/t	Critical Length (cm)	Pc (MPa) (calculated)	Factor A, Sc/E	Factor B, Sc/2 (psi)	Factor B (MPa)	Pa (MPa) (from A and B)	Pc (MPa)
0.48	0.77	147	960	2.81	0.0009	8800	60.7	414	1.66
0.32	0.77	220	1180	1.01	0.0006	7100	50.0	223	0.89

Table 4: Critical length, allowable working pressure, and collapsing pressure for different thicknesses of the vacuum vessel outer cylinder.

In combination with the tangential stress due to external pressure, the outer cylinder of the vessel also has two sources of axial, or meridional, stress including the stress caused by the atmospheric pressure on the capped ends and the stress caused by the weight of the components resting on the edge of the outer cylinder. For a pressure vessel with its ends capped, the meridional stress [36] is given by

$$S1 = \frac{PR}{2t}, \tag{9}$$

where R is the radius of the vessel, P is the pressure and t is the wall thickness. For a pressure of 103 KPa, this stress is 5.64 MPa as shown in Table 5. The stress, *S2*, caused by the approximately 1790 N (400 lb)[1] load of components on the vessel shell (refer to Table 30 in Appendix-A) is calculated by dividing the load by the area of the end of the vessel. *S2* is also shown in Table 5. These stresses are both significantly lower than the 227 GPa yield strength of stainless steel 304.

Thickness (cm)	Capped S1 (MPa)	End Area (cm^2)	Axial Load Stress S2 (KPa)
0.32	5.64	69.7	257

Table 5: Capped pressure and load axial stresses.

2.4 Inner Cylinder

The inner cylinder, or inner bore, of the vacuum vessel is under uniform internal pressure. In this case, the hoop stress still applies and is again given by

$$S_h = \frac{PR}{t}, \tag{10}$$

where t is the thickness of the shell, P is the internal pressure and R is the radius. Expressing this equation in terms of the inner radius Ri gives

$$S_h = P(Ri + 0.5t)/t\,. \tag{11}$$

---

[1] The calculated load of 357 lb was increased to 400 lb to ensure an excellent safety factor.

The hoop stress, S_h, can also be expressed in terms of the maximum allowable stress S_a and the weld efficiency E_w where

$$S_h = S_a E_w . \tag{12}$$

The allowable stress is approximately ¼ the minimum ultimate strength (tensile strength) of material [37] and the weld efficiency can be determined from the Code section UW-12 [34]. Solving Equation 11 for t and substituting it into Equation 10, results in the equation given by the ASME Boiler and Pressure Vessel Code [34] for determining the minimum thickness of a vessel with longitudinal joints:

$$t = \frac{PR}{S_a E_w - 0.6P}, \tag{13}$$

using $0.6P$ instead of $0.5P$.

Results of using Equation 13 with the bore dimensions shown in Table 6, are given in Table 7 where S_a=586/4=147 MPa for 304 SS and the weld efficiency of a double-welded butt joint that has had no examination is estimated as 70%. The minimum thickness of the inner cylinder at an operating pressure of 103 KPa is 0.018 cm (0.007 in). Once more, the thickness must be chosen to be 0.32 cm (0.125 in) so that it is easy to work with and weld. At this thickness, the operating pressure can be over 18 times higher than atmospheric pressure. Again, this creates an extremely large safety factor.

Unsupported Length	60.3cm
Inside Diameter	33.5cm

Table 6: Inner cylinder dimensions of the superconducting magnet vessel.

P (KPa)	Diameter (cm)	Allowable Stress (MPa)	Weld Efficiency (%)	t (cm)
103	33.5	146	70	0.018
1920	33.5	146	70	0.32

Table 7: Inner cylinder minimum thickness with different internal pressures.

The ends of the inner cylinder are not capped and there is no axial load and therefore no significant axial stress.

2.5 Lids

The lids are 81.3 cm (32 in) in outer diameter and have a 34.2 cm (13.45 in) diameter hole, offset 4.8 cm (1.875 in) from the center, as shown in Figure 7.

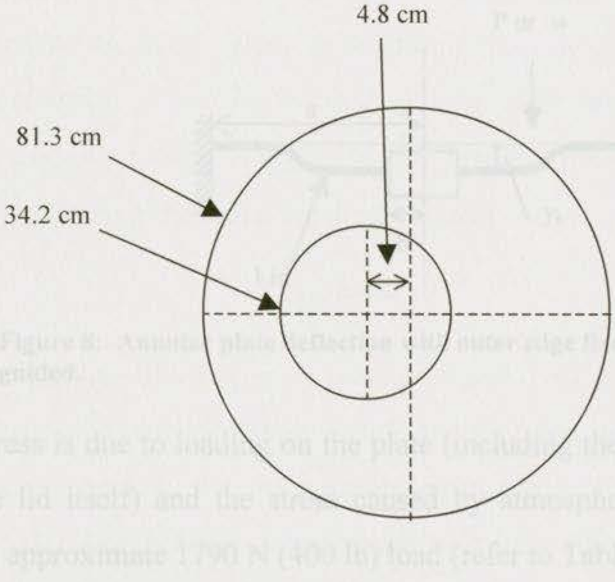

Figure 7: Sketch of vacuum vessel lid.

The hole is for the furnace. The opening is offset due to the cryocooler needing extra space on the outside of the magnet. The lid thickness is determined using an unsupported outer radius, of *a*=35.6 cm (14 in). These as well as the other parameters, including the hole radius *b*, used in the lid stress calculations are shown in Table 8.

b	17.1cm
a	35.6cm
Modulus of Elasticity E	193GPa
Poisson's Ratio ν	0.3
Total load	1790N

Table 8: Parameters used in lid thickness calculations.

The ASME code does not address the minimum thickness of bolted flat heads. Instead, the stress and deflections for the flat plates are analyzed using *Roark's Formulas for Stress & Strain* [36]. Specific equations are determined by the plate edge conditions. For this work, the boundary conditions most closely resemble a plate with its outer edge fixed and its inner edge guided as shown in Figure 8. Also, the center hole in the lid is assumed to be concentric since there are no formulas included for off-center holes. This assumption should not cause a large underestimation of the stresses involved since the offset is small compared to the size of the lid.

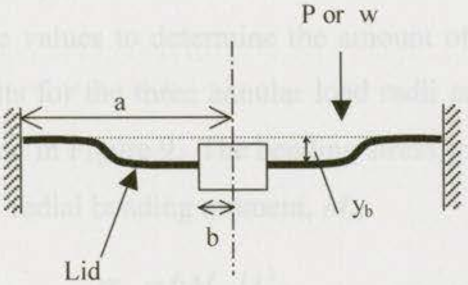

Figure 8: Annular plate deflection with outer edge fixed, inner edge guided.

The total stress is due to loading on the plate (including the mass of components and the mass of the lid itself) and the stress caused by atmospheric pressure. In the case of loading, the approximate 1790 N (400 lb) load (refer to Table 30 Appendix-A) is assumed to create a uniform line load induced from the mass hanging from the supports, the mass of components attached to the lid, and the mass of the lid itself (182 kg). The inner supports are at a radius of 26.9 cm (10.61 in) around the center hole. This is set to the radial location of the unit line loading, r_0. The r_0 is also set to 20.3 cm (8 in) and 17.8 cm (7 in) respectively to test more extreme center loading possibilities as is recommended [36]. Annular load, w, is then determined by dividing the total load of 1790 N by the effective circumference, $2\pi r_0$.

In the second case, where stress is caused by atmospheric pressure, the force is uniformly distributed over the plate from b to a. Initially, b is set to 17.1 cm (6.725 in) as was used in the previous case. To check that the offset of 4.7 (1.875 in) will not have a great effect, the radius of the hole is decreased by the offset to 12.3 cm (4.85 in).

For these two cases, the deflection, y, multiplied by a plate constant, D, given by

$$D = Et^3 / 12(1 - \nu^2), \qquad (14)$$

where E is Young's modulus, t is the plate thickness and ν is Poisson's ratio, is calculated at incremental radial positions from a to b. Once the radial position of maximum deflection is determined, the plate constant D is evaluated for different plate thicknesses and yD is divided by these values to determine the amount of deflection in centimeters. Maximum deflection results for the three annular load radii and for the pressure load at different b values are plotted in Figure 9. The bending stress, σ_p, versus plate thickness, t, is also calculated using the radial bending moment, M_r,

$$\sigma_p = 6M_r / t^2, \qquad (15)$$

where M_r is calculated for positions between a and b and the maximum value position is selected. Maximum bending stress results for the three annular load radii and for the vacuum pressure load at different b values are plotted in Figure 10. Note that equations for the deflection and bending moments are very long and are, therefore, not reproduced in this thesis.

The results in Figure 9 and Figure 10 show that the deflection and stress due to loading is negligible compared to the results due to the atmospheric pressure. In addition, for thicknesses greater than 1.5 cm the slopes of the plots are significantly decreased. At a lid thickness of 1.6 cm (0.63 in) and b= 12.3 cm (4.85 in) the maximum deflection is 0.015 cm and the maximum bending stress is 27.6 MPa. These are acceptable values so a thickness of 1.6 cm is chosen.

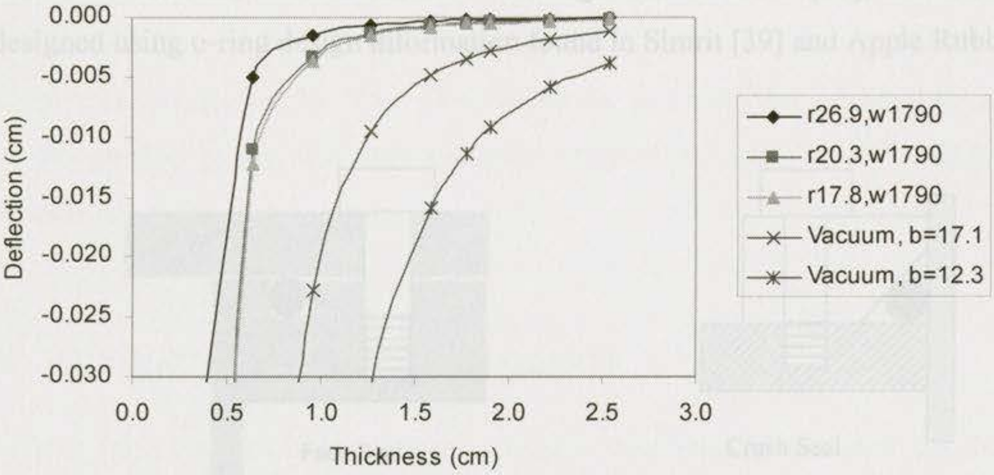

Figure 9: Deflection of the lid at radius r and b (cm) due to load, w (N), and atmospheric pressure for different thicknesses.

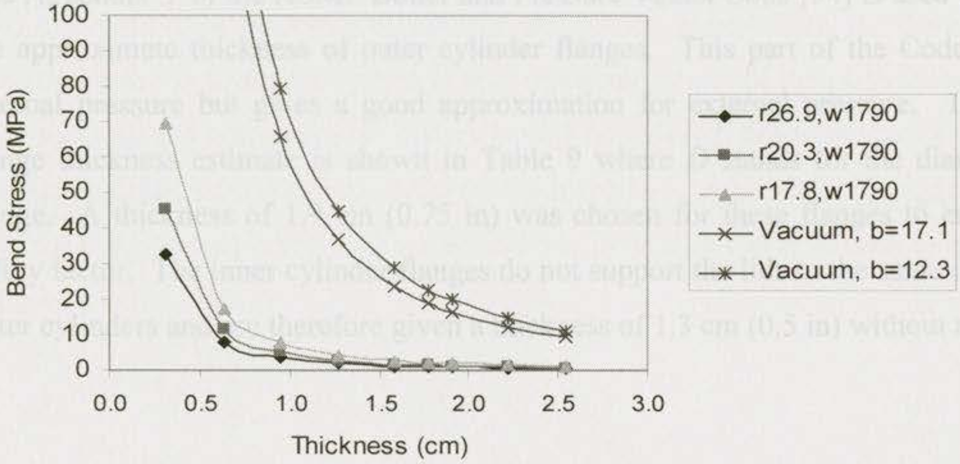

Figure 10: Maximum bending stress in the lid at r and b (cm) due to load, w (N), and atmospheric pressure for various plate thicknesses.

2.6 Flanges and o-rings

Two types of flanges are required for the system. The outer cylinder and one end of the inner cylinder have face seal flanges. A removable seal, the static crush seal, is used on the other end of the inner cylinder so that it can be inserted through the lid holes. Diagrams of these seals are shown in Figure 11. The face seal flanges are designed using

Parker Seals software called inPHorm^{TM} O-Rings Version 2.0.2. [38], and the crush seal is designed using o-ring design information found in Simrit [39] and Apple Rubber [40].

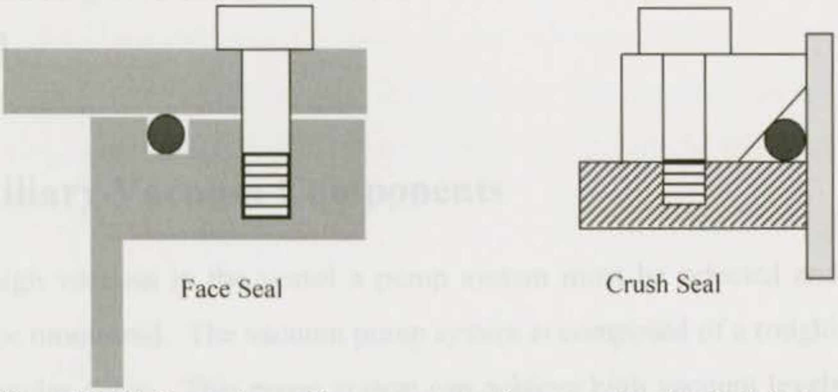

Figure 11: O-ring seals used in superconducting magnet outer shell design.

The Appendix Y of the ASME Boiler and Pressure Vessel Code [34] is used to determine the approximate thickness of outer cylinder flanges. This part of the Code is only for internal pressure but gives a good approximation for external pressure. The resulting flange thickness estimate is shown in Table 9 where *D* stands for the diameter of the flange. A thickness of 1.9 cm (0.75 in) was chosen for these flanges to ensure a high safety factor. The inner cylinder flanges do not support the lids to the same degree as the outer cylinders and are therefore given a thickness of 1.3 cm (0.5 in) without analysis.

Pressure (KPa)	Outside D (cm)	Inside D (cm)	Bolt Circle D (cm)	Mean D of o-ring (cm)	Bolt Load (kN)	Number of Bolts	Allowable Stress (MPa)	Flange Thickness (cm)
103	81.3	69.9	78.2	74.4	456	32	146	1.55

Table 9: Flange Thickness Estimate using ASME Boiler and Pressure Vessel Code for flat face flanges.

2.7 Welds

To fabricate the vessel cylinders, stainless steel is rolled and the butt joint created is welded inside and outside using a gas tungsten arc welding (GTAW) process. These welds can have an efficiency of 100% (determined by radiograph inspection). In this case, the welds are not radiographed since examination is not mandatory for vacuum vessels according to ASME boiler and pressure vessel code. Therefore, the weld efficiency is assumed to be 70%. The welds for attaching the cylinders to the flanges were designed as groove and fillet welds as shown in drawings SM-07D and SM-10D in Appendix-D.

2.8 Auxiliary Vacuum Components

To create high vacuum in the vessel a pump system must be selected and the vacuum level must be monitored. The vacuum pump system is composed of a roughing pump and a turbomolecular pump. This pump system can achieve high vacuum levels of 1×10^{-6} to 1×10^{-7} Torr as long as the outgassing from the vessel is minimal. To keep outgassing low, materials must be selected carefully and all the components of the vacuum vessel must be clean. Because the system is also cryogenic, many of the particles will condense onto surfaces and outgassing of materials will be reduced, however, care should still be taken in material selection, especially for the insulation. A thermocouple gauge is used to detect rough vacuum levels and a cold cathode ionisation gauge is used to measure high vacuum levels.

3 Support Design

Supports are required to hang the magnet from the strongback and suspend the strongback from the lid of the vacuum vessel. Because the superconducting magnet will have a furnace placed in its centre with rotating field magnets, the supports must also prevent the superconducting magnet from horizontal movement due to possible magnetic forces. The positions of the supports are shown in Figure 12.

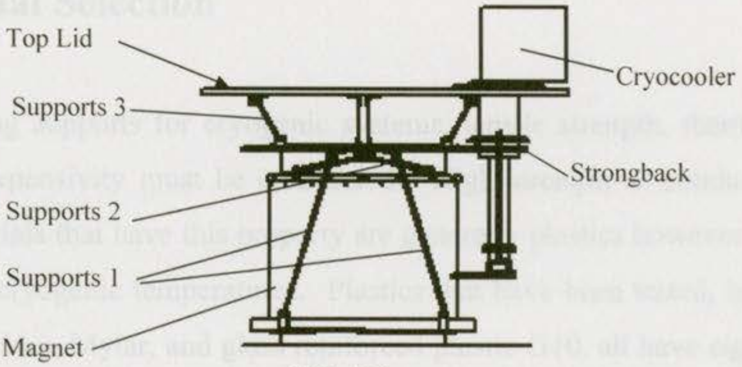

Side View

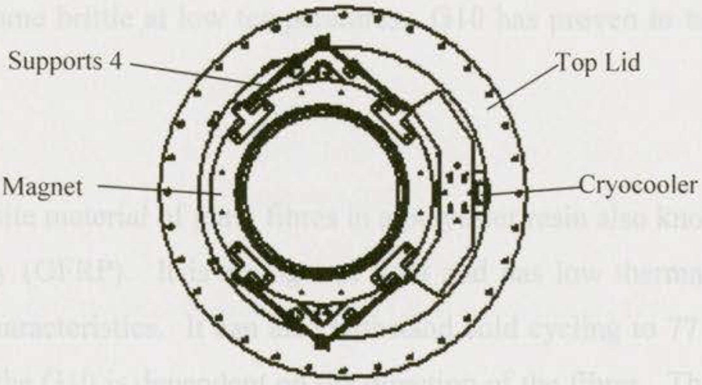

Bottom View

Figure 12: Side and bottom views of superconducting magnet supports.

Two key requirements for the supports are high strength and low thermal conductivity. The material used must be carefully selected so that it performs well at cryogenic temperatures and in vacuum. Once the material is chosen, the stress on the supports must be calculated. A specified cross section that minimizes thermal conduction but still can support the weight must then be determined. Further stress is also caused by thermal contraction during cooling and this must also be examined. The total heat transfer is then calculated to ensure that the cryocooler can handle the heat load.

3.1 Material Selection

When designing supports for cryogenic systems, tensile strength, thermal conductivity, and thermal expansivity must be considered. High strength to conductivity ratios are desired. Materials that have this property are generally plastics however only a few have been tested at cryogenic temperatures. Plastics that have been tested, including Dacron, Nylon (polyamide), Mylar, and glass reinforced plastic G10, all have significantly higher strength to conductivity ratios than stainless steel [37], however, the materials other than the G10 all become brittle at low temperatures. G10 has proven to be one of the better materials.

G10 is a composite material of glass fibres in a polyester resin also known as a glass fibre reinforced epoxy (GFRP). It is strong and light and has low thermal conductivity and good vacuum characteristics. It can also withstand cold cycling to 77 K and lower [41]. The strength of the G10 is dependent on the direction of the fibres. The warp direction is parallel to the straight fibres in the weave and is generally the strongest, the weft or fill direction is parallel to the fibres that are woven around the warp fibres, and the normal direction is perpendicular to the fabric or sheet. Tension in the supports will be in the warp or fill direction. G10-CR is a cryogenic grade of G10, which is somewhat more tightly specified and has easily accessible cryogenic property data. The cryogenic grade is very expensive so G10, which has very similar properties to G10-CR, is used for the apparatus.

In Figure 13, the thermal expansion of G10-CR and Polyamide (nylon) is shown for cryogenic temperatures. This data is from the National Institute of Standards and Technology (NIST) Cryogenic Material Properties Database [42]. The polyamide changes length much more than the G10-CR and therefore may cause alignment and stress problems. Therefore, unless stress due to thermal contraction at low temperatures can be eliminated, nylon is not a good support material.

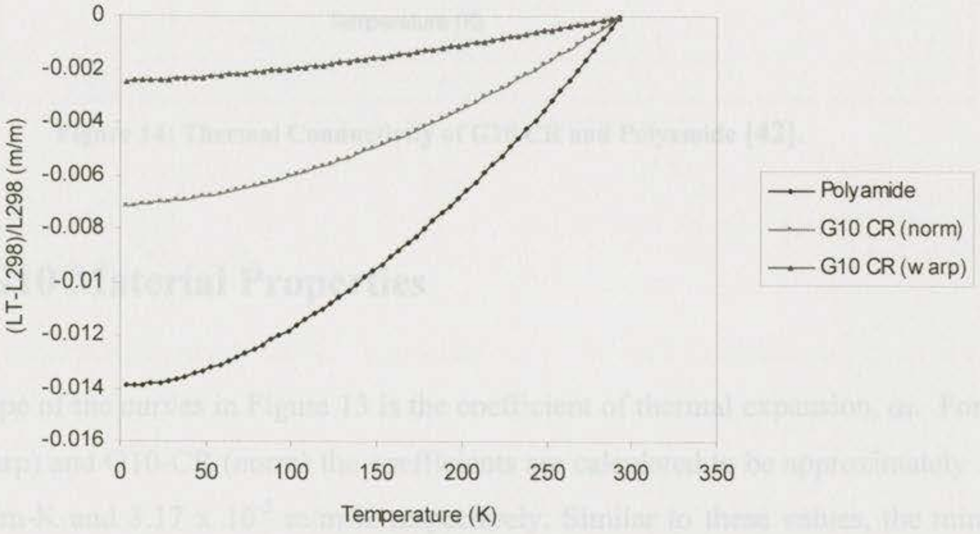

Figure 13: Thermal Expansion of G10 CR and Polyamide [42].

In Figure 14 the thermal conductivity of G10-CR and polyamide is shown. This data is also from the NIST Cryogenic Material Properties Database [42]. The polyamide has a slightly lower thermal conductivity at the high temperature range however the G10-CR value is still very good when compared to materials such as stainless steel. Therefore, since the strength, thermal expansion and thermal conductivity of G10 are all acceptable and since several authors [20,24,25,31] have proven its use, G10 was chosen as the support material for the superconducting magnet.

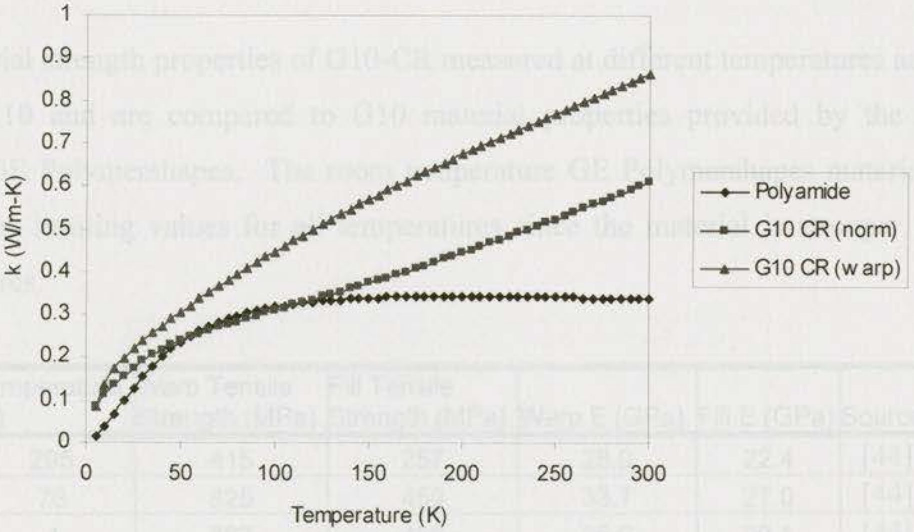

Figure 14: Thermal Conductivity of G10 CR and Polyamide [42].

3.2 G10 Material Properties

The slope of the curves in Figure 13 is the coefficient of thermal expansion, α_l. For G10-CR (warp) and G10-CR (norm) the coefficients are calculated to be approximately 1.02 x 10^{-5} m/m-K and 3.17 x 10^{-5} m/m-K respectively. Similar to these values, the minimum coefficient of thermal expansion given by the material supplier (GE Polymershapes [43]) for G10 is 1.82 x 10^{-5} m/m-K, however the direction was not specified. Kasen *et al*. [44] measured the thermal contraction of G10-CR and found that the warp and fill directions had almost the same values, therefore the value of 1.82 x 10^{-5} m/m-K will be used for both directions.

The average approximate thermal conductivity, k_{ave}, for G10 (non-cryogenic) is calculated from Figure 14 by finding the average value of k between the cold and warm end temperatures of the supports as will be defined later. These values are used in the following heat transfer calculations.

The material strength properties of G10-CR measured at different temperatures are shown in Table 10 and are compared to G10 material properties provided by the material supplier GE Polymershapes. The room temperature GE Polymershapes material values are used as limiting values for all temperatures since the material is stronger at lower temperatures.

Temperature (K)	Warp Tensile Strength (MPa)	Fill Tensile Strength (MPa)	Warp E (GPa)	Fill E (GPa)	Source
295	415	257	28.0	22.4	[44]
76	825	459	33.7	27.0	[44]
4	862	496	35.9	29.1	[44]
295	276	241	18	15	[43]

Table 10: G10 material properties.

3.3 Support Design

G10 is available in sheets, blocks, tubes and rods. To make bracket design as simple as possible, G10 sheet was cut into rectangular rods with round ends and holes at the ends as shown in Figure 15. The ends are then bolted to the support brackets. Both the cross-sectional area and the connecting ends of the G10 must be examined for stress and strength properties.

Figure 15: G10 support design sketch.

3.3.1 Cross Sectional Area

The supports were designed to have the longest lengths possible to reduce heat transfer, and to provide support in both the vertical and horizontal directions as shown in Figure 12. The lengths and angles required for these supports are shown in Table 11 where the Pin Length is the length from G10 bolt hole to bolt hole and the Conduction Length is the length between support bracket ends. The force direction is the direction of force with respect to the G10 fibre direction.

Support	Pin Length (cm)	Conduction Length (cm)	Angle (from horizontal) (deg)	Force Direction
1	37.5	36.2	66.53	warp
2	19.2	18.0	7.59	fill
3	10.5	9.25	55.30	fill
4	23.6	22.3	0.00	fill

Table 11: Design details.

Supports 1 and 3 were designed to support the weight and supports 2 and 4 to prevent horizontal motion. The amount of horizontal force that the magnet will experience is unknown and therefore only the vertical force due to gravity on supports 1 and 3 is analysed. Supports 1 must support a mass of 34.93 kg and supports 3 must support a mass of 76.66 kg. The number of supports that may be used is four for Supports 1, and four or six for supports 2.

The stress for different cross-sectional areas of supports 1 and 2 are shown in Table 12 and Table 13. The total force along the support is calculated for each support using the angles as shown in Table 11.

Number	Mass/Support (kg)	Force (N)	Dimensions (cm)	CS Area (m^2)	Stress (MPa)
4	8.732	93.29	0.64x0.95	6.05E-05	1.54
4	8.732	93.29	0.64x0.64	4.03E-05	2.31
4	8.732	93.29	0.32x0.95	3.02E-05	3.08
4	8.732	93.29	0.32x0.64	2.02E-05	4.63
4	8.732	93.29	0.32x0.32	1.01E-05	9.25

Table 12: Support 1 stress analysis.

Number	Weight/Support (kg)	Force (N)	Dimensions (cm)	CS Area (m^2)	Stress (MPa)
4	19.17	228	0.32x0.95	3.02E-05	7.55
4	19.17	228	0.32x0.64	2.02E-05	11.33
6	12.78	152	0.32x0.64	2.02E-05	7.55
4	19.17	228	0.32x0.32	1.01E-05	22.66
6	12.78	152	0.32x0.32	1.01E-05	15.11

Table 13: Support 3 stress analysis.

The calculated stress for every cross sectional area considered is well below the tensile strength given in Table 10, therefore any cross sectional area could be chosen. The area of 0.32x0.64 cm (0.125x0.25 in) is chosen since it has small cross sectional area for reducing heat transfer and is not too small for machining purposes and six supports are used in the Support 3 position. Drawings of each support are in Appendix-D.

3.3.2 Heat Transfer

Heat transfer for the chosen cross sectional area is calculated using

$$\dot{Q} = k_{ave} A \frac{T_1 - T_2}{L_{cond}} \tag{16}$$

where $\dot{Q}$ is the rate of heat flow, k_{ave} is the average thermal conductivity over the temperature range, A is the area, T_1 and T_2 are boundary temperatures, and L_{cond} is the conduction length of the support. The average conductivity k_{ave}, as explained previously, is calculated from the data for G10-CR warp shown in Figure 14. The results for each support are shown in Table 14. From these calculations, the total support conduction heat transfer to the 40 K stage of the cryocooler is 0.215 W and to the 4.2 K stage is 63.6 mW.

Support	# of supports	Cond Length (m)	CS Area (m^2)	Twarm (K)	Tcold (K)	k_{ave} (W/m-K)	Heat Transfer/support (W)	Total Heat Transfer (W)
1	4	0.3620	2.02E-05	40	4	0.1977	3.96E-04	1.59E-03
2	4	0.1796	2.02E-05	40	4	0.1977	7.99E-04	3.20E-03
3	6	0.0925	2.02E-05	300	40	0.6308	3.58E-02	2.15E-01
4	4	0.2230	2.02E-05	300	4	0.5496	1.47E-02	5.88E-02

Table 14: Supports heat transfer.

3.3.3 Thermal Expansion

Decreasing the temperature of the supports causes the lengths of the supports to contract. The length however is prevented from contracting because the supports are angled in alternating directions counteracting any horizontal motion, and the supports are clamped in friction joints so that the angles, and therefore the height, cannot change. This creates strain and therefore stress in the supports. Strain, ε, is determined using

$$\varepsilon = \frac{L_{293} - L_{ave}}{L_{293}} = \alpha_l \Delta T \,. \tag{17}$$

where L_{293} is the length at a room temperature, L_{ave} is the length at an averaged cold temperature, α_l is the coefficient of thermal expansion, and ΔT is the temperature change. The stress, S, is then calculated using Hooke's law, which assumes elasticity, and is given by

$$S = \varepsilon E \,, \tag{18}$$

where E is the modulus of elasticity given in Table 10 and the direction of the stress is shown in Table 11.

Strain due to thermal contraction was calculated for each support using the G10 coefficient of thermal expansion of 1.82×10^{-5} m/m-K. If the strain is multiplied by the room temperature support length, the change in length can be determined. Since the support ends are not at the same temperature, the average cold temperature of the support, determined by subtracting T_{warm}-T_{cold} and dividing by two, was subtracted from room temperature to determine the temperature change. The results are shown in Table 15.

Support	Pin Length (cm)	T_{ave} (K)	T_{293}-$T_{ave.}$ ΔT (K)	Strain	E (GPa)	Stress (MPa)
1	37.5	18	275	0.0050	18	90.1
2	19.2	18	275	0.0050	15	75.1
3	10.5	127	167	0.0030	15	45.5
4	23.6	145	149	0.0027	15	40.5

Table 15: Calculated strain and stress due to contraction.

The largest stress value of 90.1 MPa is a factor of 3 less than the warp direction tensile stress of 276 MPa from Table 10. This is an acceptable safety factor especially since the Young's Modulus of G10 increases a relativity small amount compared to the increase in tensile strength with decreasing temperature.

3.3.4 Joint Design

3.3.4.1 G10

Tensile, shear, and bearing stresses in the 'eye' of the G10 joint were calculated using classical formulas for pinned joints given by Lewis and Samuel [45]. All calculated values were at least a factor of ten below the acceptable values shown in Table 10. The shear stress in the stainless steel 304 bolt used to connect the joint was also determined to be well below the failure level. However, since the joint is a friction joint, the bolt should not come into bearing on the sides of the holes and therefore the bearing stress in the eye of the G10 and the shear stress on the stainless steel bolt should actually be zero.

3.3.4.2 Brackets

The brackets are 0.32 cm (1/8 in) thick Aluminum 6061-T6 or stainless steel 304. The stainless steel brackets were used only when the brackets needed to be welded to the stainless steel vessel. The drawings of these brackets are shown in Appendix-D. The tensile, shear, and bearing stresses were again calculated and the values were found to be acceptable. The size of the fillet welds required for several of the joints was also calculated and a weld size of 0.32 cm was chosen. Details of the weld calculations are shown in Appendix-B.

4 Magnet Current Lead Design

Current leads are generally the main source of heat into a superconducting magnet system. Classically, metal current leads had to be optimized in cross sectional area and length to minimize ohmic and conductive heat. However, these metal leads still allowed a relatively large amount of heat to conduct to the liquid helium in the classical immersion-cooled superconducting magnets. A method to reduce the amount of heat transfer was first proposed by Mumford in 1988 [48] and involves using a combined system of 300-40 K metallic current leads and 40-4.2 K high temperature superconductor (HTS) current leads. Several authors have modeled and tested HTS leads [49-52]. HTS leads made conduction cooling possible and have been used in most conduction cooled superconducting magnet systems [18,21,22,25,27,28]. The HTS leads are used in this design in combination with metal current leads. A diagram of the leads and their connections is shown in Figure 16. In this combined lead system, the metal current leads from the room temperature connection to the superconducting leads at 40 K are still generally the main source of heat into the system. Therefore, they must be designed so that losses are minimized. The HTS leads also transfer a small amount of heat and there is heat generated at electrical contacts due to contact resistance. All of these heat sources are considered and the total amount of heat transfer from the current leads to the cryocooler is approximated in this chapter.

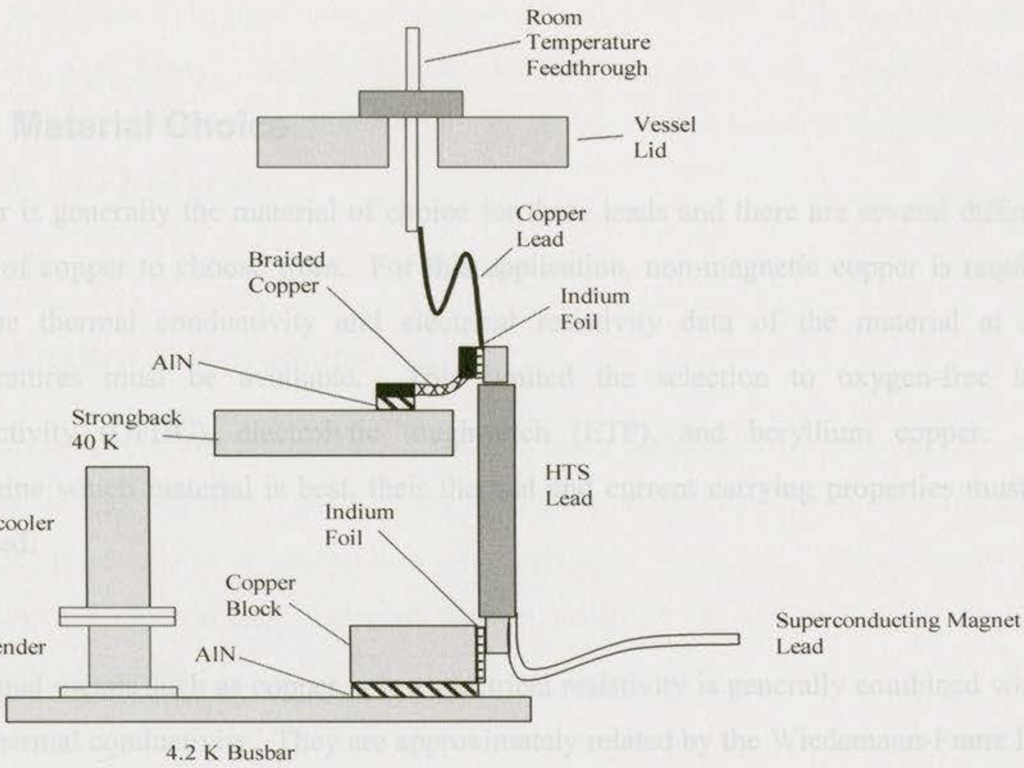

Figure 16: HTS and metal current lead components and connections.

4.1 Metal Current Lead

There are two primary losses that occur in the metal current lead. The first is due to heat transfer from thermal conduction over a temperature gradient and the second is due to heat produced from resistive losses when a current passes through the lead. The length and cross sectional area of the conductor must be optimized to minimize both the conducted heat and the I^2R (resistive) heat, where the conducted heat is inversely proportional to the length/area ratio and the resistive heat is proportional to the length/area ratio. To determine the optimal length and area of the lead, the electrical resistivity and thermal conductivity of the lead material over the operating temperature range must be found.

4.1.1 Material Choice

Copper is generally the material of choice for these leads and there are several different forms of copper to choose from. For this application, non-magnetic copper is required and the thermal conductivity and electrical resistivity data of the material at low temperatures must be available. This limited the selection to oxygen-free high conductivity (OFHC), electrolytic tough-pitch (ETP), and beryllium copper. To determine which material is best, their thermal and current carrying properties must be analysed.

In normal metals such as copper, a low electrical resistivity is generally combined with a high thermal conductivity. They are approximately related by the Wiedemann-Franz Law given by

$$k\rho = L_0 T, \tag{19}$$

where k is the thermal conductivity, ρ is the electrical resistivity, T is the temperature, and L_0 is the Lorenz number. In the ideal case of elastically scattered electrons, $L_0=2.45\text{x}10^{-8}$ $A^2\Omega^2/K^2$. With purer materials, this number is smaller on average and is constant only above a temperature of 150 K. Below 150 K the Lorenz number goes to a minimum then returns to its "constant" value at temperatures around 6 K. Values of the Lorenz number for copper are plotted by Lock [53].

The smaller Lorenz number would, in theory, be the best situation since the material would then conduct less heat and have a higher current capacity, however, if the lead is not optimised properly or if a current slightly higher than the optimised current is desired, pure metals become unstable. This is because they have a higher rate of rise of temperature during overload leading to faster thermal runaway and burnout of the lead [54]. Therefore, it is safer to stay with a material that is not quite as pure. OFHC can then be eliminated from the options. Although Powell [55] found that it has a lower thermal conductivity than ETP copper, newer data published by the NIST [42] shows that OFHC has a very high thermal conductivity and is much more pure than the sample plotted by Powell.[2] Of the other possibilities, ETP copper was chosen, however beryllium copper might also be a good option.

4.1.2 Electrical Resistivity

The resistivity ρ of ETP copper was calculated using Matthiessen's rule $\rho=\rho_R+\rho_I$ where ρ_R is the residual resistivity and ρ_I is the ideal lattice resistivity. The residual resistivity depends on purity and is independent of temperature. The ideal lattice resistivity is temperature dependent and is due to phonon scattering; it is the same for different specimens of a metal.

Residual resistivity can be calculated knowing the residual resistivity ratio (RRR) for the specific material where the RRR is defined as the ratio of the electrical resistivity at 273 K to that at 4 K. As the purity increases so does the RRR value, causing the RRR value to vary by several orders of magnitude from specimen to specimen. For ETP copper, used in this design, the RRR is between 40 and 90 (depending on the supplier). The value of RRR=40 for ETP copper was determined by comparing the thermal conductivity plotted for different RRR values by Jones *et al*. [54] and the thermal conductivity of ETP copper measured by Powell et. al. [55]. The value of 90 was obtained from Maehata et. al. [56].

Ideal lattice resistivity was calculated using the formula

$$\rho_I = 10^{-8} \bullet \exp\left[\sum_{0}^{4} C_i (\ln T)^i\right], \qquad \text{(ohm-m)} \qquad (20)$$

where

C_0=-9.600976

---

[2] OFHC can vary widely in composition depending on the manufacturer.

$C_1=-12.52445$

$C_2=8.309361$

$C_3=-1.583458$

$C_4=0.0993132$

This formula, which was determined by Jones *et al*., deviates from data by no more than two percent [54]. Equation 20 and Matthiessen's rule can be used up to 300 K, after which ρ_l must be assumed to be proportional to T. The results are shown in Figure 17 for ETP copper.

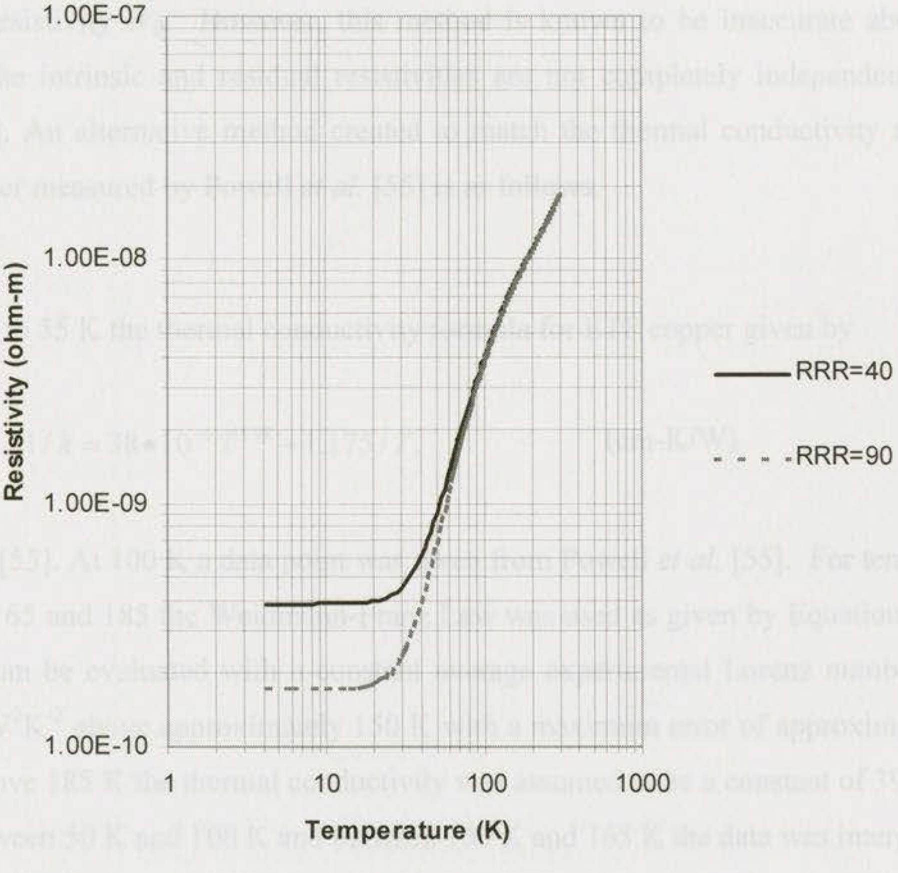

Figure 17. Electrical resistivity of ETP copper with RRR of 40 and 90.

4.1.3 Thermal Conductivity

The total thermal conductivity, k, is approximately the sum of the electronic thermal conductivity, k_e, and the lattice thermal conductivity, k_g. In metals such as copper, with a large number of free electrons, the lattice thermal conductivity can be neglected. This leaves only the electronic thermal conductivity to be calculated.

Jones *et al.* [54] used a method similar to Matthiessen's rule to calculate the electronic thermal conductivity, k_e, by assuming that $1/k_e$ is the sum of an impurity scattering term represented by the intrinsic resistivity W_i, and a phonon scattering term represented by the residual resistivity W_0. However, this method is known to be inaccurate above 10 K because the intrinsic and residual resistivities are not completely independent of each other [55]. An alternative method created to match the thermal conductivity results for ETP copper measured by Powell *et al.* [55] is as follows.

From 4 K to 55 K the thermal conductivity formula for ETP copper given by

$$1/k = 38 \bullet 10^{-6} T^{1.98} + 1.175/T, \qquad \text{(cm-K/W)} \qquad (21)$$

was used [55]. At 100 K a data point was taken from Powell *et al.* [55]. For temperatures between 165 and 185 the Weidmann-Franz Law was used as given by Equation 19. This formula can be evaluated with a constant average experimental Lorenz number [54] of $2.1\mathrm{x}10^{-8}$ V^2K^{-2} above approximately 150 K with a maximum error of approximately 15% [53]. Above 185 K the thermal conductivity was assumed to be a constant of 390 W/m-K [57]. Between 50 K and 100 K and between 100 K and 165 K the data was interpolated.

The results are shown in Figure 18. The experimental data points were taken from Powell *et al.* [55]. Equation 21 fits the experimental values between 15 K and 50 K within 2% [55]. Below 15 K the experimental data is higher than calculated using Equation 21, probably due to an anomalous electrical resistance [55]. Figure 18 also resembles the data given by Jones *et al.* [54] for RRR=39 and Maehata *et al.* [56] for RRR=92.5. Theoretically, the thermal conductivity should be larger for a larger RRR value, however, the relationship between them shown by Jones [54] and Maeheta [56] is not in agreement. It is therefore uncertain whether the ETP copper measured by Powell *et al.* [55] has a RRR value of 40 or 90. Overall, the calculated thermal conductivity compares well with the experimental values for ETP copper.

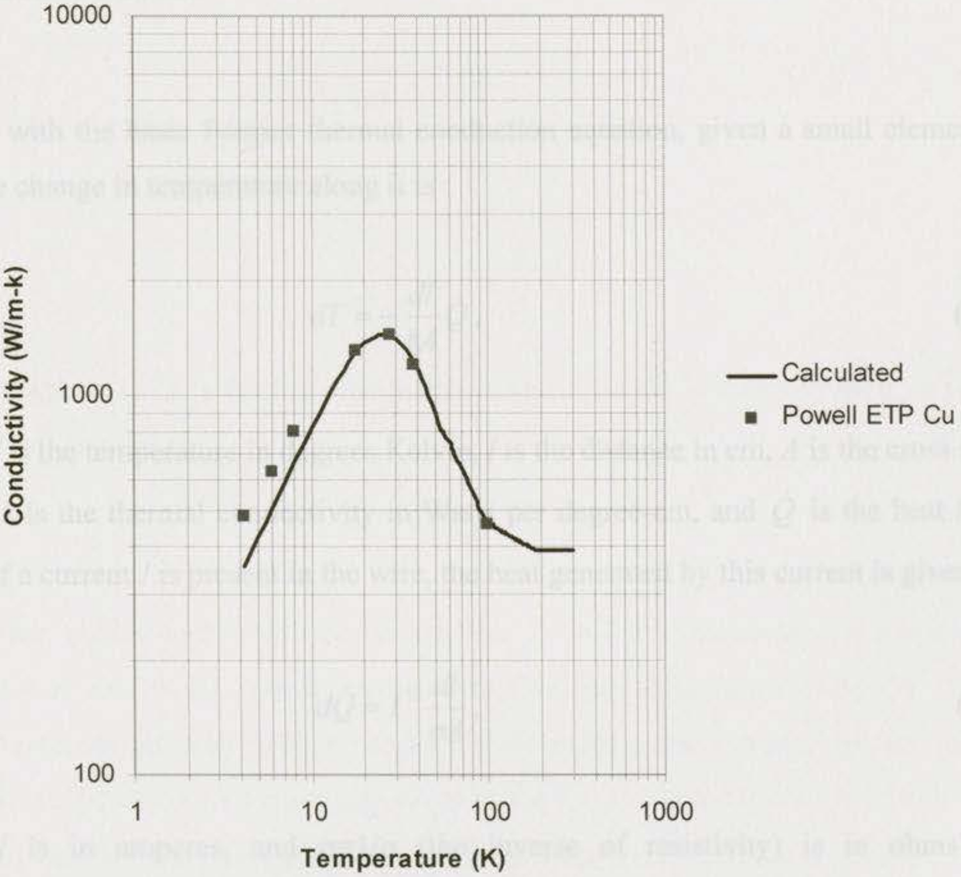

Figure 18. Comparison of calculated thermal conductivity of ETP copper and data taken from plot of ETP thermal conductivity experimental values measured by Powell *et al.* [55].

4.1.4 Optimized Length and Area

Once the electrical resistivity and thermal conductivity are known over the operating temperature, equations for an optimized length and area resulting in the minimum heat conduction and resistive heat generation for a copper lead may be derived. A simple model was determined for conduction cooled copper leads by McFee [58]. His derivation of these equations is summarized in the following paragraphs. For these equations it is assumed that there are no heat losses from the lead other than at its ends and that thermal transients have died out.

Starting with the basic Fourier thermal conduction equation, given a small element of a wire, the change in temperature along it is

$$dT = -\frac{dl}{kA}\dot{Q}\,, \tag{22}$$

where T is the temperature in degrees Kelvin, l is the distance in cm, A is the cross section in cm^2, k is the thermal conductivity in Watts per degree-cm, and $\dot{Q}$ is the heat flow in watts. If a current I is present in the wire, the heat generated by this current is given by

$$d\dot{Q} = I^2\frac{dl}{\sigma A}\,, \tag{23}$$

where I is in amperes, and $\sigma=1/\rho$ (the inverse of resistivity) is in ohms^{-1}-cm^{-1}. Eliminating dl in the two above equations and integrating gives the general equation

$$\dot{Q} = I\left[\frac{2k}{\sigma}(c-T)\right]^{1/2}\,, \tag{24}$$

where c is an integration constant and has the unit of temperature; it represents the highest possible temperature on the wire. When the conductor length is optimized (the heat flowing out is minimized), $c=T_H$. This requires that the plot of temperature versus distance have a slope of zero, and a maximum, at the hot end of the lead. As a result there is no heat entering the hot end by conduction and the electrical current generates all the heat flowing to the cold end.

Using $c=T_H$, McFee [58] then divided the conductor into n segments, each of constant k and σ, with a temperature decrement ΔT given by $(T_H-T_L)/n$. The minimum heat flow $\dot{Q}_n$ through each segment n was then determined using Equation 24 and is given by

$$\dot{Q}_n(T_L) = I\left[2\left(\frac{k}{\sigma}\right)_{AV}(T_H - T_L)\right]^{\frac{1}{2}}, \tag{25}$$

where

$$\left(\frac{k}{\sigma}\right)_{AV} = \frac{1}{n}\left[\frac{k_1}{\sigma_1}+\ldots+\frac{k_n}{\sigma_n}\right]. \tag{26}$$

In these equations, T_H is the high temperature, and T_L is the low temperature. The value of n was determined by

$$n = (T_H - T_L)/2. \tag{27}$$

T_H was then chosen and T_L was decreased from T_H in 2 K increments over a temperature range of 4 K to 290 K. The minimum heat flow was determined using the electrical resistivity values for both RRR=40 and RRR=90 and the results varied by less than 1%. Results from Equation 25 are plotted versus T_L for T_H=290 K in Figure 19. Note that the minimum heat flow is not dependent on the cross sectional area of the conductor.

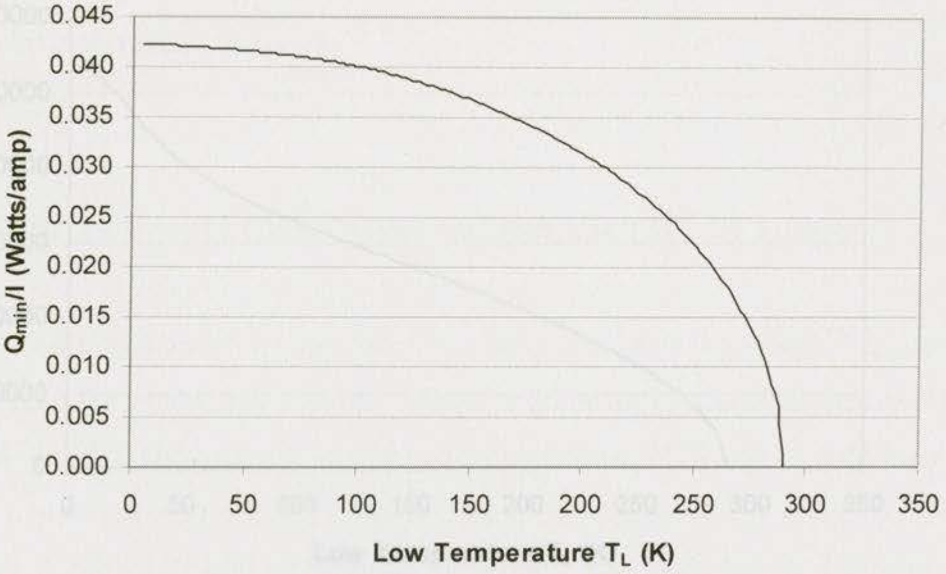

Figure 19. Heat conducted to low-temperature region by an optimized ETP copper lead for T_H=290 K.

Next, the length of the conductor can be obtained using

$$\frac{L_n I}{A} = \frac{1}{I}\left[(\sigma_1 - \sigma_2)\dot{Q}_1 + (\sigma_2 - \sigma_3)\dot{Q}_2 + \ldots + (\sigma_{n-1} - \sigma_n)\dot{Q}_{n-1} + \sigma_n \dot{Q}_n\right] \qquad (28)$$

where L_n is the over-all lead length. L_n approaches L as n approaches infinity however accurate answers are obtained with n equal to 5 or 10 [58]. The results are shown in Figure 20. The lengths per area ratio results were determined for both RRR=40 and 90 and the results varied by less than 1%. Figure 19 and Figure 20 closely resemble the plots obtained by McFee [58] in which the electrical resistivity and thermal conductivity data for OFHC copper were used [59],[60].

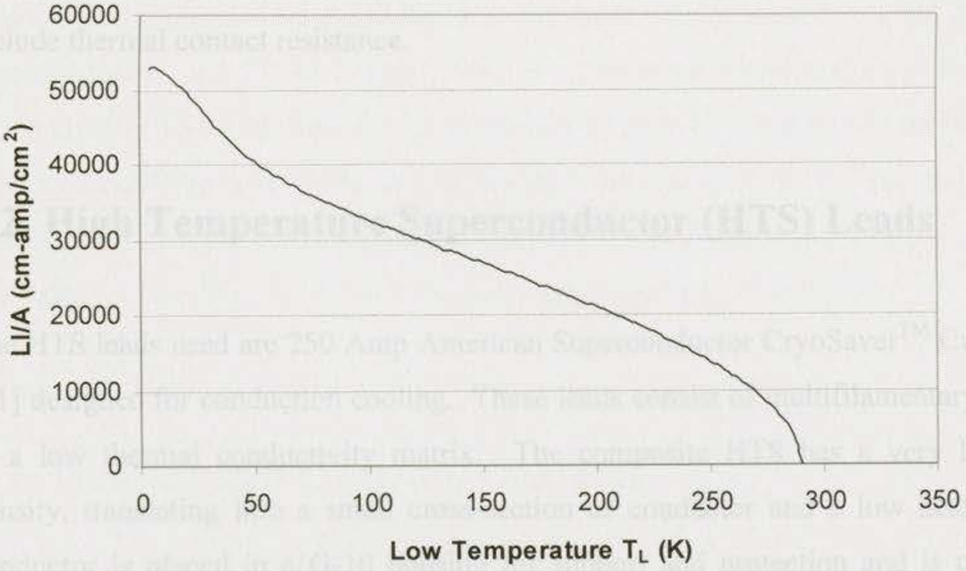

Figure 20. Ratio of length to cross sectional area of an optimized ETP copper lead for Th=290K.

Several data points were taken from Figure 19 and Figure 20 and used to determine the heat transfer and length required for the operating current of the magnet of 158 Amps and a cross section area of 1.27x0.16 cm (0.5x0.0625 in). The results are shown in Table 16. It was assumed that the temperature of the cold end is 40 K and therefore the length of the conductor should be 54.9 cm (21.63 in).

T_L (K)	Q (Watts)	L (cm)
46	6.59	52.8
44	6.59	53.5
42	6.60	54.2
40	6.60	54.9
38	6.61	55.7
36	6.61	56.5
34	6.62	57.3

Table 16: Optimized length L_n for an operating current of 158 Amps, T_H=290 K and cross section area=1.27x0.16 cm.

The heat leak through the metal current leads was also calculated with no current using Equation 22 where the conductivity was averaged over the temperature range. With

T_H=290 K and T_L=40 K the heat leak is 4.36 W for one lead. This calculation does not include thermal contact resistance.

4.2 High Temperature Superconductor (HTS) Leads

The HTS leads used are 250 Amp American Superconductor CryoSaver™ Current Leads [61] designed for conduction cooling. These leads consist of multifilamentary HTS tapes in a low thermal conductivity matrix. The composite HTS has a very high current density, translating into a small cross-section of conductor and a low heat leak. The conductor is placed in a G-10 housing for support and protection and is connected to nickel-plated copper end caps. These leads are also designed to tolerate applied magnetic fields along two axes.

The HTS lead is a perfect electrical conductor and a poor thermal conductor and therefore helps decrease the amount of heat reaching the inefficient 4 K stage of the cryocooler. In addition, a heat sink is used at the 40 K stage to further prevent heat from conducting to the second stage of the cryocooler. This heat sink also keeps temperature at the HTS and metal conductor connection stable when the current and magnetic field are varied [51].

4.2.1 HTS Heat Leak

The current heat leak in the HTS leads from 1st stage to the 2nd stage of the cryocooler is attributed to conduction of heat down the leads and generation of heat at the metal connections. There is no ohmic generation of heat within the HTS leads since there is no resistance in the leads when they are superconducting. Assuming a linear temperature gradient and a constant effective thermal conductivity of the HTS lead, the heat leak by conduction per pair is given by [48]

$$\dot{Q}_{Cond} = \frac{2kA[T_1 - T_2]}{L_{sc}} \qquad (29)$$

where k is the thermal conductivity, A is the cross section area, L_{sc} is the length of the superconductor, and T_1=40 K and T_2=4.2 K. American Superconductor [61] measured the conductive heat leak from 64-4.2 K per pair as 90 mW. This should include the metal to superconducting copper ohmic losses. With an area of 9.73×10^{-5} m^2 and a length of 0.305 m, this gives an effective thermal conductivity of 2.359 W/m-K per conductor. The heat leak per pair from 40-4.2 K is therefore approximately 54 mW.

4.3 Thermal and Electrical Contacts

As mentioned previously, a heat sink is used at the 40 K stage. Flexible braided copper is used to thermally connect the HTS leads to the 1st stage of the cryocooler and a piece of AlN is used to electrically isolate the HTS leads from the strongback and 1st stage (Figure 16).

The HTS leads are thermally connected to the busbar, shown in Figure 16, using blocks of ETP copper with bases of 5.1x4.4 cm (2x1.75 in) and 2.5 cm (1 in) thick. The leads are clamped to the sides of these blocks, which are positioned on either side of the 4.2 K stage of the cryocooler. The blocks are electrically isolated from the busbar using AlN.

Electrical contact between all leads is made by clamping indium foil between the lead ends. Since contact surfaces are never perfectly smooth, contact occurs only at discrete points. This impedes the current since the area that the current can flow through is decreased, therefore a contact resistance is created. To reduce heat generation, this contact resistance must be considered.

4.4 Contact Resistance

Contact resistance between surface contacts is another factor of heat leak into the system. The contact resistance heat generated per pair can be determined from

$$\dot{Q}_{Res} = 2I^2 R_c, \tag{30}$$

where I is the current and R_c is the contact resistance. If the contacts are poor or dirty, the contact resistance increases and more heat is added to the system. It is therefore important to reduce the contact resistance as much as possible. When dealing with metals such as copper, oxidation of the surface is a large source of contact resistance. Applying a nickel or silver coating to the copper helps eliminate the oxidation of the copper and increases the electrical conductivity of the contact [62]. In this apparatus, the HTS lead ends and the room temperature feedthroughs are nickel coated however the copper section of the conductors is not.

If a contact does not have an oxidized surface, the contact resistance can be approximated as [63]

$$R_c = [\rho^2 \eta \pi H / 4F]^{1/2}, \tag{31}$$

where ρ is the resistivity of the material, η is an empirical coefficient of order unity, F is the load applied to the interface, and H is the hardness of the softer material. The contact resistance is not dependent on the nominal contact surface area. This equation shows that inserting indium foil between the contacts also helps decrease contact resistance since its H value is relatively small. For example, Niles *et al.* measured a factor of 5 decrease in contact resistance using indium foil [64].

The contact resistance increases with temperature, however its dependence on temperature is not related to bulk resistivity [64]. Because of this and the complicated nature of contact formation, it is difficult to predict contact resistance to better than an order of magnitude [64]. Results from Niles *et al.* [64] show that from 300-40 K the contact resistance of bolted copper contacts decreases by at least a factor of two, however, if precision is required it is necessary to conduct experiments.

For an approximation of the contact resistance for this system, the contact resistance of bolted copper contacts with nickel coatings of 48 μΩ was taken from Farahat *et al.* [62]. This value was then divided by 5, since indium foil is used between the contacts, and then divided by 2, since the contacts are below 100 K. This leaves a contact resistance of 4.8 μΩ. Using Equation 30 with a current of 158 Amps, this contact resistance results in 0.24 Watts of heat being generated per pair of contacts. The complete current lead consists of three contact points giving a total of 0.72 Watts generated by contact resistance. Note again that this value is approximate and will depend on the contact force applied, cleanliness of the contacts, the individual contact surface properties, and exact temperature of the contacts.

4.5 Total Current Lead Heat Leak

The current lead heat leak to the 1st (40 K) and 2nd (4 K) stages of the cryocooler is summarized in Table 17. With a current of 158 A, the major source of heat to the 1st stage is due to conduction and electrical resistance, demonstrating the importance of finding the optimum length to minimize this value. Electrical contact resistance is the main source of heat conducted to the 2nd stage. The current lead heat leak to the cryocooler stages with no current is also shown in Table 17.

Heat Leak to 40 K Stage, I=158 A	
Copper Lead Heat Leak (1 pair)	13.20 W
Contact Resistance (4 contacts)	0.48 W
Total	**13.68 W**
Heat Leak to 4.2 K Stage, I=158 A	
HTS Lead Heat Leak (1 pair)	0.054 W
Contact Resistance (2 contacts)	0.24 W
Total	**0.294 W**
Heat Leak to 40 K Stage, I=0 A	
Copper Lead Conduction (1 pair)	**9.72 W**
Heat Leak to 4.2 K Stage, I=0 A	
HTS Lead Heat Leak	**0.054 W**

Table 17. Heat leak from current leads to 1st and 2nd cryocooler stages with and without current.

There are several ways to improve this system by decreasing the amount of heat leak. One improvement would be to use HTS leads with variable cross sections since as the temperature of the HTS decreases the cross section area required for a specific current density decreases [51]. This would decrease the amount of heat conducting to the 4.2 K stage, although only by a relatively small amount. Another improvement would involve using a thermal heat pipe containing liquid nitrogen as a method of extracting heat from the metal current leads before the HTS leads, as was tested by Daugherty *et al.* [52]. This heat pipe has a thermal conductance significantly higher than designs that rely on thermal conduction through solids. Also, adding Peltier cooling has been a recent method suggested for reducing T_H in the metal current leads [65],[66].

5 Thermal Shield and Cryogenic Insulation

Beside thermal conduction and Joule heating discussed in the previous chapters, radiation is another major method of heat transfer into the superconducting magnet system. Radiative heat transfer is reduced using a thermal shield of high conductivity material and insulation. The thermal shield consists of a strongback and metal shell that surrounds the magnet. Since the strongback must be suspended from the lid of the vacuum vessel, it must be lightweight, however, it is also required to support the magnet, so it must be strong. To act as a thermal shield it must also be an excellent thermal conductor. The material that satisfies all these properties, is nonmagnetic, and inexpensive, is Aluminum. Aluminum grade 6061-T6 is chosen since this is one of the least expensive grades yet highly versatile with good strength and workability. A thickness of 1.3 cm (0.5 in) is sufficient for creating a good thermal pathway to the cryocooler and for supporting the magnet. The metal shell surrounding the magnet must also be lightweight but does not require strength. Electro-tough pitch (ETP) copper, with its excellent thermal conductivity and low cost compared to higher purity coppers, is a good choice for this shell at a thickness of 0.16 cm (1/16 in).

The thermal shield and magnet must be covered with enough insulation to reduce the radiative heat transfer below the maximum amount of heat that the cryocooler can absorb at the 40 K and 4.2 K stages. For the cryocooler used in this apparatus, these values are 45 Watts and 1.5 Watts respectively. In this system, the insulation must also be effective in a small amount of space. To meet these requirements, the type of insulation must be carefully chosen and the thickness of insulation required must be determined. The total radiative heat entering the system may then be approximated to ensure that the cryocooler can handle the heat load.

The type of insulation is based on economy, convenience, weight, ruggedness, volume, and insulation effectiveness. Insulation effectiveness is related to the effective thermal conductivity k_{eff}, which is a measure of several heat transfer mechanisms over a temperature difference. These heat transfer mechanisms include solid conduction, residual gas conduction, and radiation. Generally, in high vacuum ($<10^{-4}$ Torr), residual gas conduction does not make a significant contribution to the total heat transfer and is therefore neglected [37].

5.1 Room Temperature to 40 K Insulation

5.1.1 Types of Insulation

There are several types of insulations used in cryogenic equipment including:

1. expanded closed-cell foams
2. gas-filled powders and fibrous materials
3. vacuum alone
4. evacuated powders and fibrous materials
5. opacified powder insulations
6. microsphere insulation
7. multilayer insulations (MLI)

Fairly complete descriptions of the various insulations have been given by authors Barron and Flynn, [37], [67]. Of all these insulations, multilayer insulation has the lowest k_{eff} and is relatively simple to install [37]. MLI consists of highly reflecting radiation shields separated by spacers or insulators in high vacuum. The radiation shields attenuate radiation and the spacers decrease solid conduction. High vacuum is required to decrease gas conduction. The main disadvantage of MLI is that it does not perform well when compressed.

There are several different types of MLI to choose from including aluminum foil and fiberglass paper, copper foil and fiberglass, and aluminized mylar crinkled or uncrinkled [37]. To avoid the more complicated and expensive use of spacers, aluminized mylar that is aluminized on one side and crinkled was chosen. The crinkling helps reduce contact area and therefore solid conduction. The brand name for this type of insulation is called NRC-2 and is distributed by Metallized Products, Inc. [68].

5.1.2 Effective Conductivity

Heat transfer through the MLI is mainly by radiation and partly by conduction [69]. To determine the insulation thickness required to decrease this heat transfer the effective thermal conductivity of the NRC-2 MLI must be known. This thermal conductivity and/or the heat transfer was measured by several authors, as shown in Table 18. The effective conductivity values vary widely between experiments and depend on many factors. These factors include compression, layer density, vacuum pressure, perforations, outgassing, penetrations, boundary temperature, and attachment methods. For example, the NRC-2 insulation in the paper by Kumar *et al.* [71] was attached by wrapping the insulation around the test apparatus. This method leads to increased heat transfer since heat can conduct from the warm temperature to the cold temperature along the length of the insulation as will be discussed later.

Description	T-Range (K)	Sample Thickness (cm)	Layer Density (#/cm)	Mean Conductivity (μW/m-K)	Heat flux (μW/cm^2)	Source
Aluminized Mylar one side, not crinkled	300-77	3.5	24	85		[37]
NRC-2 crinkled aluminized Mylar film 0.006mm	300-77		35	42		[67]
NRC-2 type Crinkled aluminized mylar film 6 um	300-77		20	28		[70]
No spacer, crinkled shield aluminized one side only	300-77?		26	29		[37]
Aluminized Polyester film, crinkled	279-77	0.978	20	138	285	[37]
Aluminized Polyester film, crinkled	279-20	0.978	20	104	276	[37]
Crinkled, Single-Aluminized Mylar	278-77	0.526	19	29	110	[41]
Crinkled, Single-Aluminized Mylar	278-77	0.333	30	36	220	[41]
Crinkled, Single-Aluminized Mylar	278-77	0.250	40	68	550	[41]
NRC-2 crinkled aluminized Mylar film 0.006mm	300-77	1.176	17	185	350	[71]
NRC-2 crinkled aluminized Mylar film 0.006mm	300-77	1.176	17	185	350	[71]

Table 18: Comparison of effective conductivity for NRC-2 and similar MLI insulations.

5.1.2.1 Compression

In this system, compression can be caused by the weight of the upper layers on the lower layers, tension in wrapping the insulation around a cylindrical object, and thermal expansion and contraction of the insulation components with respect to the object. These sources of compression should be small, however, even small amounts of compression can significantly increase the heat flux through the insulation [37].

5.1.2.2 Layer Density

The layer density greatly affects the thermal conductivity. The results summarized in Table 18 from Weisend II [41] demonstrate that as the layer density increases from 19 layers/cm, the solid conductivity increases more than the radiative heat decreases resulting in increasing thermal conductivity. The thermal conductivity also increases if there are too few layers. For example, Kumar *et al.* [71] show that the heat flux increases greatly if less than 10 layers, at a density of 17 layers/cm, of NRC-2 crinkled insulation are used. Therefore, there must be an optimum layer density resulting in a minimum thermal conductivity. However, a published paper giving the optimum layer density of NRC-2 crinkled single side aluminized mylar was not found and the calculation is difficult due to the crinkled contact surface. From the papers mentioned above, it appears that a layer density of 15-20 layers/cm will be appropriate.

5.1.2.3 Vacuum Pressure

The chamber pressure is $1x10^{-6}$ Torr and is considered high vacuum. This is well within the desired operating pressure of MLI insulation [37].

5.1.2.4 Perforations

The gas between the layers of insulation must be evacuated so that the system can reach the desired vacuum pressure. Some of the gas may escape along the edges of the insulation however perforations in the shields can increase the rate of outgassing. These holes can also increase heat flux however for the crinkled NRC-2 MLI used in this apparatus, a small amount of holes have little effect [37]. For example, if 3-4 percent of the area of the NRC-2 is perforated with 0.32 cm (1/8 in) diameter holes, the heat flux will change very little but outgassing will increase [37].

5.1.2.5 Penetrations

Insulation penetrations for the supports, electrical leads and cryocooler are required for this system. These penetrations must be treated carefully since if the edges of the insulation are in contact with the penetration, more heat will be conducted to the inner (cold) layers of insulation. The MLI insulation conducts heat laterally very well and the insulation layer will therefore become much less effective. To avoid this, the penetration should be separated from the MLI with a buffer material of non-conducting foam or glass wool. Since the foam is difficult to shape and the glass wool is expensive, another possibility may be to use polypropylene or nylon rope. Seams must also be treated carefully. The MLI should be matched layer to layer or a buffer material should again be used [37]. Calculation of the amount of heat leak from penetrations and seams is difficult and will not be attempted in this report.

5.1.2.6 Boundary Temperature

Changes in the cold boundary temperature have little effect on the heat transfer through the insulation, however changes to the warm boundary temperature are more significant. The effective thermal conductivity is approximately proportional to the third power of the warm boundary temperature [37]. For example, this means that k_{eff} for a warm boundary temperature of 279 K, as shown in Table 18, will increase by a factor of 1.4 when the warm boundary temperature is changed to 312 K.

5.1.2.7 Attachment Methods

The insulation used in this apparatus is stitched together using thread. Buttons were used to help hold the layers together and dental floss is used to hang the blankets on the apparatus. This attachment method degrades the performance of the insulation however the amount of degradation is not easily calculated [37].

5.1.2.8 Estimated Effective Thermal Conductivity

To try and account for the increase in k_{eff} due to the previously described factors, the lowest mean thermal conductivity given by Scurlock *et al.* [70] of 28 μW/m-K was multiplied by a factor of three to give 84 μW/m-K and this value is used in the following heat transfer calculations.

5.1.3 Heat Transfer Equations

Linear heat flow by conduction is given by

$$\dot{Q} = k_{eff} A \frac{T_1 - T_2}{L} \tag{32}$$

where $\dot{Q}$ is the rate of heat flow, k_{eff} is the effective thermal conductivity, A is the area, T_1 and T_2 are boundary temperatures, and L is the thickness of the insulation.

For a hollow cylinder, whose inner and outer surfaces are at different temperatures, the conductive heat transfer rate is found from Fourier's Law and is given by

$$\dot{Q}_{cond} = \frac{2\pi L k_{eff}(T_1 - T_2)}{\ln(r_2 / r_1)} \tag{33}$$

where L is the length of the cylinder, and r_1 and r_2 are the radii of the inner and outer cylinder surfaces.

The net exchange of radiant energy between two surfaces is given by

$$\dot{Q}_{rad} = \sigma e A(T_2^4 - T_1^4) \tag{34}$$

where e is a factor involving the emissivities[3] of the two surfaces, σ is a constant equal to 5.67x10-12 W/cm^2-K^4 and A is an area factor. For cylinders, A is the area of the enclosed surface; for parallel plates, A is the area of either surface.

To determine the emissivity of two concentric cylinders, the mode of reflection must be known and in most cases can be assumed to be diffuse rather than specular. The emissivity is then given by

---

[3] Emissivity is the ratio of emission of radiant energy by an opaque material to the emission of a perfect emitter (a blackbody) at the same temperature.

$$e = \frac{e_1 e_2}{e_2 + \frac{A_1}{A_2}(1 - e_2)e_1} \tag{35}$$

where A_1 is the inner surface area, A_2 is the outer surface area and e_1 and e_2 are the emissivities of the inner and outer surfaces respectively. The assumption of diffuse reflectivity may not be valid for the good reflecting surfaces and long wavelength involved in cryogenic applications but it is a good approximation[37].

To minimize the radiant heat flux, materials with low emissivities are desired. Generally, the best electrical conductors have the lowest emissivities, except for superconductors. Factors such as surface contamination, alloying, and work hardening of the surface all increase the emissivity of a material with low emissivity. It should also be noted that visual appearance is not a reliable criterion of reflecting power at long wavelengths. [37]

Description	Emissivity	Temp (K)	Source
304 SS, mechanical polish	0.16	300	[67]
Al coating (79nm thick) on both sides of Mylar film	0.025	307	[33]
Al vaporized on 12.7 um Mylar (both sides)	0.04	300-77	[37]
Al, Polished (2024-T6) 33μin roughness	0.018	4.2	[37]
Al, Polished (2024-T6) 33μin roughness	0.023	77	[37]
Al	0.011	4.2	[72]
Al	0.03	77	[72]

Table 19: Emissivity values of select materials used in the vacuum vessel.

5.1.4 Radiative Heat Transfer Calculation

The room temperature to 40 K surfaces to be insulated are shown in Figure 21, where the strongback and copper shielding are attached to the 40 K stage of the cryocooler. The stainless steel vessel is at room temperature (290 K) everywhere except the inner cylinder that surrounds the furnace that is at approximately 312 K. Because of this elevated temperature and small space, the most difficult area of the magnet to insulate is between the inner cylinder of the vacuum vessel and the magnet as shown in Figure 22. For this space, the radius of the copper shield must be adjusted so that insulation is sufficiently thick to reduce the heat transfer between the 312-40 K to an acceptable level. There must also be enough space left to insulate the 40 to 4.2 K surfaces.

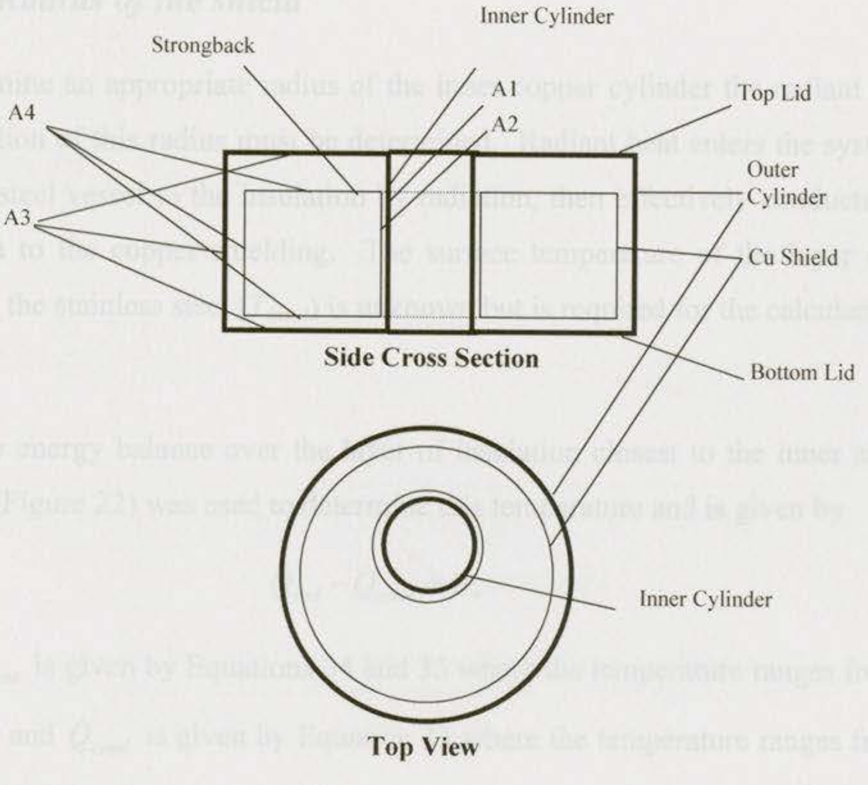

Figure 21: Side cross section and top view of copper shield and outer vacuum vessel with areas used for heat transfer calculations.

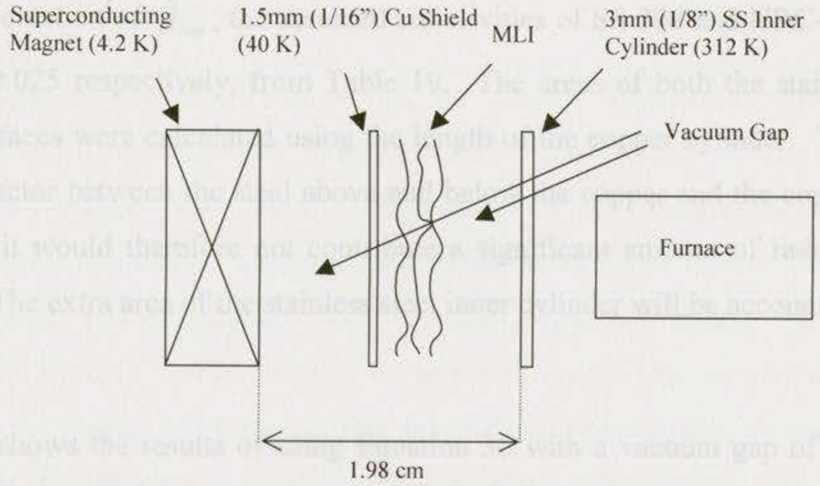

Figure 22: Cross section of space between the superconducting magnet and the inner stainless steel cylinder. (Not to scale)

5.1.4.1 Radius of the shield

To determine an appropriate radius of the inner copper cylinder the radiant heat transfer as a function of this radius must be determined. Radiant heat enters the system from the stainless steel vessel to the insulation by radiation, then effectively conducts through the insulation to the copper shielding. The surface temperature of the layer of insulation closest to the stainless steel (T_{insul}) is unknown but is required for the calculations.

A surface energy balance over the layer of insulation closest to the inner stainless steel cylinder (Figure 22) was used to determine this temperature and is given by

$$\dot{Q}_{rad} - \dot{Q}_{cond} = 0, \tag{36}$$

where $\dot{Q}_{rad}$ is given by Equations 34 and 35 where the temperature ranges from T=312 K and T_{insul}, and $\dot{Q}_{cond}$ is given by Equation 33 where the temperature ranges from the T_{insul} to 40 K. Once the T_{insul} is found, it can be substituted back into one of the heat equations and solved for the total radiant heat transfer.

For the calculation of $\dot{Q}_{rad}$, the assumed emissivities of SS 304 and NRC-2 shielding are 0.16 and 0.025 respectively, from Table 19. The areas of both the stainless steel and copper surfaces were calculated using the length of the copper cylinder. This is because the view factor between the steel above and below the copper and the copper cylinder is small and it would therefore not contribute a significant amount of radiant heat to the cylinder. The extra area of the stainless steel inner cylinder will be accounted for later on.

Figure 23 shows the results of using Equation 36 with a vacuum gap of 2 mm. These results demonstrate that an insulation thickness of 8-10 mm results in an acceptable reduction of radiant heat transfer. Since the inner stainless steel cylinder has an outer radius of 17.1 cm, the inner radius of the copper shield was chosen to be 18.1 cm (7.125 in).

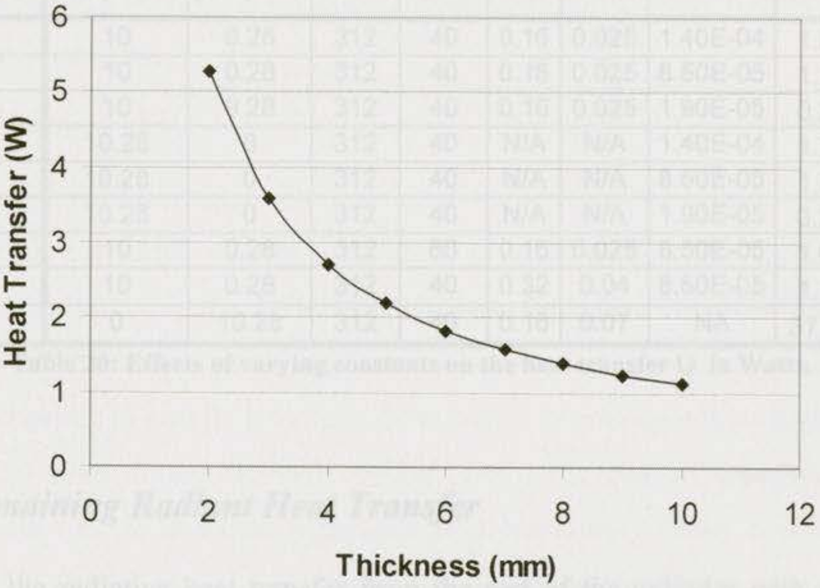

Figure 23: Heat transfer versus insulation thickness for 312 K to 40 K inner cylinder surfaces of the vacuum vessel. Vacuum gap spacing is 2 mm, k_{eff}=84 μW/m-K.

5.1.4.2 Inner Cylinder Heat Transfer

The effects on the heat transfer of varying the effective conductivity, emissivity (e), and lower boundary temperature (T2) in Equations 33,34, and 35 with a inner copper cylinder radius of 18.1 cm are shown Table 20. Case 8 shows that changing the emissivity of the stainless steel (e_1) and NRC-2 (e_2) has little effect on the radiated heat. Case 7 shows that a lower boundary temperature of 60 K also does not change the radiated heat significantly. Cases 4 to 6 in Table 20 demonstrate that the heat transfer when there is no vacuum gap is slightly lower than with a vacuum gap. And finally, for comparison, Case 9 shows the amount of heat transferred if insulation was not used. It is apparent from these results that the insulation makes a significant reduction in heat transfer.

Case	Insulation Thickness (mm)	Vacuum Gap (mm)	T1 (K)	T2 (K)	e_1	e_2	k_{eff} (W/m-K)	Q (W)
1	10	0.28	312	40	0.16	0.025	1.40E-04	1.82
2	10	0.28	312	40	0.16	0.025	8.50E-05	1.11
3	10	0.28	312	40	0.16	0.025	1.90E-05	0.25
4	10.28	0	312	40	N/A	N/A	1.40E-04	1.79
5	10.28	0	312	40	N/A	N/A	8.50E-05	1.09
6	10.28	0	312	40	N/A	N/A	1.90E-05	0.24
7	10	0.28	312	60	0.16	0.025	8.50E-05	1.03
8	10	0.28	312	40	0.32	0.04	8.50E-05	1.11
9	0	10.28	312	40	0.16	0.07	NA	37.90

Table 20: Effects of varying constants on the heat transfer Q in Watts.

5.1.4.3 Remaining Radiant Heat Transfer

To calculate the radiative heat transfer from the rest of the cylinder with an insulation thickness of 10 mm, Equations 16, 33, 34, and 35 may again be used. Equation 35 is a good approximation for short vessels with flat ends where the inner area is A4 and the outer area is A3 as shown in Figure 21. A3 includes the length of stainless steel inner cylinder that was not included in the previous calculations. Again the temperature of the surface of the NRC-2 insulation must be determined using the surface energy balance Equation 36 where $\dot{Q}_{cond}$ is the sum of the cylindrical and linear conduction components.

The resulting heat transfer is calculated to be 2.73 W. Adding this to the total from Case 2 in Table 20 gives a total of 3.84 W of radiant heat that must be absorbed by the 40 K stage of the cryocooler.

5.2 40 K to 4.2 K Insulation

NRC-2 insulation may also be an effective insulation in the 40-4.2 K temperature range. Table 21 shows a comparison of heat flux from 77-4.2 K for different insulations. In the temperature range of 77-4.2 K, a NRC-2 layer density of approximately 6 layers/cm seems to be best [72]. For a temperature ranges of 25-4.2 K and 50-4.2 K, Spradley [73] predicts that a double aluminized Mylar (DAM) layer density of 1.2 layers/cm and 3 layers/cm respectively results in the minimum heat transfer. This means that for 40-4.2 K, 2-3 layers/cm may be optimal if NRC-2 insulation is used. Also, at least a 1 cm gap is needed for the insulation.

For the space between the copper inner cylinder and the inner bore of the magnet, only a 8.02 mm gap is left which may be a bit small to apply NRC-2 effectively. However, Leung [72], Spradley [73], and Zeller [74] all show that using 3M #425 Aluminum tape can be more effective than multilayer insulation, requires less space, and is also less expensive and easier to install. It has also been shown to not degrade on a time scale of at least ten years even during thermal cycling [74]. The 3M Al tape heat transfer is comparable and can be less than optimized MLI insulation. Since it is also easier to install around penetrations and inexpensive it is a good choice to try. Another brand of tape, Eccoshield Al Tape, is also compared in Table 21. It also has an acceptable heat flux value however it is more expensive than the 3M Al tape.

Description	Temp (K)	Heat flux (μW/cm^2)	Source
30 Layers of NRC-2 in a 50.8 mm gap	77-4	1.26	[72]
Bare tank with DAM on both 4 and 77 K surfaces	77-4	2.2	[73]
9 layers of DAM radiation shields with three silk net spacers between	77-4	0.8	[73]
9 Layers of NRC-2 in a 50.8 mm gap	77-4	1.35	[72]
3M #425 Al tape	77.4-4.2	1.24	[72]
Eccoshield Al Tape	77.4-4.2	1.51	[72]
3M #425 Al tape	77-4	1.5	[74]

Table 21: Comparison of heat transfer from 77-4.2 K with different insulations.

3M #425 Aluminum tape was only available in large quantities so Compac 5mil Al tape was tried instead [75]. This tape has all the same properties as the 3M #425 Aluminum tape however the emissivity value may be different since it is a strong function of chemical purity and surface roughness, contamination, and method of preparation [72]. For an approximation, it is assumed that the heat flux of the Compac tape is also 1.5μW/cm^2 although it may be lower since the high temperature is 40 K not 77 K. Using the surface area of the copper shielding, the radiative heat transfer to the magnet is 27 mW.

5.3 Radiative Heat Transfer Summary

The total approximate radiative heat transfer to the 40 K and 4.2 K cryocooler stages is shown in Table 22. Both values are acceptable loads for the respective cryocooler stages.

Temperature Range (K)	Heat Transfer (W)
300-40 K	3.84
40-4.2 K	0.027

Table 22: Approximate Radiative Heat Transfer

6 Total Heat Transfer and Magnet Temperature

6.1 Total Heat Transfer

In summary, the sources of heat to the cryocooler that have been approximated in previous sections include conduction along the supports, conduction and joule heating in the current leads, and radiative heat transfer through the insulation. Other sources of heat include the persistent switch heater, instrumentation wire, and Joule heating within the magnet winding due to eddy currents during charging. The persistent switch heat source comes into effect when the magnet is in charging mode since in this mode, heat must be added to the persistent switch to maintain it in a normal state. The persistent switch has a heater current of 45 mA and a nominal resistance of 78 Ohms, therefore, it creates an additional 158 mW of heat that must be added to the 4.2 K stage. Heat transferred along the instrumentation wire is neglected since the wire is long and narrow, making the heat transfer small in comparison to other heat sources. The eddy current heating is assumed to be low since the magnet is charged at a low rate to avoid quenching and therefore it is neglected. The total approximated heat load on the 4.2 K stage and 40 K stage of the cryocooler in the persistent and charging modes is given in Table 23.

Source	Persistent Q (W)	Charging Q (W)
40 K Stage		
Supports	0.22	0.22
Current Leads	9.72	13.68
Radiative	3.84	3.84
Total	**13.78**	**17.74**
4.2 K Stage		
Supports	0.064	0.064
Current Leads	0.054	0.294
Radiative	0.027	0.027
Persistant Switch	0.000	0.158
Total	**0.145**	**0.543**

Table 23: Total heat load to the cryocooler.

Using these values of thermal load, the operating temperature of the cryocooler can be determined from the RDK-415 Load Map provided by the Janis Research Company [33]. These temperatures are shown in Table 24. To determine the temperature of the magnet the thermal resistance along the conduction path from the cryocooler to the magnet must be analyzed.

Mode	1st Stage Q(W)	Temperature (K)	2nd Stage Q(W)	Temperature (K)
Persistent	13.78	25	0.145	3
Charging	17.74	27	0.543	3.5

Table 24: 1st and 2nd RDK-415 cryocooler temperatures resulting from the persistent and charging heat loads in the superconducting magnet vessel.

6.2 Thermal Contacts

To keep the superconducting magnet coil at 4.2 K or below, the temperature difference between the cryocooler and the magnet must be minimized. To do this the conduction path must be made of high conductivity material, the conduction path must be short, the number of connections must be minimized, and the thermal contact resistance must be reduced. Two flexible braided tin plated ETP copper connectors were designed to attach from the cryocooler to the top and bottom of the magnet. These connectors were fabricated by Assemblage Paro Inc. [77]. The temperature difference created by conduction path from the cryocooler to the magnet, shown in Figure 24, will be approximated to ensure that the magnet will operate below 4.2 K. Note that the magnet top and bottom are aluminum and the rest of the connections are copper.

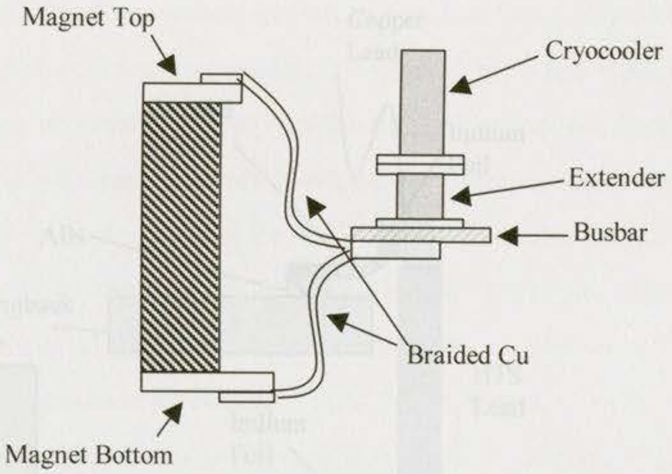

Figure 24: Thermal conduction path from the cryocooler to the top and bottom of the superconducting magnet.

Changes in temperature are also calculated for the path from the current leads to the cryocooler, shown in Figure 25, since these leads must remain in a high temperature superconducting state. In addition, the thermal links from the strongback to the current leads are important since they prevent much of the heat from traveling down to the 4.2 K stage. Since the current leads were assumed to have a high temperature end at 40 K and the cryocooler operates at 27 K then the temperature difference between the strongback and the current leads should be less than 15 K. This will guarantee that the calculated heat flux to the 4.2 K stage will not have been under-approximated.

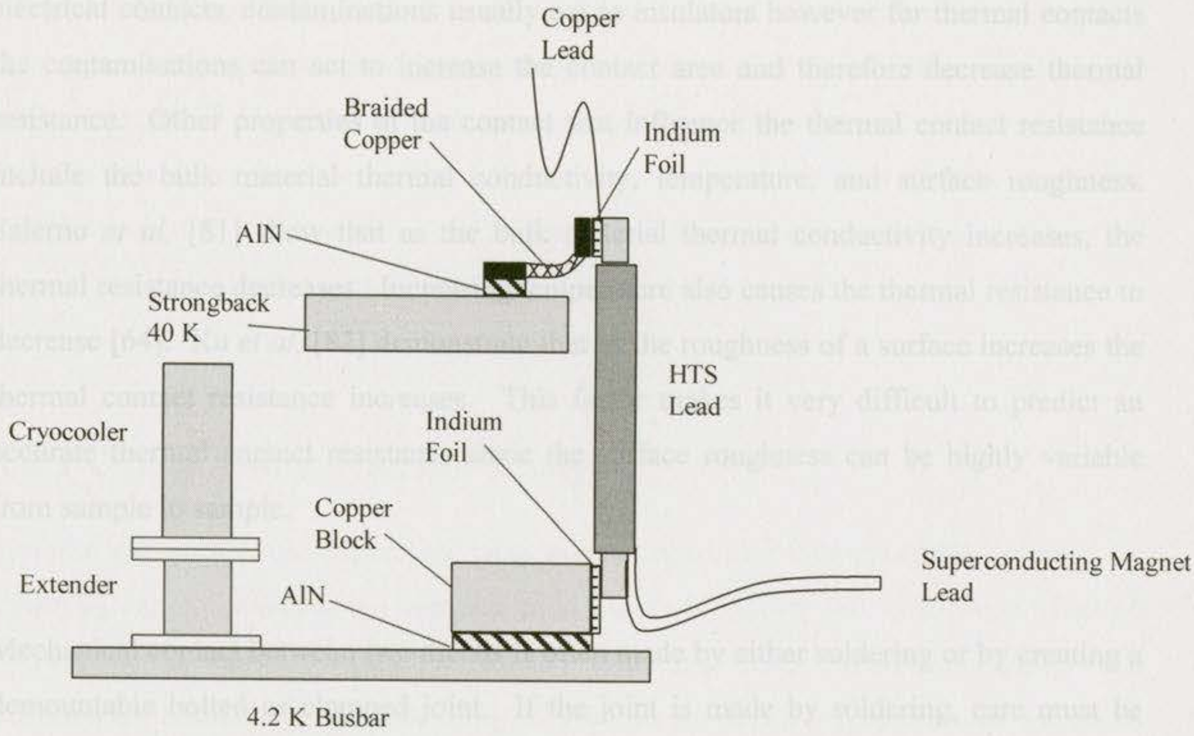

Figure 25: Thermal conduction path from the cryocooler to the HTS leads.

6.2.1 Contact Theory

Thermal contact resistance is dependent on the true contact area of the interface. On all solid surfaces, the true contact occurs at discrete spots produced by the mechanical contact of asperities on the two surfaces. Thus the true contact area is smaller than the cross-sectional area of the contact. Under plastic deformation of the asperities, the true contact area is dependent on the force applied to the interface and is independent of the cross-sectional area of the contact [63], [78], [79]. Therefore, the thermal contact resistance is also dependent on force applied and independent of the cross-sectional area of the contacts. This relationship is approximately linear for wide range of forces, so long as plastic deformation occurs (> 9 N) [80].

The theory of thermal contact resistance stated above is similar to electrical contact resistance theory. The fundamental difference is in the effect of contamination. For electrical contacts, contaminations usually act as insulators however for thermal contacts the contaminations can act to increase the contact area and therefore decrease thermal resistance. Other properties of the contact that influence the thermal contact resistance include the bulk material thermal conductivity, temperature, and surface roughness. Salerno *et al.* [81] show that as the bulk material thermal conductivity increases, the thermal resistance decreases. Increasing temperature also causes the thermal resistance to decrease [64]. Xu *et al.* [82] demonstrate that as the roughness of a surface increases the thermal contact resistance increases. This factor makes it very difficult to predict an accurate thermal contact resistance since the surface roughness can be highly variable from sample to sample.

Mechanical contact between two metals is often made by either soldering or by creating a demountable bolted or clamped joint. If the joint is made by soldering, care must be taken in choosing a solder since most solders become superconducting at low temperature and will therefore increase the thermal contact resistance [83]. However, when this solder is placed in a magnetic field this superconducting state may be suppressed [83]. Another problem with solder is that it can be a relatively poor thermal conductor compared to copper which can again lead to increased thermal contact resistance [84]. According to Willekers *et al.*, the heat resistance of a copper to copper contact is minimized when an indium solder is used, but this value is only slightly better than when clean, smooth surfaces are clamped together with brass bolts [85].

If a demountable joint is required, as is the case with this project, adding interstitial materials that are soft and have a high thermal conductivity can decrease thermal contact resistance of solid materials. Two materials that create dramatic improvement for copper and aluminum joints and are commonly used at temperatures of 4 K are Apiezon N-grease and indium foil [81]. These materials decrease the thermal resistance as a result of increasing the actual contact area by conforming to the contact surfaces. At 4.2 K, the indium foil remains soft and therefore reduces the thermal contact resistance even with lower contact pressures, unlike gold which is much harder [81]. As temperature increases above 30 K, the contact resistance of a copper contact augmented with indium foil becomes much smaller than the bulk resistance of the copper and is difficult to measure [64]. Apiezon^{TM} N-grease reduces thermal resistance between copper and aluminum contacts even more than the indium foil does, however, good contact must be ensured at room temperature so that as the Apiezon grease solidifies at cold temperatures it does not separate from the contact surface causing the thermal resistance to increase.

6.2.2 Contact Heat Transfer Analysis

Thermal contacts in the superconducting magnet apparatus will generally be made by clamping copper or aluminum contacts with a layer of indium foil in-between. Indium will be used instead of Apiezon N-grease in most cases since it is easier to apply. The effect on the contact resistance of using AlN foil as an electrical insulator was not found in any previous literature. Instead, the foil is assumed to have the same effect as the indium foil since the AlN will be sandwiched between two layers of indium foil in the contact.

Since the thermal contact resistance is independent of the cross-sectional area of the contacts, the heat flow, $\dot{Q}$, through the contact is given by

$$\dot{Q} = k_t \Delta T , \tag{37}$$

where thermal conductance k_t is the inverse of the thermal contact resistance and is in units of W/K and ΔT is the temperature change across the contact. Therefore, like the thermal contact resistance, this heat flow is dependent on the force applied to the contacts.

The thermal conductance versus force of aluminum and copper joints, measured by Salerno *et al.* [81] at a temperature of 4 K, is shown in Figure 26. Linear fits were created using Microsoft Excel. These fits were then utilized to determine the thermal contact conductance for the higher clamping forces applied to the 4.2 K joints of this project as shown in Table 26. The temperature difference caused by thermal contact conductance was then evaluated using Equation 37.

Many heat transfer text books including *Fundamentals of Heat and Mass Transfer* by Incropera and DeWitt [86] and *Heat Transfer* by Holman [87] give values of thermal contact resistance per unit area and relate these values to the contact pressure. These texts then show that the heat flow through the contact is dependent on area. This may be applicable to general applications however it does not appear to be correct unless the true contact area is known. Also, because the approximate linear relationship between resistance per unit area versus pressure has a non-zero intercept [88], this data cannot be converted to thermal resistance versus force data without knowing the area that was measured in the original experiment. Thus there are some contraditory published results and care must be taken when analyzing contact heat transfer.

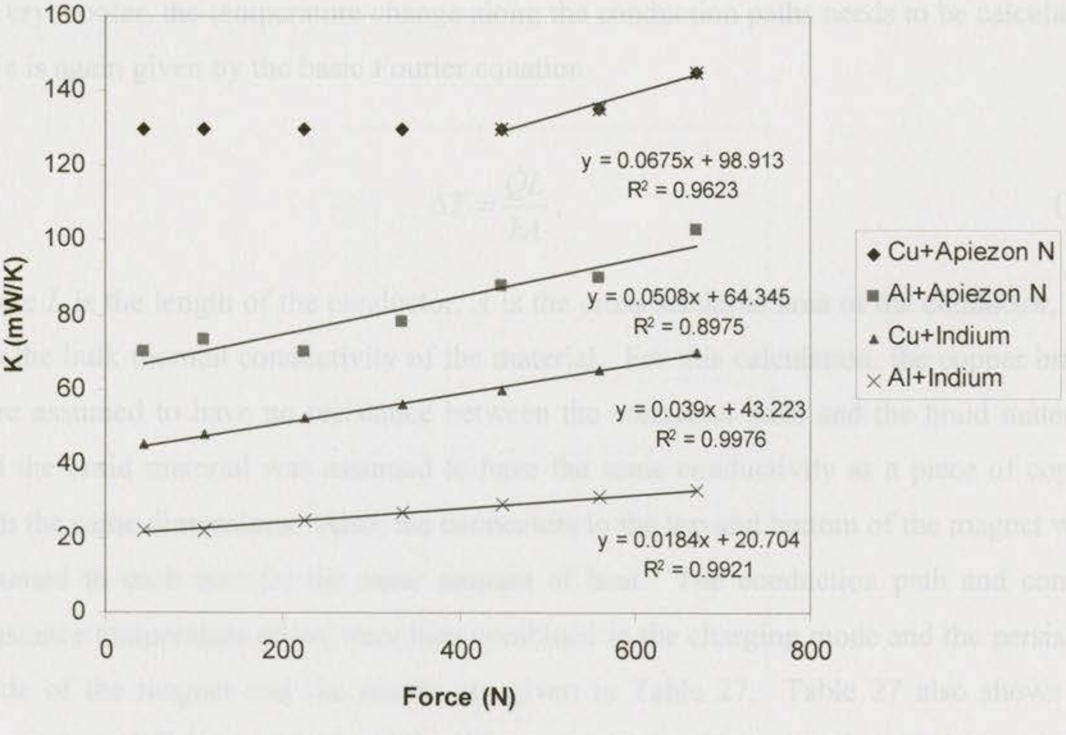

Figure 26: Thermal conductance of pressed Copper (Cu) and Aluminum (Al) joints with Apiezon N-grease and Indium foil. Data is from Salerno *et al.* [81].

Bolt Size	Clamp Load (lb)	Clamp Load (N)
10-24	725	3225
1/4-20	1350	6005

Table 25: 18-8 Stainless Steel Clamp Loads, from Circle Bolt and Nut Co., Inc. [89].

Contact	Size of Bolts	Number of Bolts	Total Clamp Load (N)	K (mW/K)
Al Clamps on Magnet	1/4-20	2	1.20E+04	242
BusbarMagClamp	1/4-20	4	2.40E+04	980
CurrentClamps	10-24	2	6.45E+03	295
CuBlock to Busbar	1/4-20	1	6.01E+03	277
Cryocooler Connection to Busbar	5mm	6	1.93E+04	798

Table 26: Approximate conductance between contacts with indium foil.

To determine the total temperature difference between the superconducting magnet and the cryocooler, the temperature change along the conduction paths needs to be calculated. This is again given by the basic Fourier equation

$$\Delta T = \frac{\dot{Q}L}{kA}, \tag{38}$$

where L is the length of the conductor, A is the cross sectional area of the conductor, and k is the bulk thermal conductivity of the material. For this calculation, the copper braids were assumed to have no resistance between the connector ends and the braid material, and the braid material was assumed to have the same conductivity as a piece of copper with the same dimensions. Also, the connectors to the top and bottom of the magnet were assumed to each transfer the same amount of heat. The conduction path and contact resistance temperature drops were then combined in the charging mode and the persistent mode of the magnet and the results are given in Table 27. Table 27 also shows the temperature difference calculated for the current leads. Note that these values are only approximations since the exact surface properties of each contact are highly variable and the load on the contacts was not measured. A breakdown of the temperature differences created by each path and contact is given in the Appendix-C.

The results in Table 27 show a temperature difference of approximately 2.5 K between the second stage of the cryocooler and the magnet in the charging mode. This is a bit high since if the cryocooler second stage is operating at 3.5 K, the magnet will be at 6 K and therefore will not be able to operate at maximum current. It may therefore be better to use Apiezon grease between the cryocooler and the extender and busbar and to use a thicker flexible copper connectors between the busbar and the magnet. This will be confirmed once the temperature differences are measured experimentally. The persistent mode results are acceptable.

The temperature difference between the high temperature superconducting leads and the second stage of the cryocooler is also approximately 2.5 K in the charging mode. Again, using Apiezon grease between the cryocooler and the extender and busbar will reduce this value however this temperature difference does not significantly affect the operation of the leads and so is not of great concern.

Path	Temperature Difference (K)
Charging Mode	
MagnetTop and Cryocooler	2.55
MagnetBottom and Cryocooler	2.30
Leads and Cryocooler	2.50
Persistent Mode	
MagnetTop and Cryocooler	0.82
MagnetBottom and Cryocooler	0.73
Leads and Cryocooler	0.60

Table 27: Approximated 4.2 K stage temperature differences.

Temperature differences between the first stage of the cryocooler and the strongback and HTS current leads are given in Table 28. Since the first stage of the cryocooler is operating at approximately 27 K in charging mode (Table 24), and 25 K in persistent mode, the strongback temperature will range from 29 to 32 K. Since these temperatures are lower than approximated for the radiative heat load calculations through the insulation, the heat load to the 1st stage will be slightly higher and the heat load to the 2nd stage will be slightly lower.

From Table 28, the temperature of the warm ends of the HTS current leads will be 43 K and 37 K for charging and persistent modes respectively. Since the HTS current lead's warm end was approximated to be 40 K for the heat load calculations these temperature differences are very reasonable. If the magnet does not reach low enough temperatures, the thermal pathways between the cryocooler and the strongback could be improved by using thicker copper links. This would decrease the temperature of the strongback and thereby decrease the heat transfer to the second stage cryocooler.

Path	Temperature Difference (K)
Charging Mode	
Strongback and Cryocooler	5.4
Current Leads and Cryocooler	16.2
Persistent Mode	
Strongback and Cryocooler	4.2
Current Leads and Cryocooler	11.8

Table 28: Approximated first stage temperature differences

7 Temperature Sensors

Temperature sensors are needed on the magnet, busbar and strongback of the system to ensure that the magnet is at 4.2 K before charging the magnet to maximum current. Before choosing a temperature sensor, the requirements of temperature sensors must be determined. Some of these requirements may include temperature range, magnetic field operation, stability, thermal response time, signal measurement, accuracy, repeatability and expense. Most of the operation information of cryogenic temperature sensors and the required instrumentation are provided in the Lake Shore Cryotronics catalogue [90] and the relevant information will be summarized in this chapter. The catalogue also includes information on calibration, mounting, and measurement uncertainty calculations, which will also be discussed.

For this apparatus, the sensors on the magnet and busbar must measure accurate temperatures in the range of 3-6 K and the sensor on the strongback must measure down to 20 K. The sensors must also be able to operate in a magnetic field of 1.25 Tesla. Thermal response time of the sensor is not as important since the superconducting magnet system will mostly be in a stable state, however the sensor must be stable and give repeatable measurements. The expense must be as low as possible while still meeting the main requirements.

7.1 Types of Sensors

There are four main types of temperature sensors: diodes, resistors, capacitors, and thermocouples. Capacitors and thermocouples are generally not used for accurate temperature measurements. This leaves diodes and resistors. There are many types of diode and resistor sensors, however, only the sensors that can operate satisfactorily in a magnetic field and at low temperatures are considered in this report.

Diode temperature sensors that can be used at low temperatures and in a magnetic field include the Silicon diodes and the Gallium-Aluminum-Arsenide (Ga-Al-As) diodes. Some problems of these sensors are that the silicon diode is strongly orientation dependent in a magnetic field below 50 K and the Ga-Al-As diode has low sensitivity at temperatures in the range of 30 K to 110 K. These sensors could be combined with the Ga-Al-As diodes measuring the 4.2 K to 30 K temperatures and the silicon diodes measuring temperatures from 20 K to room temperature with one power source. The magnetic field induced errors of the sensors in these temperature ranges are fairly reasonable since the Ga-Al-As diodes have a maximum temperature error of 2.9% or +0.12 K at 4.2 K and the silicon diodes have a maximum temperature error of –10% (-2 K) parallel to the field and – 4 % (-0.8 K) perpendicular to the field.

Resistance temperature sensors suitable for low temperature measurement in a magnetic field include Cernox™, Carbon-Glass™, Rox™, and Platinum Resistors. The Cernox™ and Carbon-Glass™ all have very good sensor accuracy and the lowest temperature error due to magnetic field at low temperatures. Cernox sensors can be used in all low temperature ranges, with different sensors having high sensitivity in different temperature ranges. They are not as sensitive to temperature changes above 100 K, however, these changes are not as important in this application. Carbon-Glass sensors are also not very sensitive above 100 K and are more expensive than the Cernox sensors so were not considered as an option for this system. The Rox sensors are excellent for measuring temperatures below 3 K but are not very sensitive above 10 K so are not suitable for this application. Finally, the platinum resistors are a relatively inexpensive method of measuring temperatures from 40 K to 300 K. They have high reproducibility and good stability over time.

The choices for this application are now narrowed down to the Ga-Al-As diodes and Silicon diodes, Cernox resistive sensors, and Platinum resistive sensors. Because the Cernox have better performance in a magnetic field and sensors can be selected that are more sensitive in the 30 K region, they were chosen over the diodes. Platinum sensors are also used to measure temperature from room temperature to 40 K since they are an inexpensive addition.

7.2 Instrumentation and Installation

For both diode and resistance sensors, a current must be passed through the sensor to produce a voltage drop that can be measured and used to determine the temperature. If the leads to measure the voltage drop are the same as the leads that supply the current (two-lead measurement) then an error is introduced due to the resistance of the lead wires. To eliminate this error, it is best to connect the wires with separate leads for the current supply and the measurement (four-lead measurement). In this case, the resistance in the measurement (voltage) leads is not measured since only a very small current is required by the voltmeter to make the voltage measurement. In some cases where either the measured resistance is very high or the resultant error can be tolerated, the two-lead measurement will be sufficient, however, it is recommended to use a four-lead measurement whenever possible.

Both diodes and resistance sensors require current sources, however, diodes require a constant 10 μA current source and resistors require a variable current source from 1 mA to 0.01 μA. The constant current source does make diodes easier to use and measure but the increased accuracy of the Cernox resistive sensors is still desired in this case. Since the current must be known to determine the voltage drop, all the sensors must be either connected in series or, for a high cost, separate current sources must be used. Therefore, since the diodes and resistors operate at different currents, it is best to not combine them in an apparatus. Also, the resistors must have similar resistances in the temperature ranges they are measuring so that the voltage drop is in a detectable range. This led to the decision of using Cernox sensors CX-1050 on the 4.2 K stage and CX-1080 on the 40 K stage from Lake Shore Cryotronics [90].

Platinum sensors and Cernox sensors cannot be used with the same current source at the same time. This is because the resistance of Cernox sensors decreases with temperature whereas the Platinum sensors resistance increases with temperature. Instead, the Platinum sensors are used first, then, once the temperature is approximately 40 K, the current source is switched from the platinum sensors to the Cernox sensors.

To prevent heat from leaking from the room temperature environment to the cold environment through the electrical leads of the temperature sensors, the leads are made very small in diameter, generally 32 AWG and are made of high electrical resistance materials. For this experiment, 32 AWG non-magnetic phosphor-bronze wire is used. The wires are heat sunk at several temperatures by winding them around copper bobbins. It is recommended that the wires be insulated from the bobbins using cigarette paper then varnished to the heat sink using IMI-7031 varnish for better thermal contact.

7.3 Sensor mounting

The Cernox sensors were ordered in a 4-wire CU package. This means the sensor has already been thermally attached to a copper bobbin and the wires are also anchored to this bobbin. The bobbin is then screwed on to the measurement surface with a layer of Apiezon N-grease between the bobbin and the surface. The Platinum sensor packages are small cylinders. They are mounted to the strongback by drilling holes in the strongback and placing the sensors in the holes with Apiezon grease. The sensors must be shielded from radiation by using insulation or a copper thermal shield.

7.4 Calibration

One CX-1050 and CX-1080 sensor was ordered calibrated from LakeShore. The other Cernox sensors will be calibrated using the Lakeshore calibrated sensors. The Platinum sensors follow standard curves with specified tolerances.

7.5 Circuit

The Cernox sensors have a recommended excitation of 10 mV. With the CX-1050 sensor operating at 4.2 K and the CX-1080 sensor operating at 40 K the resistances of the sensors are approximately 5128 Ω and 2050 Ω respectively. The variable current source used in this experiment is the Lake Shore model 120CS. Using the 3 μA current setting of the 120CS gives an excitation of 15.4 mV for sensor CX-1050 and 6.15 mV for sensor CX-1080. These values are large enough to be measured and small enough to not cause a large amount of self-heating. To measure higher temperatures, the current must be increased to compensate for the decreasing resistance of the sensors. The sensors are wired in series with phenolic terminals to ensure that all sensors receive the same known current.

The platinum sensors will be operating at a constant current of approximately 2 mA. This will result in a voltage signal between 0.03 V and 0.2 V in the operating temperature range. These sensors will also be wired in series with the phenolic terminals.

7.6 Temperature Measurement Uncertainty

The Cernox and Platinum sensors are resistive sensors and therefore output a resistance that must be measured. Uncertainties in the measurement are therefore in resistive units (ohms) and not in temperature units. To convert to temperature units, the formula

$$\frac{u_T}{T} = \frac{u_R / R}{(T/R)(dR/dT)} \equiv \frac{u_R / R}{S_T} \tag{39}$$

is used, where u_T is the temperature uncertainty, T is the temperature, u_R is the resistive uncertainty, R is the resistance, and S_T is defined as the dimensionless temperature sensitivity and is given for each sensor. Because this formula is dimensionless it can also be applied to sensors that depend on voltage by replacing R with V as appropriate.

In this apparatus, the platinum sensors are used to give an approximate temperature reading and therefore the uncertainty in these sensors is not important. For the Cernox sensors where high accuracy is desired, there are several sources of uncertainty that must be approximated including:

1. Instrumentation measurement uncertainty

The measurement instrument is a National Instruments PCI-6035E DAQ card that has eight differential channels of 16-bit analog input, two channels of 12-bit analog output, a 68-pin connector, and eight lines of digital I/O [91]. The voltage uncertainty is given as a percentage of the reading ± an offset voltage ± the error due to noise [92]. This uncertainty must be converted to a resistance uncertainty using the V=IR formula. Equation 39 can then be used to determine the temperature uncertainty.

2. Excitation uncertainty

Excitation uncertainty is due to an uncertainty in the excitation current. The current source used in this apparatus is the Lake Shore Model 120CS which has a specified accuracy of 0.1% at a current of 3 μA.

3. Thermal noise, thermoelectric and zero offset voltages

Electrical noise created by the motion of particles with thermal energy is negligible. Thermoelectric and zero offset voltages are created when dissimilar metals are joined and the joints are held at different temperatures. Using current reversal, this uncertainty can be eliminated. Electromagnetic pickup noise can also be eliminated using current reversal and also by twisting the wire pairs.

4. Sensor self heating

Power dissipation in a sensor is necessary to make a temperature measurement, however this dissipation also causes the temperature of the sensor to rise. Therefore, it is necessary to balance the uncertainties due to self-heating and output signal measurement. To calculate the self-heating, the thermal resistance between the sensor and its environment, R_t, must be known. The thermal resistance should be determined experimentally since it is very difficult to calculate and values will change from experiment to experiment since surface conditions are not repeatable. However, since only an approximate value is desired for this application, experimental values are used.

Courts *et al.* [93] measured the thermal resistance of Cernox 1050 and 1070 SD packages. These SD packages are mounted with Apiezon N-grease to a copper block. As mentioned previously, in our apparatus CU packages are used which are SD packaged sensors soldered into a flat, copper bobbin and the CU package is screw mounted to a copper block with Apiezon N-grease. For an approximation, it is assumed that the thermal resistance of the CU package is twice that of the SD package alone. Also, the thermal resistance of CX-1070 is assumed to be the same of CX-1080. The approximate values given by Courts *et al.* [93] are 9×10^3 K/W and 3.2×10^2 K/W for CX-1050 at 4.2 K and CX-1070 at 40.6 K respectively.

5. Calibration uncertainty, and calibration fit interpolation uncertainty

The calibration uncertainty is due partly to the accuracy of the national standards which the sensors were calibrated to. As the standards are applied to different devices used to transfer a calibration the uncertainty increases. The value of the uncertainty is given by Lakeshore [90] for each sensor. To determine the temperatures that lie between calibration points an interpolation function is required. This function adds to the uncertainty of the measurement typically by a factor of one-tenth the calibration uncertainty.

Once all the uncertainties have been determined, they can be combined using the formula

$$u_c = \sqrt{u_1^2 + u_2^2 + \ldots + u_n^2} \tag{40}$$

where u_c is the combined uncertainty. Example uncertainty calculations are shown in Table 29 for Cernox sensors CX-1050 and CX-1080. The resistance and sensitivity data is taken from the Lake Shore catalogue sensor data tables [90]. The total combined uncertainties are ±8.1 mK and ±0.149 K for the CX-1050 and CX-1080 respectively which are acceptable values.

Temperature Sensor Model		CX-1050-CU		CX-1080-CU	
Temperature, T		4.2 K		40 K	
Mounting Environment (N-greased to block)		vacuum		vacuum	
Static Electrical Resistance, Rs (from table)		5128 Ω		2050 Ω	
Dynamic Electrical Resistance, Rd (from table)		5128 Ω		2050 Ω	
Excitation Current, I		3 µA		3 µA	
Output Voltage, V		15.4 mV		6.15 mV	
Dimensionless Temperature Sensitivity, ST		-1.9		-1.6	
Uncertainties due to		Value used	Temperature Uncertainty u_T/T (PPM)	Value used	Temperature Uncertainty u_T/T (PPM)
1	Measurement Instrumentation (NI PCI-6035E)				
	meter full scale range	50 mV		50 mV	
	voltage accuracy specification	0.0646%+/- 28.9µV+/- 2.57µV		0.0646%+/- 28.9µV+/- 2.57µV	
		4.14E-05 V	-1417	3.54E-05 V	-3602
2	Excitation Uncertainty (LSCI model 120CS)				
	current accuary specification	u_I/I=0.1 %	-526	u_I/I=0.1 %	-625
3	Sensor Self Heating				
	thermal resistance	18000 K/W	198	640 K/W	0.3
4	Calibration Uncertainty	5 mK	1190	30 mK	750
5	Interpolation uncertainty		119		75
Combined Uncertainties (ppm)			1928		3733
Combined Uncertainties (mK)			8.1		149

Table 29: Temperature Uncertainty Approximation Example.

7.7 Placement of the Sensors

After the vessel is assembled, the temperature sensors will be calibrated on copper plates attached to the cryocooler. They will then be placed in their designated positions to measure the required temperatures.

Two CX-1050 sensors are placed on the superconducting magnet, one on the top and one on the bottom, to monitor the temperature of the magnet. One CX-1050 is placed on the copper block that the current leads are attached to on the busbar to measure the approximate temperature of the current leads, and one is placed as close as possible to the 2nd stage of the cryocooler so that the temperature of the cryocooler is known. The temperature of the 1st stage of the cryocooler is measured with one CX-1080 sensor mounted directly to the 1st stage. Finally, one CX-1080 sensor is mounted on the strongback at the furthest point away from the 1st stage of the cryocooler so that an approximate shield temperature is known. Once the magnet is operating, the resulting temperature measurements will be used to validate the total heat calculations performed in the previous chapters.

8 Conclusions and Future Work

This thesis presents the analysis and design of a cryostat for a conduction-cooled 1.25 Tesla superconducting magnet to be used in THM growth of CdZnTe. As an applied magnetic field has never before been used to grow CdZnTe crystals by THM, this is the first published work of the design of a superconducting magnet cryostat for this purpose. Other researchers have previously examined the individual topics included in this work however this thesis is a unique collection of these topics.

The decision to use a superconducting magnet rather than a room temperature solenoid magnet was based on the power requirements of the solenoid. The solenoid was found to require excessive amounts of power and an extreme amount of cooling that would have cost a great deal. Thus, the superconducting magnet was chosen. The magnet was built and designed by an outside company and a cryocooler was purchased to cool the magnet system.

The vacuum vessel designed to contain the magnet has an inner bore that allows the THM furnace to be placed in the center of the magnet and also allows adequate insulation between the vessel surface and the magnet. It was made of non-magnetic 304 stainless steel and the walls were optimized to have a thickness of 0.32 cm (0.125 in). The lids were also analyzed for deflection and bending stress and a thickness of 1.59 cm (0.63 in) was chosen as acceptable. The welds and flanges were designed using standard practices.

Supports were designed to hang the magnet from the lid of the vacuum vessel and to prevent horizontal movement. G10 material was chosen and the minimum cross-sectional area was determined that would allow an adequate strength safety factor for the weight and thermal contraction of the supports and minimize the conductive heat transfer to the magnet. The brackets for the G10 supports were designed for simple bolt joints and the stress in the brackets was analyzed.

The magnet current leads, composed of a metal and a HTS section, were also designed to minimize heat transfer. The metal component of the leads was optimized in length and cross section to reduce the joule heating and conductive heat to a minimum. To perform this optimization, the electrical resistivity and thermal conductivity as a function of temperature were approximated. Since the precise RRR of ETP copper was unknown, the optimization was evaluated for values of 40 and 90 and the difference in results was shown to be negligible. The total heat transfer from the metal and HTS leads, including electrical contact resistance but excluding thermal contact resistance, was determined.

The thermal shield and NRC-2 insulation was optimized to reduce the radiative heat transfer to the magnet. This optimization required the approximation of the effective conductivity of the insulation including several variable factors. Optimization of the insulation in the bore of the magnet from the room temperature wall to the 40 K thermal shield led to the determination of the required thermal shield radius. Aluminum tape is used as insulation from the 40 K thermal shield to the 4.2 K magnet. Aluminum tape has been used successfully by previous experimenters however the Compac brand 5 mil aluminum tape chosen for this apparatus has never before been tested.

The total heat transfer to the first and second stages of the cryocooler was approximated. After analyzing the thermal resistance of the contacts the temperature difference between the magnet and the cryocooler was estimated. These temperature differences were found to be acceptable in the persistent mode but may be too high in the charging mode. This is probably not a problem since the magnet will not usually be operating at maximum field however increasing the thickness of the thermal connections could reduce these temperature differences.

Finally, the temperature sensors and instrumentation required for monitoring the state of the magnet are discussed and the uncertainty of the measurements is approximated. The sensors will be placed on the strongback, cryocooler, busbar, and magnet so that estimated temperature differences can be verified.

Assembly of the superconducting magnet cryostat is in progress. The vacuum vessel has been assembled to ensure that all components were properly machined as shown in Figure 27.

Figure 27: Assembled superconducting magnet vacuum vessel.

The vessel has been successfully placed under vacuum of 1×10^{-7} Torr. The wiring of the instrument feedthroughs has also begun and temperature sensor bobbins and terminal strips have been placed on the busbar, shown in Figure 28, and strongback.

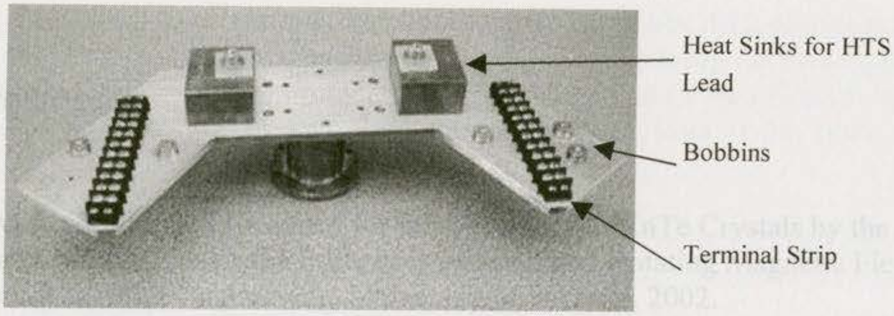

Figure 28: Busbar to attach to 2nd stage of the cryocooler.

The next steps in constructions are:

- Sewing the NRC-2 insulation blankets
- Calibration of temperature sensors
- Insert the superconducting magnet
- Cool magnet and ensure magnet reaches a temperature of 4.2 K
- Charge magnet

Once the magnet is operating, it can be immediately used in the THM growth experiments of CdZnTe.

9 References

[1] Crowle, M.R. Equipment Designed for the Growth of CdZnTe Crystals by the Traveling Heater Method Under the Influences of Static and Rotating Magnetic Fields. MASc Thesis, Mechanical Engineering, University of Victoria, 2002.

[2] Senchenkov, A.S., Barmin, I.V., Tomson, A.S., Krapukhin, V.V. Seedless THM growth of $Cd_xHg_{1-x}Te$ (x~0.2) Single Crystals within Rotating Magnetic Field. Journal of Crystal Growth, Vol 197, No. 3, 1999. pp. 552-6.

[3] Barmin, I.V., Egorov, A.V., Senchenkov, A.S. Results of Crystal Growth Experiments by FZM on Zona Facilities in Microgravity. Proceedings VIIIth European Symposium on Materials and Fluid Sciences in Microgravity, Brussels, Belguim, 12-16 April 1992. p. 591.

[4] Barmin, I.V., Senchenkov, A.S. Technological Equipment of SPLAV Technical Center for Producing Materials in Space. Some Results of the Experiments on Crystal Growth. Microgravity Q., Vol. 3, No. 2-4, 1993. pp. 233-239.

[5] Benz, K.W., Dold, P., Croll, A., Schweizer, M., Kaiser, Th., Lichtensteiger, M., Szofran, F.R. Comparison of the Effect of Microgravity and Magnetic Fields on the Crystal Growth of Floating Zone Silicon. SPIE Conference on Materials Research in Low Gravity II, Denver, Colorado, July 1999. SPEI Vol. 3792.

[6] Sheibani, H., Sakai, S., Dost, S., Lent, B. LPEE Growth of Binary and Ternary Crystals Under Applied Magnetic Field-Experimental. The 13th International Symposium on Transport Phenomena, Victoria, B.C. July 14-18, 2002. pp. 599.

[7] Dost, S., Qin, Z. A Model for Liquid Phase Electroepitaxy Under an External Magnetic Field, I. Theory. Journal of Crystal Growth Vol. 153, 1995. pp. 123-130.

[8] Dost, S. Numerical Simulation of Liquid Phase Electroepitaxial Growth of GaInAs Under Magnetic Field. ARI Vol 51, 1999. pp. 235-246.

[9] Dost, S., Liu, Y., Lent, B., Redden, R.F. A Numerical Simulation Study for the Effect of Applied Magnetic Field in Growth of CdTe single Crystals by the Traveling Heater Method. International Journal of Applied Electromagnetics and Mechanics, 2003. In Press.

[10] Salk, M., Fiederle, M., Benz, K.W., Senchenkov, A.S., Egorov, A.V., Matiuokhin, D.G. CdTe and CdTe0.9Se0.1 Crystals Grown by the Travelling Heater Method Using a Rotating Magnetic Field. Journal of Crystal Growth, Vol. 138, 1994. pp. 161-167.

[11] Gelfgat, Y., Krumin, J., Abricka, M. Application of Combined Electromagnetic Fields for Controlling the Hydrodynamics and Heat/Mass Transfer in the Processes of Bulk Single Crystal Growth. Third International Conference on Crystal Growth, Strength Problems and Heat Mass Transfer, (ICSC99), Obninsk, Russia, Sept 21-24, 1999. Abstracts p. 201.

[12] Liu, Y.C., Okano, Y., Dost, S. The Effect of Applied Magnetic Field on Flow Structures in Liquid Phase Electroepitaxy – A Three-Dimensional Simulation Model. Journal of Crystal Growth, Vol. 244, 2002. pp. 12-26.

[13] Sheibani, H., Liu, Y., Sakai, S., Lent, B., Dost, S. The Effect of Applied Magnetic Field on the Growth Mechanisms of Liquid Phase Electroepitaxy. International Journal of Engineering Science, Vol. 41, 2003. pp. 401-415.

[14] Montgomery, D.B. Solenoid Magnet Design, The Magnetic and Mechanical Aspects of Resistive and Superconducting Systems. John Wiley & Sons, Inc., New York. 1969.

[15] American Magnetics, Inc. P.O. Box 2509, 112 Flint Road, Oak Ridge, TN 37831-2509. Phone: (865) 482-1056, Fax: (865) 482-5472. http://www.americanmagnetics.com

[16] Janis Research Company, Inc. No. 2 Jewel Drive, P.O. Box 696, Wilmington, MA 01887-0696. TEL: (978) 657-8750, FAX: (978) 658-0349 http://www.janis.com/p-cfms.html

[17] CRYO Industries of America, Inc., 11124 S. Willow Street, Manchester, NH 03103 Tel: (603) 621-9957, Fax: (603) 621-9960

http://www.cryoindustries.com/magsys.htm

[18] Burgoyne, J.W., Daniels, P.D., Timms, K.W., Vale, S.H. Advances in Superconducting Mangets for Commercial and Industrial Applications. IEEE Transactions on Applied Superconductivity, Vol. 10, No. 1, March 2000. pp. 703.

[19] Cooper, T.L., Walters, J.D., Fikse, T.H. Thermal Conductance of Heat Transfer Interfaces for Conductively Cooled Superconducting Magnets. Advances in Cryogenic Engineering, Vol. 41. Plenum Press, NY. (1996). Pp. 297-304.

[20] Hasebe, T. et al. Cryocooler Cooled Superconducting Magnets and their Applications. Advances in Cryogenic Engineering, Vol. 43. Plenum Press, NY. 1998. 291-297.

[21] Hata, F., Sakuraba, J., Chong, C.K., Yamada, Y., Hasebe, T., Ishihara, M., and Watanabe, K. A Conduction Cooled Superconducting Magnet Using High-Tc Oxide Current Leads. MT-13 Conference, (Victoria sept.93)

[22] Kuriyama, T. *et al.* Cryocooler Directly Cooled 6 T NbTi Superconducting Magnet System with 180 mm Room Temperature Bore. Cryogenics, Vol 34. ICEC Supplement. 1994.

[23] Masuyama, S. Yamamoto, H., Matsubara, Y. A NbTi Split Magnet Directly Cooled by a Cryocooler. IEEE Transactions on Applie Superconductivity, Vol. 3, No. 1 March 1993. pp. 262,

[24] Obasih, K.M. and Mruzek, M.T. Thermal Design and Analysis of a Cryogenless Superconducting Magnet for Interventional MRI Therapy. Advances in Cryogenic Engineering, Vol. 41. Plenum Press, NY. (1996) pp. 305-311.

[25] Rowe, A., Barclay, J.A., Dost, S. Design of an Apparatus for a 5T Conduction Cooled NbTi Solenoid with a 203 mm Room Temperature Bore. Advances in Cryogenic Engineering, Vol 45. Plenum Publishers, 2000. pp. 651-658.

[26] Shibutani, K. et al. Development of Two Types of Cryogen Free Superconducting Magnet. Advances in Cryogenic Engineering, Vol. 43. 1998. pp. 299-305.

[27] Snitchler, G., Kalsi, S.S., Manlief, M., Schwall, R.E., Sidid-Yekhlef, A., Ige, W., Medeiros, R. High-Field Warm-Bore HTS Conduction Cooled Magnet. Invited Talk at 1998 Applied Superconductivity Conference. Desert Springs, CA, September 1998.

[28] Song, N.H. et al. A Cryocooler Directly Cooled 5 Tesla Niobium Titanium Superconducting Magnet System. Advances in Cryogenic Engineering, vol 45. Kluwer Academic/Plenum Publishers (2000). pp. 667-674.

[29] Takahashi, H. et al. A 7.7 T NbTi Superconducting Magnet System Cooled by a 4 K GM Refrigerator. Advances in Cryogenic Engineering. Vol. 39. Plenum Press, NY. (1994) pp. 343-350.

[30] van Oort, J.M. et al. A Cryogen-Free 0.5 Tesla MRI Magnet for Head Imaging. Advances in Cryogenic Engineering, Vol. 43. Plenum Press, NY. (1998) pp. 139-147.

[31] Squires, B. et al. Design of the 2 Tesla Superconducting Solenoid for the Fermilab D0 Detector Upgrade. Advances in Cryogenic Engineering. Vol 39. Plenum Press, NY. (1994). Pp. 301-308.

[32] Chang, H., Kim, H. Development of a Thermal Switch for Faster Cool-Down by Two-Stage Cryocooler. Cryogenics, Vol. 40, 2000. pp. 769-777.

[33] RDK-415 Sumitomo (SHI) 4 K Refrigerator, Janis Research Company, Inc. 2 Jewel Drive, P.O. Box 696, Wilmington, MA 01887-0696. TEL: (978) 657-8750,
FAX: (978) 658-0349
http://www.janis.com/p-a4k11.html

[34] ASME Boiler and Pressure Vessel Code, Section VIII, Rules for Construction of Pressure Vessels, Division 1. 1992 Edition, July 1, 1992.

[35] Bednar, H.H. Pressure Vessel Design Handbook. Van Nostrand Reinhold Company, New York, 1981.

[36] Young, W.C. Roark's Formulas for Stress & Strain, Sixth Edition. McGraw-Hill Inc. 1989.

[37] Flynn, T.M. Cryogenic Engineering. Marcel Dekker, Inc., 1997.

[38] inPHormTM O-Rings, Version 2.0.2. Parker Seals, 1994-1999. Parker Hannifin Corporation, Cleveland, Ohio.
http://www.parker.com/inphorminfo/

[39] Simrit – North American Headquarters, 47690 East Anchor Court, Plymouth, MI 48170, Phone:(866) 2-SIMRIT, Fax: (734) 354-5500
http://www.simritna.com/catalog/o-ring/991applications.htm

[40] Apple Rubber, 1.800.828.7745 (US and Canada Only), Tel: 716.684.6560, Fax: 716.684.8302.
http://www.applerubber.com

[41] Weisend II, J.G. Handbook of Cryogenic Engineering. Taylor and Francis, 1998.

[42] Marquardt, E.D., Le, J.P., Radebaugh, R. Cryogenic Material Properties Database. National Institute of Standards and Technology. 11th International Cryocooler Conference. June, 2000.

[43] GE Polymershapes Thermoset Industrial Laminate Properties, Minimum Values. 3917 Grant Street, Burnaby, BC V5C 3N4, Phone: 604-298-1945, Fax: 604-298-1941
http://www.gepolymershapes.com

[44] Kasen, M.B., MacDonald, G.R., Beekman, D.H.Jr, Schramm, R.E. Mechanical.Electrical, and Thermal Characterization of G-10CR and G-11CR Glass-Cloth/Epoxy Laminates Between Room Temperature and 4 K. Advances in Cryogenic Engineering, Materials. Vol. 26, 1980. pp. 235.

[45] Lewis, W., Samuel, A. Fundamentals of Engineering Design. Prentice Hall, 1989.

[46] Shigley, J.E., Mischke, C.R. Fastening, Joining, and Connecting, A Mechanical Designers' Workbook. McGraw-Hill Publishing Company, 1990.

[47] Megyesy, E.F. Pressure Vessel Handbook, Eighth Edition. Pressure Vessel Handbook Publishing, Inc. 1989.

[48] Mumford, F.J. Superconducting Current-Leads made from High Tc Superconductor and Normal Metal Conductor. Cryogenics, Vol. 29, 1989. pp. 206.

[49]Bogdanov, I., Kozub, S., Myznikov, K et.al. Application of HTS BI-2223 For Current Leads of Superconducting Magnets. Proceedings of EPAC 2000, Vienna, Austira.

[50]Chang, H., VanSciver, S.W. Thermodynamic Optimization of conduction-Cooled HTS Current Leads. Cryogenics, Vol. 38, 1998. pp. 729-736.

[51] Herrmann, P.F., Cottevieille, C., Duperray, G., Leriche, A., Verhaege, T., Albercht, C., Bock, J. Cryogenic Load Calculation of High Tc Current Lead. Cryogenics, Vol 33, 1993. pp. 555.

[52] Daugherty, M.A., Daney, D.E., Prenger, F.C., Hill, D.D., Williams, P.M., Boenig, H.J. Assembly and Testing of a Composite Heat Pipe Thermal Intercept for HTS Current Leads. Advances in Cryogenic Engineering, Vo. 41, 1996. pp. 579.

[53] Lock, J.M. Optimization of Current Leads into a Cryostat. Cryog. 9, 1969. pp. 438

[54] Jones, M.C., Yeroshenko, V.M., Strostin, A., Yaskin, L.A. Transient Behaviour or Helium-Cooled Current Leads for Superconducting Power Transmission. Cryog.. 18, 1978. pp. 337

[55] Powell, R.L., Roder, H.M., Rogers, W.M. Low-Temperature Thermal Conductivity of Some Commercial Coppers. J. Applied Physics. Vol 28, No. 11, 1957. pp. 1282

[56] Maehata, K., Ishibashi, K., Wakuta, Y. Design Chart of Gas-Cooled Current Leads Made of Copper of Different RRR Values. Cryogenics, Vol. 34, 1994. pp. 935.

[57] Smith, C.O. The Science of Engineering Materials. Third Edition. Prentice-Hall, Inc., 1986. pp. 554.

[58] McFee, R. Optimum Input Leads for Cryogenic Apparatus. The Rev. Sci. Inst. Vol. 30 1959. pp. 98.

[59] Powell, R.L., Coffin, D.O. Low-Temperature Thermal Conductivity of a Free-Machining Copper. Rev. Sci. Instr. Vol. 26, 1955. pp. 516

[60] Dauphinee, T.M., Preston-Thomas, H. A Copper Resistance Temperature Scale. Rev. Sci. Instr. Vol 25, #9, 1954. pp. 884

[61] American Superconductor CryoSaver^{TM} Current Leads, Two Technology Drive Westborough, MA. 01581.
www.amsuper.com

[62] Farahat, M.A. Gockenbach, E., El-Alaily, A.A., Abdel Aziz, M.M. Effect of Coating Materials on the Electrical Performance of Copper Joints. Proceedings of the 42nd IEEE Holm Conference on Electrical Contacts, 1996. pp. 472.

[63] Timsit, R.S. Electrical Contact Resistance: Properties of Stationary Interfaces. IEEE Trans. on Components and Packaging Technology, Vol. 22, No. 1, 1999. pp. 85.

[64] Nilles, M.J., Van Sciver, S.W. Effects of Oxidation and Roughness on Cu Contact Resistance from 4 K to 290 K. Advances in Cryogenic Engineering, Vol. 34, 1988. pp. 443.

[65] Sato, K., Okumura, H., Yamaguchi, S. Numerical Calculations for Peltier Current Lead Designing. Cryogenics, Vol, 41, 2001. pp. 497.

[66] Xuan, X.C., Ng, K.C., Yap, C., Chua, H.T. Optimization and Thermodynamic Understanding of Conduction-Cooled Peltier Current Leads. Cryogenics, Vol 42, 2002. pp.141.

[67] Barron, R.F. Cryogenic Heat Transfer. Taylor & Francis, 1999.

[68] Metallized Products, Inc. 37 East St., Winchester, MA 01890
Phone: 781.729.8300

[69] Eyssa, Y.M., Okasha, O. Thermodynamic Optimizaton of Thermal Radiation Shields for a Cryogenic Apparatus. Cryogenics, Vol 18, no. 5, 1978. pp. 304-307.

[70] Scurlock, R.G., Saull, B. Development of Multilayer Insulations with Thermal Conductivities Below 0.1 μW cm^{-1}K^{-1}. Cryogenics. May 1976. pp. 303.

[71] Kumar, A.S., Murthy, M.V.K., Jacob, S., Kasthurirengan, S. Thermal Performance of Multilayer Insulation Down to 4.2 K. Advances in Cryogenic Engineering. Vol. 45, 2000. pp. 1675.

[72] Leung, E.M.W., Fast, R.W., Hart, H.L., Heim, J.R. Techniques for Reducing Radiation Heat Transfer Between 77 and 4.2 K. Advances in Cryogenic Engineering, Vol 25, 1980. pp. 489-499.

[73] Spradley, I.E., Nast, T.C., Frank, D.J. Experimental Studies of MLI Systems at Very Low Boundary Temperatures. Advances in Cryogenic Engineering, Vol 35, 1990. pp. 477-486.

[74] Zeller, A.F., DeKamp, J.C., Leung, E.M.W., Fast, R.W. Long Term Results from the Elimination of MLI Between 4 and 77 K. Advances in Cryogenic Engineering, Vol 39, 1994. pp. 1691-1697.

[75] World of Tape Ltd. 11191 Horseshoe Way, Unit 9, Richmond, B.C.,
Tel: 1-888-272-6898, Fax: 604-272-4552.
www.worldoftape.com

[76] RDK-415 Load Map, Janis Research Company, Inc. 2 Jewel Drive, P.O. Box 696 Wilmington, MA 01887-0696. TEL: (978) 657-8750 FAX: (978) 658-0349
http://www.janis.com/p-a4k11.html

[77] Assemblage Paro Inc., 495, de l'Aviation,Cap-de-la-Madeleine (Québec)G8T 5M4 Canada. Tél.: (819) 375-3503 Fax: (819) 373-2448

[78] Holm, R., Holm, E. Electric Contacts, Theory and Application. Fourth Edition. Springer-Verlag New York Inc., 1967.

[79] Berman, R. Some Experiments on Thermal Contact at Low Temperatures. Journal of Applied Physics, Vol. 27, No. 4, 1956. pp. 318.

[80] Kittel, P., Salerno, L.J., Spivak, A.L. Thermal Conductance of Pressed Bi-Metallic Contacts at Liquid Nitrogen Temperatures. Presented at ICEC, Genova, Italy, June 7-10, 1994.

[81] Salerno, L.J., Kittel, P., Spivak, A.L. Thermal Conductance of Pressed Metallic Contacts Augmented with Indium Foil or Apiezon Grease at Liquid Helium Temperatures. Cryogenics, Vol. 34, 1994. pp. 649.

[82] Xu, L., Yang, J., Xu, J.M., Li, S.M., Xiong, W., Zhang,T. The Effectof Solid Interfaces on Thermal Contact Resistance at Low Temperature. Advances in Cryogenic Engineering, Vol. 43, 1998. pp. 1369.

[83] Pobell, F. Matter and Methods at Low Temperatures. Springer-Verlag, Berlin Heidelberg, 1992. pp. 71-72.

[84] Williams, B., Jensen, S., Chadek, M., Batty, J.C. Solderless Flexible Thermal Links. Cryogenics, Vol., 36, No. 10, 1996. pp. 867.

[85] Willekers, R.W., Bosch, W.A., Mathu, F., Meijer, H.C., Postma, H. Impact Welding: A Superior Method of Producing Joints with High Thermal Conductivity Between Metals at Very Low Temperatures. Cryogenics, Vol. 29, 1989. pp. 904.

[86] Incropera, F.P., DeWitt, D.P. Fundamentals of Heat and Mass Transfer, Fourth Edition. John Wiley & Sons, 1996. pp. 79-81.

[87] Holman, J.P. Heat Transfer, 8th Edition. McGraw-Hill Companies, Inc., 1997. pp.56-59.

[88] Fried, E. Thermal Conduction Contribution to Heat Transfer at Contacts. R.P. Tye, Ed., Thermal Conductivity, Vol. 2, Academic Press, London, 1969. pp. 253.

[89] Circle Bolt and Nut Co., Inc. http://www.circlebolt.com/SAE%20Grade%20Clamping%20Specification.htm

[90] Lake Shore Cryotronics, Temperature Measurement and Control catalogue, 2002.

[91] National Instruments Corporation, NI 6034E/6035E/6036E User Manual, p. 1-1, A-2.

[92] National Instruments Corporation, Instrumentation Catalogue, Measurment and Automation, 1998. pp. 185.

[93] Courts, S.S., Davenport, W.E., Holmes, D.S. Thermal Resistances of Cryogenic Temperature Sensors from 1-300 K. Advances in Cryogenic Engineering, Vol. 45, 2000. pp. 1849.

Appendix-A

Weight

Table 30 has the weight of all components as they are designed. When calculating stresses due to the weight for the supports and the vacuum vessel shell, the weight was first approximated, then when the dimensions for design were selected and the actual weight was known the calculations were redone.

Component	Weight (lb)	Mass (kg)	Force (N)
Magnet	77	35	343
Extras	40	18	177
Copper Shield	50	23	226
Aluminum Strongback	17	8	78
Cryocooler	40	18	177
SS 304 Bore	34	15	147
SS 304 Outer Shell	73	33	324
SS 304 Lids (2)	238	108	1060
Outer Flanges	75	34	334
Top Inner Flange	8	4	39
Bottom Inner Flange	15	7	69
Totals			
Supported by Shell	357	162	1590
Supported by Strongback	152	69	677
Supported by Lid Supports	169	77	755
Shell	484	220	2160
Total of all components	**663**	**301**	**2950**

Table 30: Weight of superconducting magnet system components.

Appendix-B

Weld Strengths for Brackets

Welds are required on the brackets for supports 1, supports 3 and supports 4. For support 1, the Al 6061-T6 bottom magnet bracket must be welded together and for support 3 the top SS 304 brackets must be welded to the lid of the vessel. For support 4, a bracket must be welded to the inside of the stainless steel cylinder. Also, for assembly, three SS 304 brackets are welded to the outside of the lid and must be able to support the entire load of the superconducting magnet assembly of approximately 3110 N (700 lb). These welds can be examined in drawings SM-04C, SM-04D, and SM-15B in the Appendix-D.

To determine the required size of the fillet weld, the tension, shear and bending forces must be determined. The tension or compression force is given by

$$W_1 = \frac{P_w}{A_w}, \tag{41}$$

where P_w is the allowable concentrated axial load and A_w is the length of the weld. The vertical shear force is given by

$$W_s = \frac{V}{A_w}, \tag{42}$$

where V is the vertical shear. And, the bending force is given by

$$W_b = \frac{M_w}{S_w}, \tag{43}$$

where M_w is the bending moment and S_w is the section modulus of weld lines and is given by

$$S_w = \frac{d_b^{\,2}}{3}, \tag{44}$$

for a rectangular piece, where d_b is the width of the bracket. The resultant force is then

$$W = \sqrt{W_1 + W_s + W_b}\,. \tag{45}$$

The fillet weld size required can now be found and is given by

$$w = \frac{W}{f}, \tag{46}$$

where f is the allowable load on a weld and can be found in tables or is given by the formula

$$f = 0.707\omega 0.3S_t\,, \tag{47}$$

where ω is the leg size and S_t is the minimum tensile strength of the weld metal. For a 2.5x2.5 cm (1"x1") weld on SS 304, f is 88 MPa (12730 lb/in^2), and for a 2.5x2.5 cm weld on Al 6061-T6, f is approximately 59 MPa (8484 lb/in^2) [46]. All of the equations were taken from Megyesy [46] and Shigley [47].

The resulting minimum leg sizes are shown in Table 31. The minimum leg sizes are very small, so common weld sizes of 0.32 cm (1/8 in) and 0.64 cm (1/4 in) are used and will easily handle the required loads. Note that for the lid support brackets, a safety factor of 3 was used on the weight of the magnet vessel. Also, for supports 4, the amount of horizontal force on the cylinder bracket is unkown so the weld size was not calculated. A practical weld size of 0.32 cm (1/8 in) was chosen for support 4 bracket weld.

Support bracket	W1 (N/m)	Ws (N/m)	Wb (N/m)	f (MPa)	W (kN/m)	ω_{min} (cm)	ω (cm)
1	3370	1480	6660	59	7.53	0.0130	0.32
3	1410	977	5180	88	5.43	0.0061	0.32
lid	2540	1540	138000	88	142	0.162	0.64

Table 31: Weld leg sizes.

Appendix-C

Thermal Path Temperature Differences

Path	Area (m^2)	Length (m)	Thermal Conductivity (W/m-K)	Thermal Conductance (mW/K)	Heat load (W)	Temperature Difference (K)
cryocooler to extender				798	0.15	0.193
extender	1.46E-03	4.47E-02	320		0.15	0.015
extender to busbar				798	0.15	0.193
Total						**0.401**

Table 32: Temperature Difference Between Cryocooler and Busbar (Persistent mode)

Path	Area (m^2)	Length (m)	Thermal Conductivity (W/m-K)	Thermal Conductance (mW/K)	Heat load (W)	Temperature Difference (K)
cryocooler to extender				798	0.54	0.681
extender	1.46E-03	4.47E-02	320		0.54	0.052
extender to busbar				798	0.54	0.681
Total						**1.413**

Table 33: Temperature Difference Between Cryocooler and Busbar (Charging mode)

Path	Area (m^2)	Length (m)	Thermal Conductivity (W/m-K)	Thermal Conductance (mW/K)	Heat load (W)	Temperature Difference (K)
CuLead to Copper Block				295	0.03	0.092
Cu Block	2.26E-03	1.27E-02	320		0.03	0.000
CuBlock to Busbar				277	0.03	0.097
Along Busbar to Cryocooler	4.84E-04	6.10E-02	320		0.03	0.011
Total						**0.200**

Table 34: Temperature Difference Between Leads and Busbar (Persistent mode)

Path	Area (m^2)	Length (m)	Thermal Conductivity (W/m-K)	Thermal Conductance (mW/K)	Heat load (W)	Temperature Difference (K)
CuLead to Copper Block				295	0.15	0.499
Cu Block	2.26E-03	1.27E-02	320		0.15	0.003
CuBlock to Busbar				277	0.15	0.530
Busbar to Cryocooler	4.84E-04	6.10E-02	320		0.15	0.058
Total						**1.089**

Table 35: Temperature Difference Between Leads and Busbar (Charging mode)

Path	Area (m^2)	Length (m)	Thermal Conductivity (W/m-K)	Thermal Conductance (mW/K)	Heat load (W)	Temperature Difference (K)
Busbar to BraidedCu1				980	0.05	0.047
BraidedCu1	2.02E-04	2.60E-01	320		0.05	0.186
BraidedCu1 to MagnetTop				242	0.05	0.190
MagnetTop Total						**0.423**
Busbar to BraidedCu2				980	0.05	0.047
BraidedCu2	2.02E-04	1.30E-01	320		0.05	0.093
BraidedCu2 to MagnetBot				242	0.05	0.190
Magnet Bottom Total						**0.330**

Table 36: Temperature Difference Between Magnet and Busbar (Persistent Mode)

Path	Area (m^2)	Length (m)	Thermal Conductivity (W/m-K)	Thermal Conductance (mW/K)	Heat load (W)	Temperature Difference (K)
Busbar to BraidedCu1	3.23E-03			612	0.124	0.063
BraidedCu1	2.02E-04	2.60E-01	320		0.124	0.500
BraidedCu1 to MagnetTop	1.61E-03			270	0.124	0.285
MagnetTop Total						**0.848**
Busbar to BraidedCu2	3.23E-03			612	0.124	0.063
BraidedCu2	2.02E-04	1.30E-01	320		0.124	0.250
BraidedCu2 to MagnetBot	2.42E-03			270	0.124	0.190
Magnet Bottom Total						**0.503**

Table 37: Temperature Difference Between Magnet and Busbar (Charging Mode)

Appendix-D

SolidWorks Drawings

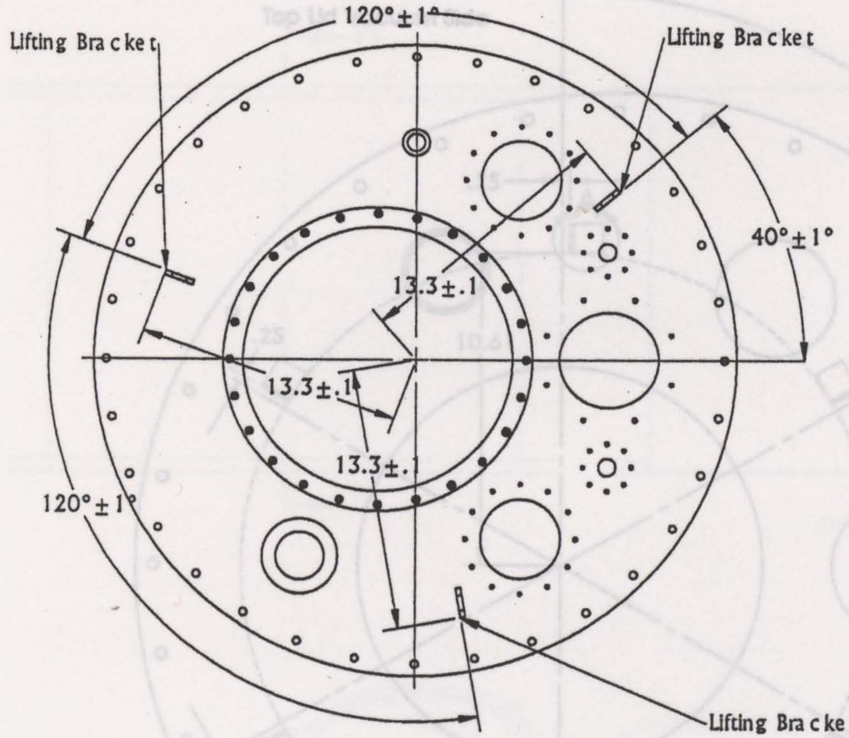

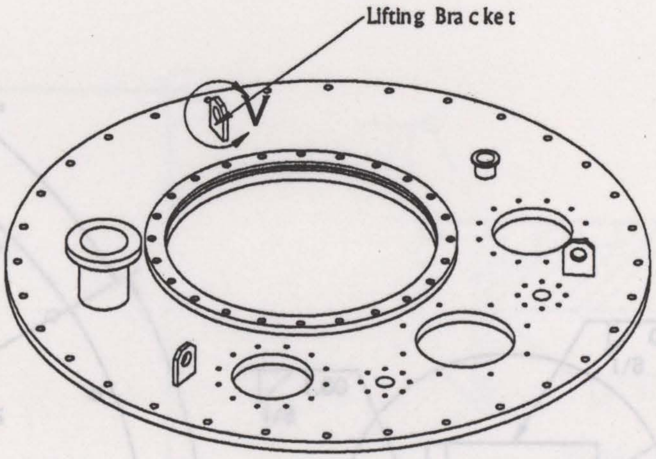

Notes:
Same weld for all three lifting brackets.

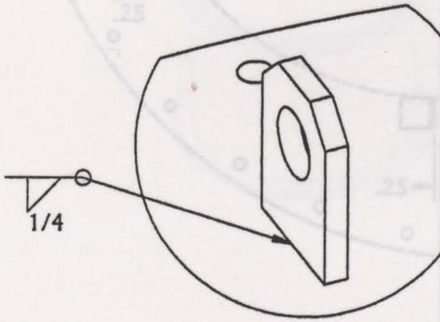

DETAIL V

PROPRIETARY AND CONFIDENTIAL

THE INFORMATION CONTAINED IN THIS DRAWING IS THE SOLE PROPERTY OF THE UNIVERSITY OF VICTORIA. ANY REPRODUCTION IN PART OR AS A WHOLE WITHOUT THE WRITTEN PERMISSION OF THE UNIVERSITY OF VICTORIA IS PROHIBITED.

UNLESS OTHERWISE SPECIFIED:		DATE	NAME	Crystal Growth
DIMENSIONS ARE IN INCHES TOLERANCES: FRACTIONAL± ANGULAR: MACH± BEND ± TWO PLACE DECIMAL ± 0.01 THREE PLACE DECIMAL ± 0.001	DRAWN	06/10/02	RM	TITLE: Superconducting Magnet-- Lifting Bracket Welds on Top Lid
	CHECKED			
	ENG APPR.			
	MFG APPR.			
INTERPRET GEOMETRIC TOLERANCING PER:	Q.A.			
MATERIAL 304 SS	COMMENTS:			DWG. NO. SM-04C
FINISH				REV
				WEIGHT:

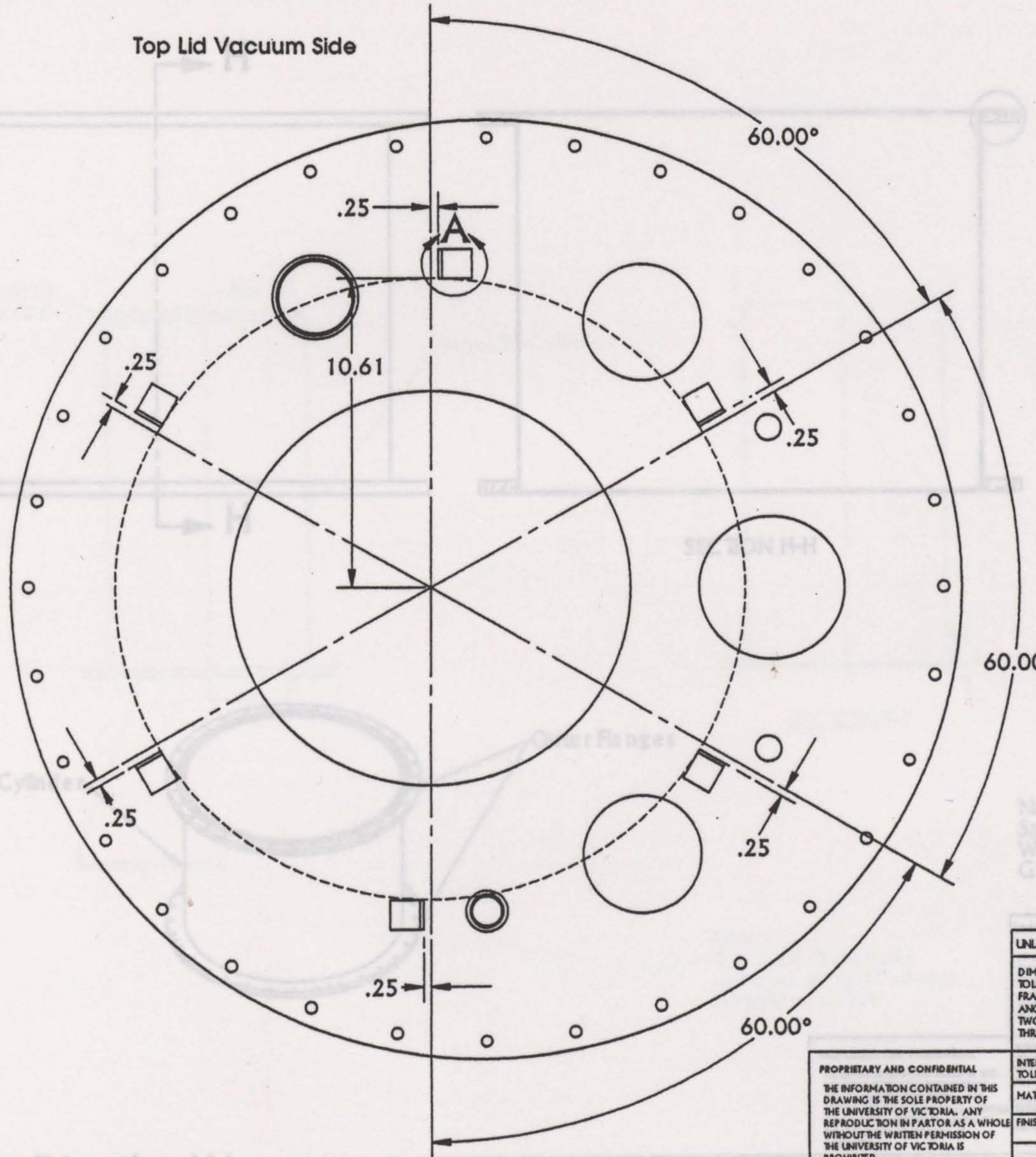

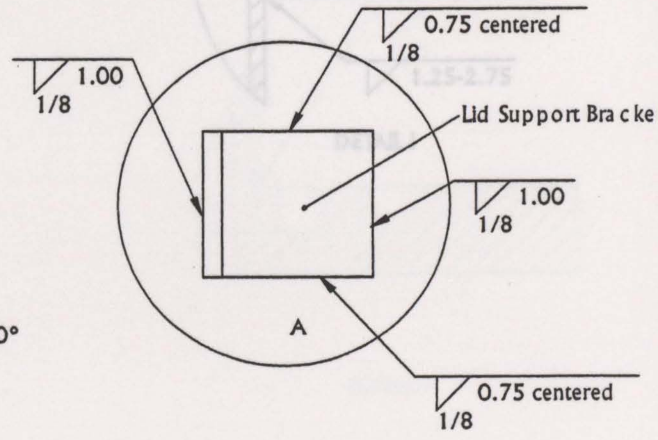

Notes:
Fillet Weld 6 brackets to vacuum side of Top Lid as noted.

UNLESS OTHERWISE SPECIFIED:		DATE	NAME	Crystal Growth
DIMENSIONS ARE IN INCHES TOLERANCES: FRACTIONAL± ANGULAR: MACH± BEND ± TWO PLACE DECIMAL ± 0.01 THREE PLACE DECIMAL ± 0.001	DRAWN	06/10/02	RM	TITLE: Superconducting Magnet-- Lid Support Bracket Welds on Vacuum Side of Top Lid
	CHECKED			
	ENG APPR.			
	MFG APPR.			
INTERPRET GEOMETRIC TOLERANCING PER:	Q.A.			
MATERIAL 304 SS	COMMENTS:			DWG. NO. SM-04D
FINISH				REV
				WEIGHT:

PROPRIETARY AND CONFIDENTIAL

THE INFORMATION CONTAINED IN THIS DRAWING IS THE SOLE PROPERTY OF THE UNIVERSITY OF VICTORIA. ANY REPRODUCTION IN PART OR AS A WHOLE WITHOUT THE WRITTEN PERMISSION OF THE UNIVERSITY OF VICTORIA IS PROHIBITED.

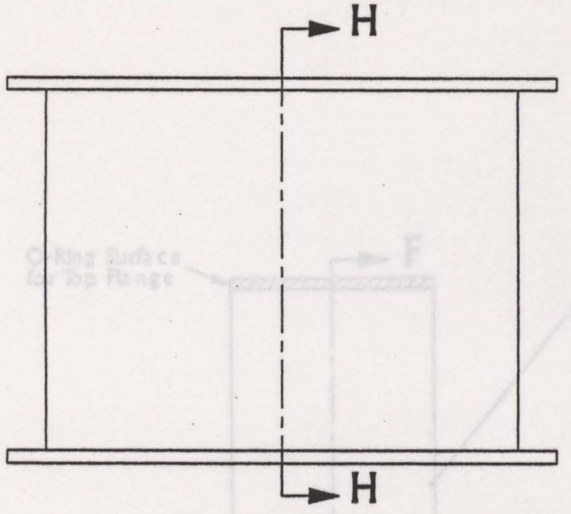

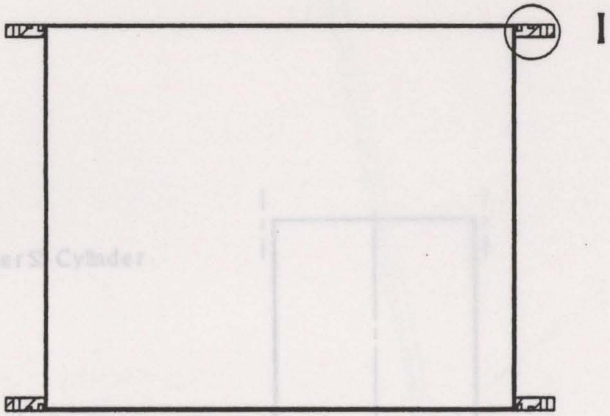

SECTION H-H

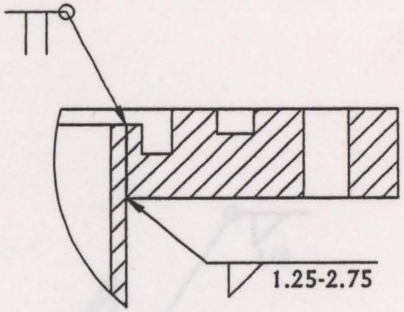

DETAIL I

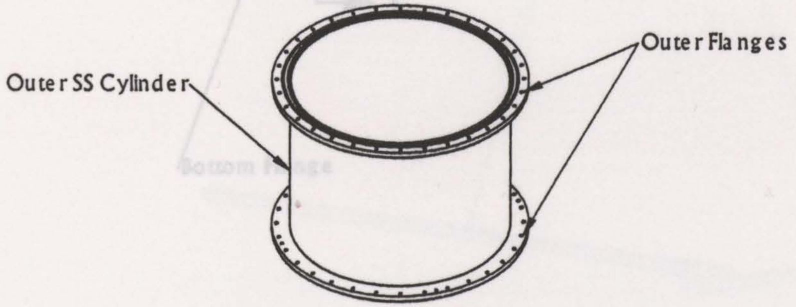

Notes:
Same weld on top and bottom flanges.
Welds must seal vacuum of 1x10^-6 Torr.
GMAW or GTAW.

UNLESS OTHERWISE SPECIFIED:
DIMENSIONS ARE IN INCHES
TOLERANCES:
FRACTIONAL±
ANGULAR: MACH± BEND ±
TWO PLACE DECIMAL ±0.01
THREE PLACE DECIMAL ±0.001
INTERPRET GEOMETRIC TOLERANCING PER:
MATERIAL 304 SS
FINISH

	DATE	NAME
DRAWN	06/10/02	RM
CHECKED		
ENG APPR.		
MFG APPR.		
Q.A.		

COMMENTS:

Crystal Growth

TITLE: Superconducting Magnet--
Outer Cyliner and Flange Welds

DWG. NO.
SM-07D

REV

WEIGHT:

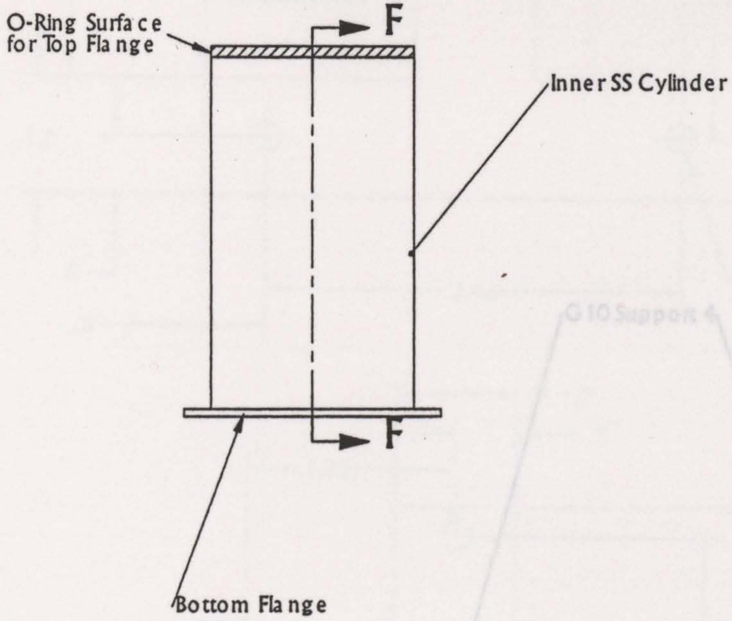

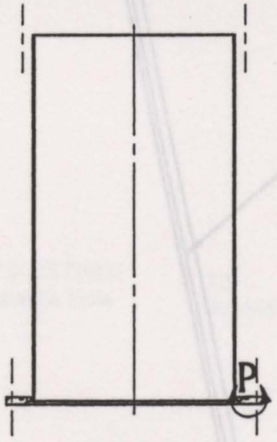

SECTION F-F

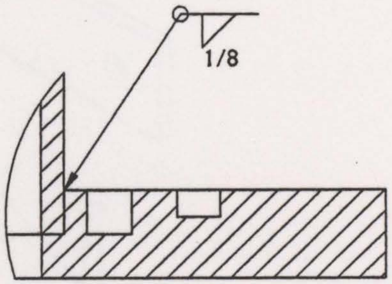

DETAIL P

Notes:
The weld must hold vacuum of 1x10^-6 torr.
GMAW or GTAW

UNLESS OTHERWISE SPECIFIED:		DATE	NAME	Crystal Growth
DIMENSIONS ARE IN INCHES TOLERANCES: FRACTIONAL± ANGULAR: MACH± BEND ± TWO PLACE DECIMAL ±0.01 THREE PLACE DECIMAL ±0.001	DRAWN	06/10/02	RM	TITLE: Superconducting Magnet-- Inner SS Cylinder and Bottom Flange Weld
	CHECKED			
	ENG APPR.			
	MFG APPR.			
INTERPRET GEOMETRIC TOLERANCING PER:	Q.A.			
MATERIAL 304 SS	COMMENTS:			DWG. NO. SM-10D
FINISH				REV
				WEIGHT:

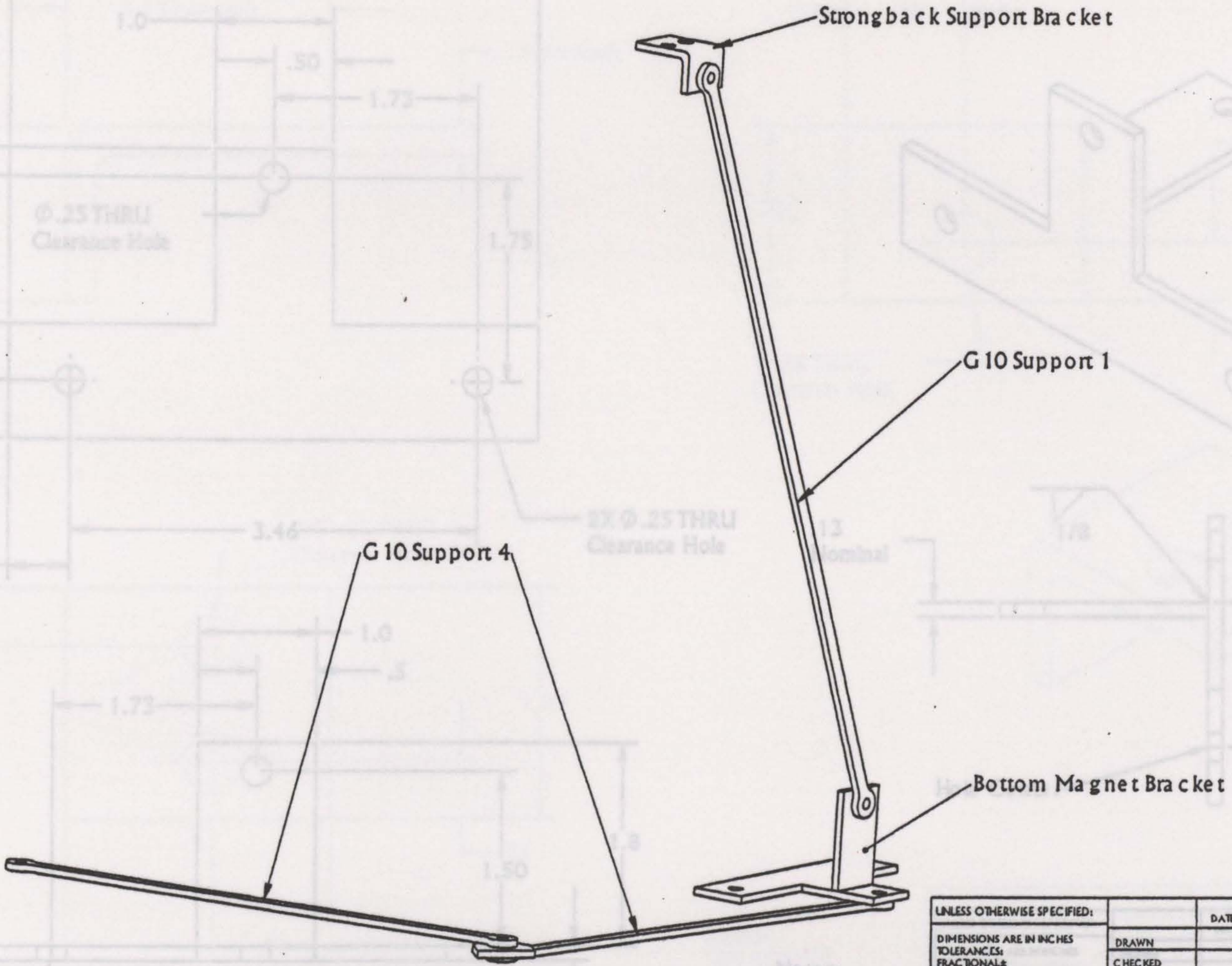

UNLESS OTHERWISE SPECIFIED:		DATE	NAME	Crystal Growth
DIMENSIONS ARE IN INCHES TOLERANCES: FRACTIONAL± ANGULAR: MACH± BEND ± ONE PLACE DECIMAL ±0.03 TWO PLACE DECIMAL ± 0.01 THREE PLACE DECIMAL ± 0.001	DRAWN		RM	TITLE: Superconducting Magnet-- Magnet Support Assembly
	CHECKED			
	ENG APPR.			
	MFG APPR.			
INTERPRET GEOMETRIC TOLERANCING PER:	Q.A.			
MATERIAL	COMMENTS:			DWG. NO. SM-15A REV
FINISH				WEIGHT:

PROPRIETARY AND CONFIDENTIAL

THE INFORMATION CONTAINED IN THIS DRAWING IS THE SOLE PROPERTY OF THE UNIVERSITY OF VICTORIA. ANY REPRODUCTION IN PART OR AS A WHOLE WITHOUT THE WRITTEN PERMISSION OF THE UNIVERSITY OF VICTORIA IS PROHIBITED.

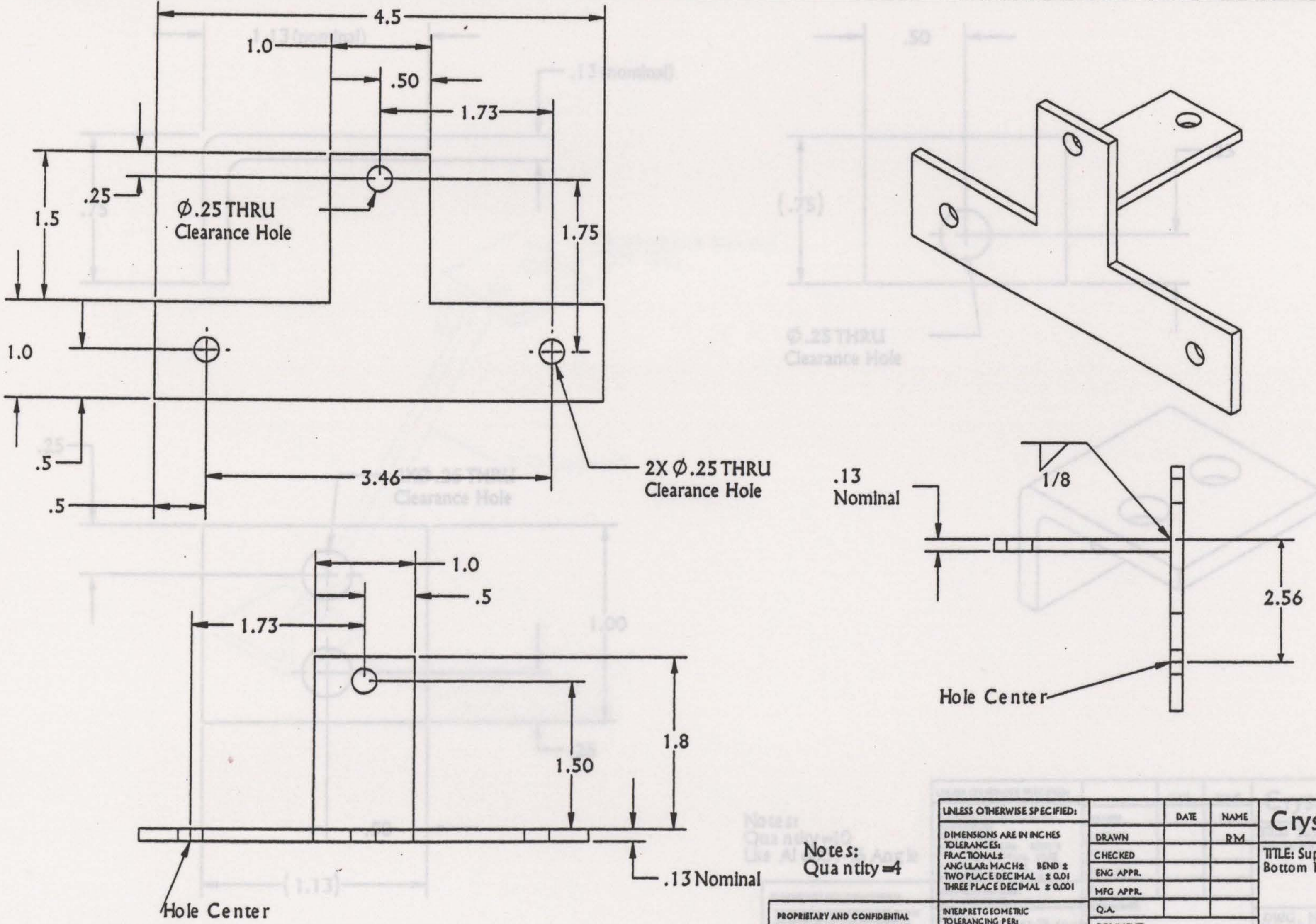

Notes:
Quantity=4

PROPRIETARY AND CONFIDENTIAL

THE INFORMATION CONTAINED IN THIS DRAWING IS THE SOLE PROPERTY OF THE UNIVERSITY OF VICTORIA. ANY REPRODUCTION IN PART OR AS A WHOLE WITHOUT THE WRITTEN PERMISSION OF THE UNIVERSITY OF VICTORIA IS PROHIBITED.

UNLESS OTHERWISE SPECIFIED:
DIMENSIONS ARE IN INCHES
TOLERANCES:
FRACTIONAL±
ANGULAR: MACH± BEND ±
TWO PLACE DECIMAL ± 0.01
THREE PLACE DECIMAL ± 0.001
INTERPRET GEOMETRIC TOLERANCING PER:
MATERIAL Al 6061-T6
FINISH

	DATE	NAME
DRAWN		RM
CHECKED		
ENG APPR.		
MFG APPR.		
Q.A.		

COMMENTS:

Crystal Growth

TITLE: Superconducting Magnet--
Bottom Magnet Bracket

DWG. NO.
SM-15B

REV

WEIGHT:

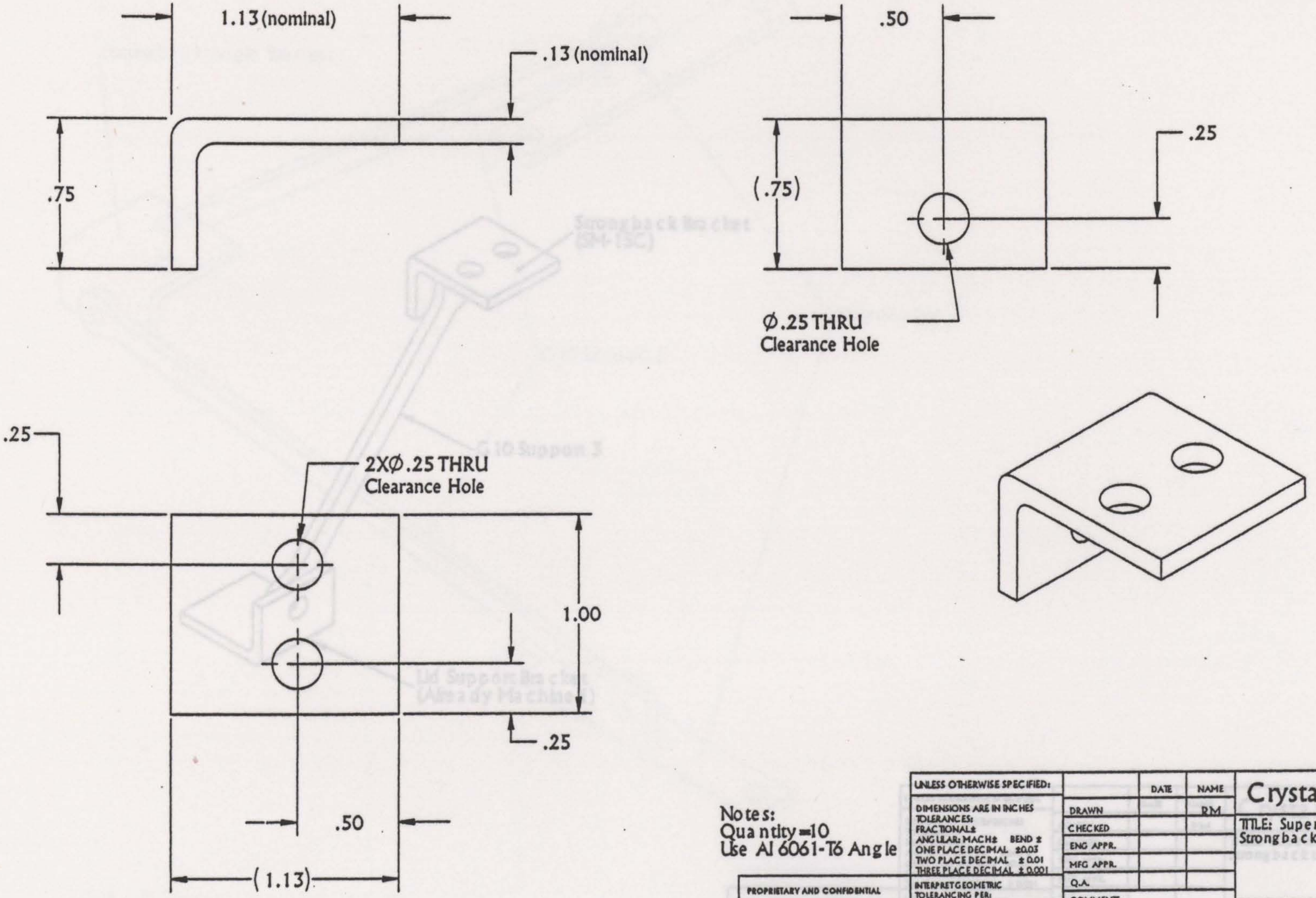

Notes:
Quantity =10
Use Al 6061-T6 Angle

UNLESS OTHERWISE SPECIFIED:		DATE	NAME
DIMENSIONS ARE IN INCHES TOLERANCES: FRACTIONAL± ANGULAR: MACH± BEND ± ONE PLACE DECIMAL ±0.03 TWO PLACE DECIMAL ± 0.01 THREE PLACE DECIMAL ± 0.001	DRAWN		RM
	CHECKED		
	ENG APPR.		
	MFG APPR.		
INTERPRET GEOMETRIC TOLERANCING PER:	Q.A.		
MATERIAL Al 6061-T6 Angle	COMMENTS:		
FINISH			

PROPRIETARY AND CONFIDENTIAL

THE INFORMATION CONTAINED IN THIS DRAWING IS THE SOLE PROPERTY OF THE UNIVERSITY OF VICTORIA. ANY REPRODUCTION IN PART OR AS A WHOLE WITHOUT THE WRITTEN PERMISSION OF THE UNIVERSITY OF VICTORIA IS PROHIBITED.

Crystal Growth

TITLE: Superconducting Magnet--Strongback Bracket

DWG. NO. SM-15C

REV

WEIGHT:

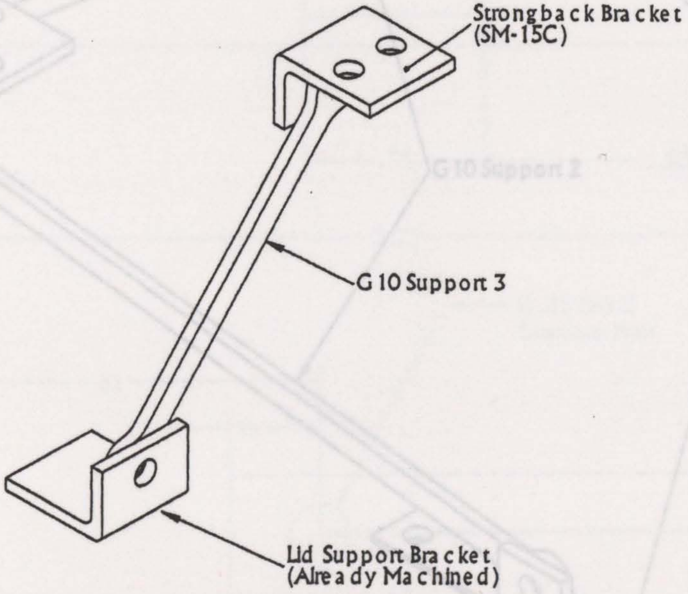

UNLESS OTHERWISE SPECIFIED:		DATE	NAME
DIMENSIONS ARE IN INCHES TOLERANCES: FRACTIONAL± ANGULAR: MACH± BEND ± ONE PLACE DECIMAL ±0.03 TWO PLACE DECIMAL ± 0.01 THREE PLACE DECIMAL ± 0.001	DRAWN		RM
	CHECKED		
	ENG APPR.		
	MFG APPR.		
INTERPRET GEOMETRIC TOLERANCING PER:	Q.A.		
MATERIAL	COMMENTS:		
FINISH			

PROPRIETARY AND CONFIDENTIAL

THE INFORMATION CONTAINED IN THIS DRAWING IS THE SOLE PROPERTY OF THE UNIVERSITY OF VICTORIA. ANY REPRODUCTION IN PART OR AS A WHOLE WITHOUT THE WRITTEN PERMISSION OF THE UNIVERSITY OF VICTORIA IS PROHIBITED.

Crystal Growth

TITLE: Superconducting Magnet--
Strongback to Lid Support Assembly

DWG. NO.
SM-16A

REV

WEIGHT:

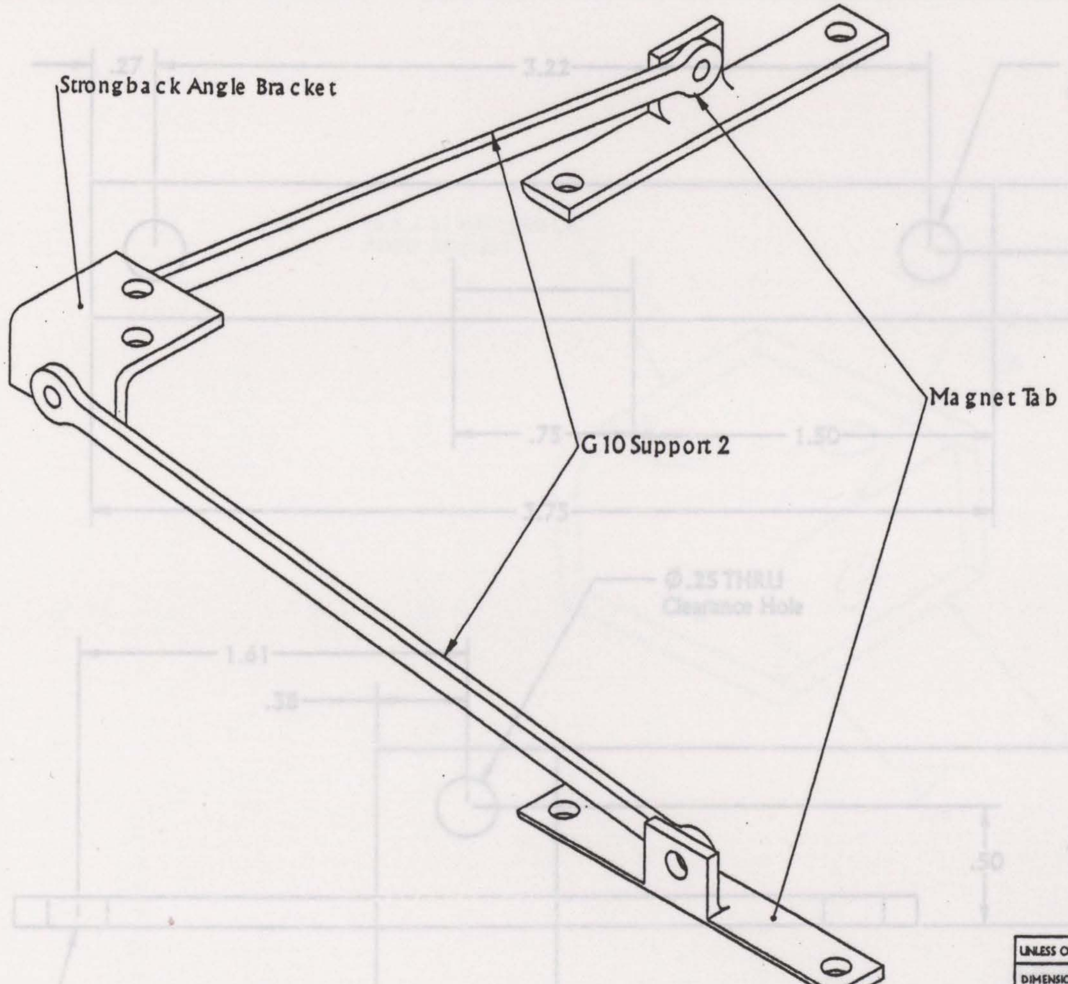

UNLESS OTHERWISE SPECIFIED:		DATE	NAME	Crystal Growth
DIMENSIONS ARE IN INCHES TOLERANCES: FRACTIONAL± ANGULAR: MACH± BEND ± ONE PLACE DECIMAL ±0.03 TWO PLACE DECIMAL ± 0.01 THREE PLACE DECIMAL ± 0.001	DRAWN		RM	TITLE: Superconducting Magnet-- Magnet Top Support
	CHECKED			
	ENG APPR.			
	MFG APPR.			
INTERPRET GEOMETRIC TOLERANCING PER:	Q.A.			
MATERIAL	COMMENTS:			DWG. NO. SM-17A
FINISH				REV
				WEIGHT:

PROPRIETARY AND CONFIDENTIAL

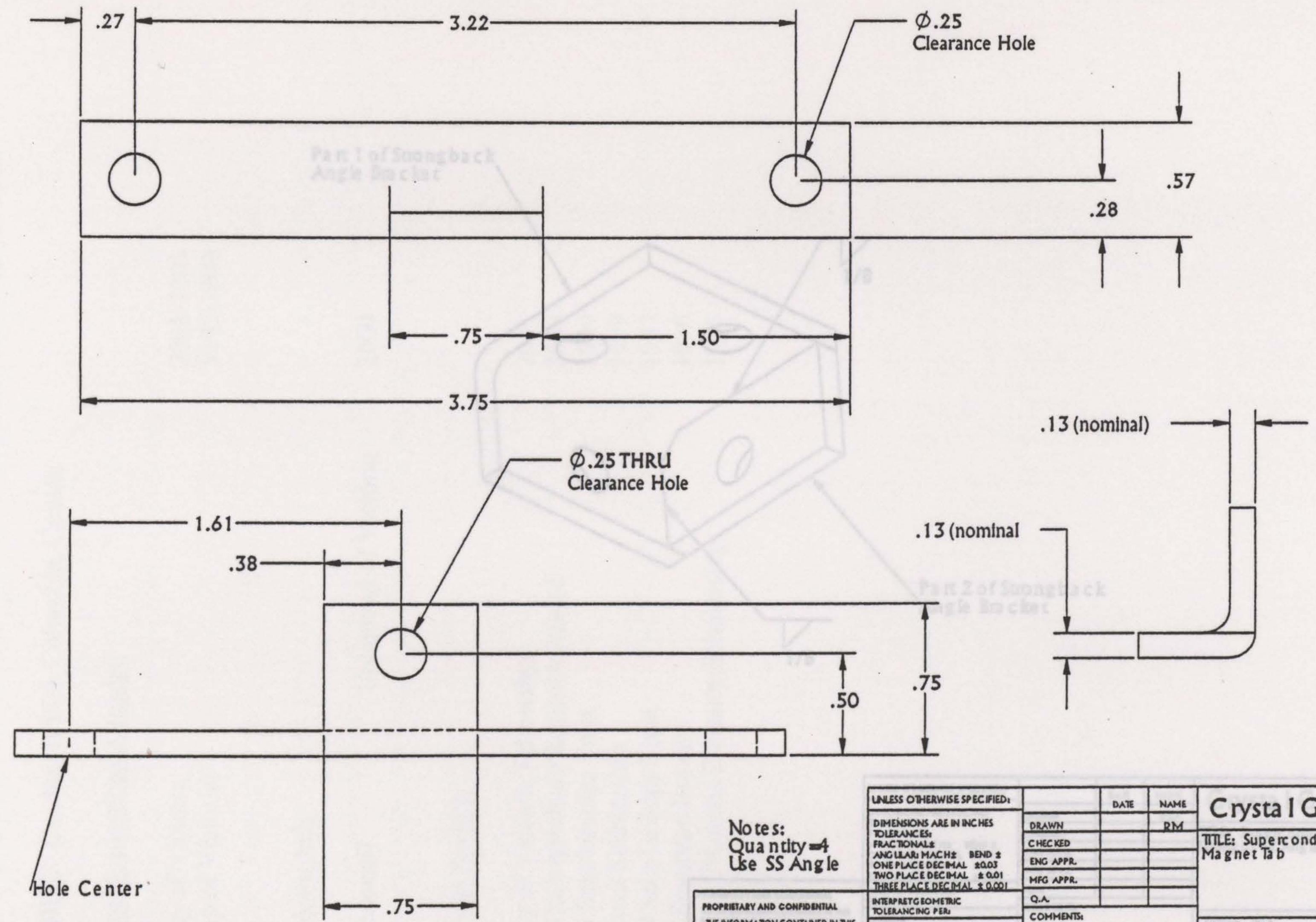

Notes:
Quantity=4
Use SS Angle

		DATE	NAME
UNLESS OTHERWISE SPECIFIED:			
DIMENSIONS ARE IN INCHES TOLERANCES: FRACTIONAL± ANGULAR: MACH± BEND ± ONE PLACE DECIMAL ±0.03 TWO PLACE DECIMAL ±0.01 THREE PLACE DECIMAL ±0.001	DRAWN		RM
	CHECKED		
	ENG APPR.		
	MFG APPR.		
INTERPRET GEOMETRIC TOLERANCING PER:	Q.A.		
MATERIAL 6061-T6 Al	COMMENTS:		
FINISH			

PROPRIETARY AND CONFIDENTIAL

THE INFORMATION CONTAINED IN THIS DRAWING IS THE SOLE PROPERTY OF THE UNIVERSITY OF VICTORIA. ANY REPRODUCTION IN PART OR AS A WHOLE WITHOUT THE WRITTEN PERMISSION OF THE UNIVERSITY OF VICTORIA IS PROHIBITED.

Crystal Growth

TITLE: Superconducting Magnet--Magnet Tab

DWG. NO.
SM-17B

REV

WEIGHT:

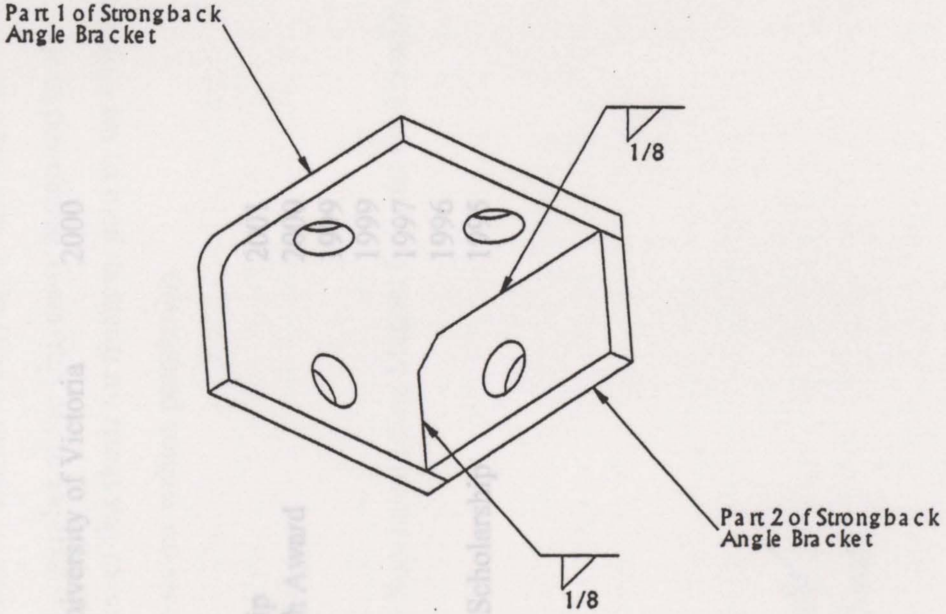

PROPRIETARY AND CONFIDENTIAL

THE INFORMATION CONTAINED IN THIS DRAWING IS THE SOLE PROPERTY OF THE UNIVERSITY OF VICTORIA. ANY REPRODUCTION IN PART OR AS A WHOLE WITHOUT THE WRITTEN PERMISSION OF THE UNIVERSITY OF VICTORIA IS PROHIBITED.

UNLESS OTHERWISE SPECIFIED:
DIMENSIONS ARE IN INCHES
TOLERANCES:
FRACTIONAL±
ANGULAR: MACH± BEND ±
ONE PLACE DECIMAL ±0.03
TWO PLACE DECIMAL ± 0.01
THREE PLACE DECIMAL ± 0.001

INTERPRET GEOMETRIC TOLERANCING PER:

MATERIAL

FINISH

	DATE	NAME
DRAWN		RM
CHECKED		
ENG APPR.		
MFG APPR.		
Q.A.		

COMMENTS:

Crystal Growth

TITLE: Superconducting Magnet--Strongback Angle Bracket Assembly

DWG. NO.
SM-17C

REV

WEIGHT:

VITA

Surname: McDonald Given Names: Robbi Lynn

Place of Birth: Creston, British Columbia, Canada

Educational Institutions Attended

University of Victoria	2001-2003
University of Victoria	1995-2000

Degrees Awarded:

B.Sc. (Honours)	University of Victoria	2000

Honours and Awards

University of Victoria Fellowship	2001
NSERC Undergraduate Research Award	2000
PISAPIO Scholarships Trust	1999
Woods Trust Scholarship	1999
PISAPIO Scholarships Trust	1997
The Jane Seaborne Bursary	1996
University of Victoria Entrance Scholarship	1995

Title of Thesis:

Design and Analysis of a Superconducting Magnet Cryostat for Traveling Heater Method Growth of CdZnTe

Author [redacted]

Robbi Lynn McDonald

April 10, 2000

9 References

[1] Crowle, M.R. Equipment Designed for the Growth of CdZnTe Crystals by the Traveling Heater Method Under the Influences of Static and Rotating Magnetic Fields. MASc Thesis, Mechanical Engineering, University of Victoria, 2002.

[2] Senchenkov, A.S., Barmin, I.V., Tomson, A.S., Krapukhin, V.V. Seedless THM growth of $Cd_xHg_{1-x}Te$ (x~0.2) Single Crystals within Rotating Magnetic Field. Journal of Crystal Growth, Vol 197, No. 3, 1999. pp. 552-6.

[3] Barmin, I.V., Egorov, A.V., Senchenkov, A.S. Results of Crystal Growth Experiments by FZM on Zona Facilities in Microgravity. Proceedings VIIIth European Symposium on Materials and Fluid Sciences in Microgravity, Brussels, Belguim, 12-16 April 1992. p. 591.

[4] Barmin, I.V., Senchenkov, A.S. Technological Equipment of SPLAV Technical Center for Producing Materials in Space. Some Results of the Experiments on Crystal Growth. Microgravity Q., Vol. 3, No. 2-4, 1993. pp. 233-239.

[5] Benz, K.W., Dold, P., Croll, A., Schweizer, M., Kaiser, Th., Lichtensteiger, M., Szofran, F.R. Comparison of the Effect of Microgravity and Magnetic Fields on the Crystal Growth of Floating Zone Silicon. SPIE Conference on Materials Research in Low Gravity II, Denver, Colorado, July 1999. SPEI Vol. 3792.

[6] Sheibani, H., Sakai, S., Dost, S., Lent, B. LPEE Growth of Binary and Ternary Crystals Under Applied Magnetic Field-Experimental. The 13th International Symposium on Transport Phenomena, Victoria, B.C. July 14-18, 2002. pp. 599.

[7] Dost, S., Qin, Z. A Model for Liquid Phase Electroepitaxy Under an External Magnetic Field, I. Theory. Journal of Crystal Growth Vol. 153, 1995. pp. 123-130.

[8] Dost, S. Numerical Simulation of Liquid Phase Electroepitaxial Growth of GaInAs Under Magnetic Field. ARI Vol 51, 1999. pp. 235-246.

[9] Dost, S., Liu, Y., Lent, B., Redden, R.F. A Numerical Simulation Study for the Effect of Applied Magnetic Field in Growth of CdTe single Crystals by the Traveling Heater Method. International Journal of Applied Electromagnetics and Mechanics, 2003. In Press.

[10] Salk, M., Fiederle, M., Benz, K.W., Senchenkov, A.S., Egorov, A.V., Matiuokhin, D.G. CdTe and CdTe0.9Se0.1 Crystals Grown by the Travelling Heater Method Using a Rotating Magnetic Field. Journal of Crystal Growth, Vol. 138, 1994. pp. 161-167.

[11] Gelfgat, Y., Krumin, J., Abricka, M. Application of Combined Electromagnetic Fields for Controlling the Hydrodynamics and Heat/Mass Transfer in the Processes of Bulk Single Crystal Growth. Third International Conference on Crystal Growth, Strength Problems and Heat Mass Transfer, (ICSC99), Obninsk, Russia, Sept 21-24, 1999. Abstracts p. 201.

[12] Liu, Y.C., Okano, Y., Dost, S. The Effect of Applied Magnetic Field on Flow Structures in Liquid Phase Electroepitaxy – A Three-Dimensional Simulation Model. Journal of Crystal Growth, Vol. 244, 2002. pp. 12-26.

[13] Sheibani, H., Liu, Y., Sakai, S., Lent, B., Dost, S. The Effect of Applied Magnetic Field on the Growth Mechanisms of Liquid Phase Electroepitaxy. International Journal of Engineering Science, Vol. 41, 2003. pp. 401-415.

[14] Montgomery, D.B. Solenoid Magnet Design, The Magnetic and Mechanical Aspects of Resistive and Superconducting Systems. John Wiley & Sons, Inc., New York. 1969.

[15] American Magnetics, Inc. P.O. Box 2509, 112 Flint Road, Oak Ridge, TN 37831-2509. Phone: (865) 482-1056, Fax: (865) 482-5472. http://www.americanmagnetics.com

[16] Janis Research Company, Inc. No. 2 Jewel Drive, P.O. Box 696, Wilmington, MA 01887-0696. TEL: (978) 657-8750, FAX: (978) 658-0349 http://www.janis.com/p-cfms.html

[17] CRYO Industries of America, Inc., 11124 S. Willow Street, Manchester, NH 03103 Tel: (603) 621-9957, Fax: (603) 621-9960 http://www.cryoindustries.com/magsys.htm

[18] Burgoyne, J.W., Daniels, P.D., Timms, K.W., Vale, S.H. Advances in Superconducting Mangets for Commercial and Industrial Applications. IEEE Transactions on Applied Superconductivity, Vol. 10, No. 1, March 2000. pp. 703.

[19] Cooper, T.L., Walters, J.D., Fikse, T.H. Thermal Conductance of Heat Transfer Interfaces for Conductively Cooled Superconducting Magnets. Advances in Cryogenic Engineering, Vol. 41. Plenum Press, NY. (1996). Pp. 297-304.

[20] Hasebe, T. et al. Cryocooler Cooled Superconducting Magnets and their Applications. Advances in Cryogenic Engineering, Vol. 43. Plenum Press, NY. 1998. 291-297.

[21] Hata, F., Sakuraba, J., Chong, C.K., Yamada, Y., Hasebe, T., Ishihara, M., and Watanabe, K. A Conduction Cooled Superconducting Magnet Using High-Tc Oxide Current Leads. MT-13 Conference, (Victoria sept.93)

[22] Kuriyama, T. *et al.* Cryocooler Directly Cooled 6 T NbTi Superconducting Magnet System with 180 mm Room Temperature Bore. Cryogenics, Vol 34. ICEC Supplement. 1994.

[23] Masuyama, S. Yamamoto, H., Matsubara, Y. A NbTi Split Magnet Directly Cooled by a Cryocooler. IEEE Transactions on Applie Superconductivity, Vol. 3, No. 1 March 1993. pp. 262,

[24] Obasih, K.M. and Mruzek, M.T. Thermal Design and Analysis of a Cryogenless Superconducting Magnet for Interventional MRI Therapy. Advances in Cryogenic Engineering, Vol. 41. Plenum Press, NY. (1996) pp. 305-311.

[25] Rowe, A., Barclay, J.A., Dost, S. Design of an Apparatus for a 5T Conduction Cooled NbTi Solenoid with a 203 mm Room Temperature Bore. Advances in Cryogenic Engineering, Vol 45. Plenum Publishers, 2000. pp. 651-658.

[26] Shibutani, K. et al. Development of Two Types of Cryogen Free Superconducting Magnet. Advances in Cryogenic Engineering, Vol. 43. 1998. pp. 299-305.

[27] Snitchler, G., Kalsi, S.S., Manlief, M., Schwall, R.E., Sidid-Yekhlef, A., Ige, W., Medeiros, R. High-Field Warm-Bore HTS Conduction Cooled Magnet. Invited Talk at 1998 Applied Superconductivity Conference. Desert Springs, CA, September 1998.

[28] Song, N.H. et al. A Cryocooler Directly Cooled 5 Tesla Niobium Titanium Superconducting Magnet System. Advances in Cryogenic Engineering, vol 45. Kluwer Academic/Plenum Publishers (2000). pp. 667-674.

[29] Takahashi, H. et al. A 7.7 T NbTi Superconducting Magnet System Cooled by a 4 K GM Refrigerator. Advances in Cryogenic Engineering. Vol. 39. Plenum Press, NY. (1994) pp. 343-350.

[30] van Oort, J.M. et al. A Cryogen-Free 0.5 Tesla MRI Magnet for Head Imaging. Advances in Cryogenic Engineering, Vol. 43. Plenum Press, NY. (1998) pp. 139-147.

[31] Squires, B. et al. Design of the 2 Tesla Superconducting Solenoid for the Fermilab D0 Detector Upgrade. Advances in Cryogenic Engineering. Vol 39. Plenum Press, NY. (1994). Pp. 301-308.

[32] Chang, H., Kim, H. Development of a Thermal Switch for Faster Cool-Down by Two-Stage Cryocooler. Cryogenics, Vol. 40, 2000. pp. 769-777.

[33] RDK-415 Sumitomo (SHI) 4 K Refrigerator, Janis Research Company, Inc. 2 Jewel Drive, P.O. Box 696, Wilmington, MA 01887-0696. TEL: (978) 657-8750,
FAX: (978) 658-0349
http://www.janis.com/p-a4k11.html

[34] ASME Boiler and Pressure Vessel Code, Section VIII, Rules for Construction of Pressure Vessels, Division 1. 1992 Edition, July 1, 1992.

[35] Bednar, H.H. Pressure Vessel Design Handbook. Van Nostrand Reinhold Company, New York, 1981.

[36] Young, W.C. Roark's Formulas for Stress & Strain, Sixth Edition. McGraw-Hill Inc. 1989.

[37] Flynn, T.M. Cryogenic Engineering. Marcel Dekker, Inc., 1997.

[38] inPHormTM O-Rings, Version 2.0.2. Parker Seals, 1994-1999. Parker Hannifin Corporation, Cleveland, Ohio.
http://www.parker.com/inphorminfo/

[39] Simrit – North American Headquarters, 47690 East Anchor Court, Plymouth, MI 48170, Phone:(866) 2-SIMRIT, Fax: (734) 354-5500
http://www.simritna.com/catalog/o-ring/991applications.htm

[40] Apple Rubber, 1.800.828.7745 (US and Canada Only), Tel: 716.684.6560, Fax: 716.684.8302.
http://www.applerubber.com

[41] Weisend II, J.G. Handbook of Cryogenic Engineering. Taylor and Francis, 1998.

[42] Marquardt, E.D., Le, J.P., Radebaugh, R. Cryogenic Material Properties Database. National Institute of Standards and Technology. 11th International Cryocooler Conference. June, 2000.

[43] GE Polymershapes Thermoset Industrial Laminate Properties, Minimum Values. 3917 Grant Street, Burnaby, BC V5C 3N4, Phone: 604-298-1945, Fax: 604-298-1941
http://www.gepolymershapes.com

[44] Kasen, M.B., MacDonald, G.R., Beekman, D.H.Jr, Schramm, R.E. Mechanical,Electrical, and Thermal Characterization of G-10CR and G-11CR Glass-Cloth/Epoxy Laminates Between Room Temperature and 4 K. Advances in Cryogenic Engineering, Materials. Vol. 26, 1980. pp. 235.

[45] Lewis, W., Samuel, A. Fundamentals of Engineering Design. Prentice Hall, 1989.

[46] Shigley, J.E., Mischke, C.R. Fastening, Joining, and Connecting, A Mechanical Designers' Workbook. McGraw-Hill Publishing Company, 1990.

[47] Megyesy, E.F. Pressure Vessel Handbook, Eighth Edition. Pressure Vessel Handbook Publishing, Inc. 1989.

[48] Mumford, F.J. Superconducting Current-Leads made from High Tc Superconductor and Normal Metal Conductor. Cryogenics, Vol. 29, 1989. pp. 206.

[49]Bogdanov, I., Kozub, S., Myznikov, K et.al. Application of HTS BI-2223 For Current Leads of Superconducting Magnets. Proceedings of EPAC 2000, Vienna, Austira.

[50]Chang, H., VanSciver, S.W. Thermodynamic Optimization of conduction-Cooled HTS Current Leads. Cryogenics, Vol. 38, 1998. pp. 729-736.

[51] Herrmann, P.F., Cottevieille, C., Duperray, G., Leriche, A., Verhaege, T., Albercht, C., Bock, J. Cryogenic Load Calculation of High Tc Current Lead. Cryogenics, Vol 33, 1993. pp. 555.

[52] Daugherty, M.A., Daney, D.E., Prenger, F.C., Hill, D.D., Williams, P.M., Boenig, H.J. Assembly and Testing of a Composite Heat Pipe Thermal Intercept for HTS Current Leads. Advances in Cryogenic Engineering, Vo. 41, 1996. pp. 579.

[53] Lock, J.M. Optimization of Current Leads into a Cryostat. Cryog. 9, 1969. pp. 438

[54] Jones, M.C., Yeroshenko, V.M., Strostin, A., Yaskin, L.A. Transient Behaviour or Helium-Cooled Current Leads for Superconducting Power Transmission. Cryog.. 18, 1978. pp. 337

[55] Powell, R.L., Roder, H.M., Rogers, W.M. Low-Temperature Thermal Conductivity of Some Commercial Coppers. J. Applied Physics. Vol 28, No. 11, 1957. pp. 1282

[56] Maehata, K., Ishibashi, K., Wakuta, Y. Design Chart of Gas-Cooled Current Leads Made of Copper of Different RRR Values. Cryogenics, Vol. 34, 1994. pp. 935.

[57] Smith, C.O. The Science of Engineering Materials. Third Edition. Prentice-Hall, Inc., 1986. pp. 554.

[58] McFee, R. Optimum Input Leads for Cryogenic Apparatus. The Rev. Sci. Inst. Vol. 30 1959. pp. 98.

[59] Powell, R.L., Coffin, D.O. Low-Temperature Thermal Conductivity of a Free-Machining Copper. Rev. Sci. Instr. Vol. 26, 1955. pp. 516

[60] Dauphinee, T.M., Preston-Thomas, H. A Copper Resistance Temperature Scale. Rev. Sci. Instr. Vol 25, #9, 1954. pp. 884

[61] American Superconductor CryoSaver^{TM} Current Leads, Two Technology Drive Westborough, MA. 01581.
www.amsuper.com

[62] Farahat, M.A. Gockenbach, E., El-Alaily, A.A., Abdel Aziz, M.M. Effect of Coating Materials on the Electrical Performance of Copper Joints. Proceedings of the 42nd IEEE Holm Conference on Electrical Contacts, 1996. pp. 472.

[63] Timsit, R.S. Electrical Contact Resistance: Properties of Stationary Interfaces. IEEE Trans. on Components and Packaging Technology, Vol. 22, No. 1, 1999. pp. 85.

[64] Nilles, M.J., Van Sciver, S.W. Effects of Oxidation and Roughness on Cu Contact Resistance from 4 K to 290 K. Advances in Cryogenic Engineering, Vol. 34, 1988. pp. 443.

[65] Sato, K., Okumura, H., Yamaguchi, S. Numerical Calculations for Peltier Current Lead Designing. Cryogenics, Vol, 41, 2001. pp. 497.

[66] Xuan, X.C., Ng, K.C., Yap, C., Chua, H.T. Optimization and Thermodynamic Understanding of Conduction-Cooled Peltier Current Leads. Cryogenics, Vol 42, 2002. pp.141.

[67] Barron, R.F. Cryogenic Heat Transfer. Taylor & Francis, 1999.

[68] Metallized Products, Inc. 37 East St., Winchester, MA 01890
Phone: 781.729.8300

[69] Eyssa, Y.M., Okasha, O. Thermodynamic Optimizaton of Thermal Radiation Shields for a Cryogenic Apparatus. Cryogenics, Vol 18, no. 5, 1978. pp. 304-307.

[70] Scurlock, R.G., Saull, B. Development of Multilayer Insulations with Thermal Conductivities Below 0.1 μW cm^{-1}K^{-1}. Cryogenics. May 1976. pp. 303.

[71] Kumar, A.S., Murthy, M.V.K., Jacob, S., Kasthurirengan, S. Thermal Performance of Multilayer Insulation Down to 4.2 K. Advances in Cryogenic Engineering, Vol. 45, 2000. pp. 1675.

[72] Leung, E.M.W., Fast, R.W., Hart, H.L., Heim, J.R. Techniques for Reducing Radiation Heat Transfer Between 77 and 4.2 K. Advances in Cryogenic Engineering, Vol 25, 1980. pp. 489-499.

[73] Spradley, I.E., Nast, T.C., Frank, D.J. Experimental Studies of MLI Systems at Very Low Boundary Temperatures. Advances in Cryogenic Engineering, Vol 35, 1990. pp. 477-486.

[74] Zeller, A.F., DeKamp, J.C., Leung, E.M.W., Fast, R.W. Long Term Results from the Elimination of MLI Between 4 and 77 K. Advances in Cryogenic Engineering, Vol 39, 1994. pp. 1691-1697.

[75] World of Tape Ltd. 11191 Horseshoe Way, Unit 9, Richmond, B.C., Tel: 1-888-272-6898, Fax: 604-272-4552.
www.worldoftape.com

[76] RDK-415 Load Map, Janis Research Company, Inc. 2 Jewel Drive, P.O. Box 696 Wilmington, MA 01887-0696. TEL: (978) 657-8750 FAX: (978) 658-0349
http://www.janis.com/p-a4k11.html

[77] Assemblage Paro Inc., 495, de l'Aviation,Cap-de-la-Madeleine (Québec)G8T 5M4 Canada. Tél.: (819) 375-3503 Fax: (819) 373-2448

[78] Holm, R., Holm, E. Electric Contacts, Theory and Application. Fourth Edition. Springer-Verlag New York Inc., 1967.

[79] Berman, R. Some Experiments on Thermal Contact at Low Temperatures. Journal of Applied Physics, Vol. 27, No. 4, 1956. pp. 318.

[80] Kittel, P., Salerno, L.J., Spivak, A.L. Thermal Conductance of Pressed Bi-Metallic Contacts at Liquid Nitrogen Temperatures. Presented at ICEC, Genova, Italy, June 7-10, 1994.

[81] Salerno, L.J., Kittel, P., Spivak, A.L. Thermal Conductance of Pressed Metallic Contacts Augmented with Indium Foil or Apiezon Grease at Liquid Helium Temperatures. Cryogenics, Vol. 34, 1994. pp. 649.

[82] Xu, L., Yang, J., Xu, J.M., Li, S.M., Xiong, W., Zhang,T. The Effectof Solid Interfaces on Thermal Contact Resistance at Low Temperature. Advances in Cryogenic Engineering, Vol. 43, 1998. pp. 1369.

[83] Pobell, F. Matter and Methods at Low Temperatures. Springer-Verlag, Berlin Heidelberg, 1992. pp. 71-72.

[84] Williams, B., Jensen, S., Chadek, M., Batty, J.C. Solderless Flexible Thermal Links. Cryogenics, Vol., 36, No. 10, 1996. pp. 867.

[85] Willekers, R.W., Bosch, W.A., Mathu, F., Meijer, H.C., Postma, H. Impact Welding: A Superior Method of Producing Joints with High Thermal Conductivity Between Metals at Very Low Temperatures. Cryogenics, Vol. 29, 1989. pp. 904.

[86] Incropera, F.P., DeWitt, D.P. Fundamentals of Heat and Mass Transfer, Fourth Edition. John Wiley & Sons, 1996. pp. 79-81.

[87] Holman, J.P. Heat Transfer, 8^{th} Edition. McGraw-Hill Companies, Inc., 1997. pp.56-59.

[88] Fried, E. Thermal Conduction Contribution to Heat Transfer at Contacts. R.P. Tye, Ed., Thermal Conductivity, Vol. 2, Academic Press, London, 1969. pp. 253.

[89] Circle Bolt and Nut Co., Inc. http://www.circlebolt.com/SAE%20Grade%20Clamping%20Specification.htm

[90] Lake Shore Cryotronics, Temperature Measurement and Control catalogue, 2002.

[91] National Instruments Corporation, NI 6034E/6035E/6036E User Manual, p. 1-1, A-2.

[92] National Instruments Corporation, Instrumentation Catalogue, Measurment and Automation, 1998. pp. 185.

[93] Courts, S.S., Davenport, W.E., Holmes, D.S. Thermal Resistances of Cryogenic Temperature Sensors from 1-300 K. Advances in Cryogenic Engineering, Vol. 45, 2000. pp. 1849.

Appendix-A

Weight

Table 30 has the weight of all components as they are designed. When calculating stresses due to the weight for the supports and the vacuum vessel shell, the weight was first approximated, then when the dimensions for design were selected and the actual weight was known the calculations were redone.

Component	Weight (lb)	Mass (kg)	Force (N)
Magnet	77	35	343
Extras	40	18	177
Copper Shield	50	23	226
Aluminum Strongback	17	8	78
Cryocooler	40	18	177
SS 304 Bore	34	15	147
SS 304 Outer Shell	73	33	324
SS 304 Lids (2)	238	108	1060
Outer Flanges	75	34	334
Top Inner Flange	8	4	39
Bottom Inner Flange	15	7	69
Totals			
Supported by Shell	357	162	1590
Supported by Strongback	152	69	677
Supported by Lid Supports	169	77	755
Shell	484	220	2160
Total of all components	**663**	**301**	**2950**

Table 30: Weight of superconducting magnet system components.

Appendix-B

Weld Strengths for Brackets

Welds are required on the brackets for supports 1, supports 3 and supports 4. For support 1, the Al 6061-T6 bottom magnet bracket must be welded together and for support 3 the top SS 304 brackets must be welded to the lid of the vessel. For support 4, a bracket must be welded to the inside of the stainless steel cylinder. Also, for assembly, three SS 304 brackets are welded to the outside of the lid and must be able to support the entire load of the superconducting magnet assembly of approximately 3110 N (700 lb). These welds can be examined in drawings SM-04C, SM-04D, and SM-15B in the Appendix-D.

To determine the required size of the fillet weld, the tension, shear and bending forces must be determined. The tension or compression force is given by

$$W_1 = \frac{P_w}{A_w}, \tag{41}$$

where P_w is the allowable concentrated axial load and A_w is the length of the weld. The vertical shear force is given by

$$W_s = \frac{V}{A_w}, \tag{42}$$

where V is the vertical shear. And, the bending force is given by

$$W_b = \frac{M_w}{S_w}, \tag{43}$$

where M_w is the bending moment and S_w is the section modulus of weld lines and is given by

$$S_w = \frac{{d_b}^2}{3}, \tag{44}$$

for a rectangular piece, where d_b is the width of the bracket. The resultant force is then

$$W = \sqrt{W_1 + W_s + W_b}\,. \tag{45}$$

The fillet weld size required can now be found and is given by

$$w = \frac{W}{f}, \tag{46}$$

where f is the allowable load on a weld and can be found in tables or is given by the formula

$$f = 0.707\omega 0.3S_t\,, \tag{47}$$

where ω is the leg size and S_t is the minimum tensile strength of the weld metal. For a 2.5x2.5 cm (1"x1") weld on SS 304, f is 88 MPa (12730 lb/in^2), and for a 2.5x2.5 cm weld on Al 6061-T6, f is approximately 59 MPa (8484 lb/in^2) [46]. All of the equations were taken from Megyesy [46] and Shigley [47].

The resulting minimum leg sizes are shown in Table 31. The minimum leg sizes are very small, so common weld sizes of 0.32 cm (1/8 in) and 0.64 cm (1/4 in) are used and will easily handle the required loads. Note that for the lid support brackets, a safety factor of 3 was used on the weight of the magnet vessel. Also, for supports 4, the amount of horizontal force on the cylinder bracket is unkown so the weld size was not calculated. A practical weld size of 0.32 cm (1/8 in) was chosen for support 4 bracket weld.

Support bracket	W1 (N/m)	Ws (N/m)	Wb (N/m)	f (MPa)	W (kN/m)	ω_{min} (cm)	ω (cm)
1	3370	1480	6660	59	7.53	0.0130	0.32
3	1410	977	5180	88	5.43	0.0061	0.32
lid	2540	1540	138000	88	142	0.162	0.64

Table 31: Weld leg sizes.

Appendix-C

Thermal Path Temperature Differences

Path	Area (m^2)	Length (m)	Thermal Conductivity (W/m-K)	Thermal Conductance (mW/K)	Heat load (W)	Temperature Difference (K)
cryocooler to extender				798	0.15	0.193
extender	1.46E-03	4.47E-02	320		0.15	0.015
extender to busbar				798	0.15	0.193
Total						**0.401**

Table 32: Temperature Difference Between Cryocooler and Busbar (Persistent mode)

Path	Area (m^2)	Length (m)	Thermal Conductivity (W/m-K)	Thermal Conductance (mW/K)	Heat load (W)	Temperature Difference (K)
cryocooler to extender				798	0.54	0.681
extender	1.46E-03	4.47E-02	320		0.54	0.052
extender to busbar				798	0.54	0.681
Total						**1.413**

Table 33: Temperature Difference Between Cryocooler and Busbar (Charging mode)

Path	Area (m^2)	Length (m)	Thermal Conductivity (W/m-K)	Thermal Conductance (mW/K)	Heat load (W)	Temperature Difference (K)
CuLead to Copper Block				295	0.03	0.092
Cu Block	2.26E-03	1.27E-02	320		0.03	0.000
CuBlock to Busbar				277	0.03	0.097
Along Busbar to Cryocooler	4.84E-04	6.10E-02	320		0.03	0.011
Total						**0.200**

Table 34: Temperature Difference Between Leads and Busbar (Persistent mode)

Path	Area (m^2)	Length (m)	Thermal Conductivity (W/m-K)	Thermal Conductance (mW/K)	Heat load (W)	Temperature Difference (K)
CuLead to Copper Block				295	0.15	0.499
Cu Block	2.26E-03	1.27E-02	320		0.15	0.003
CuBlock to Busbar				277	0.15	0.530
Busbar to Cryocooler	4.84E-04	6.10E-02	320		0.15	0.058
Total						**1.089**

Table 35: Temperature Difference Between Leads and Busbar (Charging mode)

Path	Area (m^2)	Length (m)	Thermal Conductivity (W/m-K)	Thermal Conductance (mW/K)	Heat load (W)	Temperature Difference (K)
Busbar to BraidedCu1				980	0.05	0.047
BraidedCu1	2.02E-04	2.60E-01	320		0.05	0.186
BraidedCu1 to MagnetTop				242	0.05	0.190
MagnetTop Total						**0.423**
Busbar to BraidedCu2				980	0.05	0.047
BraidedCu2	2.02E-04	1.30E-01	320		0.05	0.093
BraidedCu2 to MagnetBot				242	0.05	0.190
Magnet Bottom Total						**0.330**

Table 36: Temperature Difference Between Magnet and Busbar (Persistent Mode)

Path	Area (m^2)	Length (m)	Thermal Conductivity (W/m-K)	Thermal Conductance (mW/K)	Heat load (W)	Temperature Difference (K)
Busbar to BraidedCu1	3.23E-03			612	0.124	0.063
BraidedCu1	2.02E-04	2.60E-01	320		0.124	0.500
BraidedCu1 to MagnetTop	1.61E-03			270	0.124	0.285
MagnetTop Total						**0.848**
Busbar to BraidedCu2	3.23E-03			612	0.124	0.063
BraidedCu2	2.02E-04	1.30E-01	320		0.124	0.250
BraidedCu2 to MagnetBot	2.42E-03			270	0.124	0.190
Magnet Bottom Total						**0.503**

Table 37: Temperature Difference Between Magnet and Busbar (Charging Mode)